Near-Infrared Tm^{3+}:ZBLAN Fiber Lasers

Chenglai Jia

Department of Electrical and Computer Engineering

McGill University

Montreal, Quebec, Canada

December, 2016

A thesis submitted to McGill University in partial fulfilment of the requirements of the degree of Doctor of Philosophy.

ABSTRACT

All-fiber lasers in the near-IR region from 800 nm to 2500 nm have become a promising technology and been successfully applied in the fields of optical sensing, spectroscopy, communications, and medical surgery. Recognized as the most stable heavy metal fluoride glass, ZBLAN fiber is an excellent host for rare-earth ions to generate lasing emission in the near-IR region. In this thesis, we demonstrate the use of Tm^{3+}:ZBLAN fiber to achieve near-IR lasing emission at 810 nm, 1480 nm, 1900 nm and 2300 nm in all-fiber configuration. Simultaneous multi-band or multi-wavelength lasing outputs are realized with different output manners including CW, Q-switched, and mode-locked operations.

First, experimental studies of CW Tm^{3+}:ZBLAN fiber lasers are provided. A dual-band CW Tm^{3+}:ZBLAN fiber at 810 nm and 1487 nm using a single linear cavity pumped at 1064 nm, as well as a dual-band three-wavelength CW Tm^{3+}:ZBLAN fiber laser at 1460 nm, 1503 nm and 1873 nm are presented. Then, a widely tunable dual-wavelength Tm^{3+}:silica fiber laser at 1900 nm is introduced. A tuning range of 70 nm with alternate switching operation by ~5.4 nm separation is achieved. These multi-band or multi-wavelength laser sources will find important applications in the fields of LIDAR, multi-wavelength absorption spectroscopy, and fiber cavity ring-down spectroscopy.

Next, graphene is employed as a saturable absorber for pulse generation in Tm^{3+}:ZBLAN fiber laser. A passively synchronized Q-switched dual-band fiber ring laser at 1480 nm and 1840 nm with a synchronized repetition rate from 20 kHz to 40.5 kHz is shown. Then, a mode-locked dual-band fiber linear laser at 1480 nm and 1845 nm with synchronized or unsynchronized mode-locked pulses is demonstrated by controlling the cavity lengths. Such dual-band pulsed fiber laser sources will be important in the fields of spectroscopy, instrumentation, communications and nonlinear frequency conversion.

Finally, bidirectional pumping scheme at 795 nm is adopted to stimulate two lasing transitions, $^3H_4 \rightarrow {}^3H_6$ for 1900 nm and $^3F_4 \rightarrow {}^3H_5$ for 2300 nm, simultaneously. A CW Tm^{3+}:ZBLAN all-fiber laser with co-lasing emission at 1875 nm and 2320 nm, along with a passively Q-switched Tm^{3+}:ZBLAN all-fiber laser at 1895 nm and 2315 nm using a graphene SA

with a synchronized repetition rate from 10.8 kHz to 25.2 kHz are presented. Such fiber laser sources can add new capabilities in the newly exploited optical transmission window around 2000 nm or for sensing and gas concentration detection.

ABRÉGÉ

Les lasers à fibre optique qui émettent dans le proche infrarouge entre 800 nm à 3000 nm font partie des technologies les plus prometteuses et sont appliquées avec succès dans les domaine des capteurs optiques, dans la spectroscopie, les communications et dans la médicine chirurgicale. La fibre optique à base de ZBLAN est le plus stable verre fluoré à base de métaux lourds et un hôte excellent pour les ions des éléments terrestres rares pour la génération d'émissions laser dans le proche infrarouge. Dans cette thèse, on démontre l'utilisation de la fibre au Tm^{3+}:ZBLAN pour obtenir des émissions laser à 810 nm, 1480 nm, 1900 nm et 2300 nm dans le cadre d'un système basé intégralement sur la fibre optique. On utilise des différents procédées pour obtenir des émissions laser sur plusieurs bandes passantes et à multiples longueurs en mode onde continue (CW), à commutation de Q., et en opération de verrouillage de mode.

Premièrement, on présente les études expérimentaux des lasers à base de fibre optique au Tm^{3+}:ZBLAN en mode CW. On démontre l'utilisation d'une seule cavité linéaire avec un signal de pompe à 1064 nm pour obtenir un signal laser en mode CW à deux bandes passantes à 810 nm et 1487 nm. Le même système peut être étendue pour obtenir un signal laser à deux bandes passantes en mode CW à trois longueurs d'ondes: 1460 nm, 1503 nm et 1873 nm. Subséquemment, on introduit un laser à base de Tm^{3+} fibre de silice à double longueur d'onde autour de 1900 nm qui peut être largement accorde. On obtient une opération sur un registre de longueurs d'ondes de 70 nm avec la possibilité de commutation avec une séparation autour de 5.4 nm. Ces lasers sur plusieurs bandes passantes ou à plusieurs longueurs d'ondes sont utiles dans le domaine du LIDAR, de la spectroscopie d'absorption à plusieurs longueurs d'ondes, ou dans la spectroscopie par absorption laser dans un résonateur optique en anneau.

Ensuite, le graphène est employé comme absorbeurs saturable pour la génération des pulsations dans le cadre des lasers à base de Tm^{3+}:ZBLAN. On démontre un laser en anneau à commutation de Q., à deux bandes passantes aux longueurs d'onde de 1480 nm et de 1840 nm et avec une taux de répétition synchronisée de 20 kHz à 40.5 kHz. Par la suite, si on contrôle les longueurs des cavités, on peut obtenir un laser à verrouillage de mode, à deux bandes passantes à 1480 nm et 1845 nm, avec des pulsations à verrouillage de mode synchronisées ou non-synchronisées. Ces types de sources de laser pulses à deux bandes passantes seront importantes

dans les domaines de la spectroscopie, de l'instrumentation, des communications et de la conversion non linéaire des fréquences.

Enfin, l'utilisation d'un mécanisme de pompage bidirectionnel à 795 nm est adopte pour stimuler deux transitions laser simultanées: $^3H_4 \rightarrow {}^3H_6$ pour 1900 nm and $^3F_4 \rightarrow {}^3H_5$ pour 2300 nm. On présente un système laser de Tm^{3+}:ZBLAN basé intégralement sur la fibre optique à émission en mode CW, à 1875 nm et 2320 nm, simultanément. On démontre que en utilisant le graphène SA, on obtient un laser de Tm^{3+}:ZBLAN basé intégralement sur la fibre optique avec des émissions à 1895 nm et à 2315 nm, à commutation de Q. de manière passive et avec un taux de répétition entre 10.8 kHz et 25.2 kHz. Ces dernières sources laser ajoutent du potentiel aux bandes de transmission optiques autour de 2000 nm, aux capteurs optiques et à la détection des concentrations de gaz.

ACKNOWLEDGEMENTS

First of all, I would like to thank my supervisor Prof. Lawrence Chen for his five years' guidance and support. When we first met on the MEDA weekend in March, 2012, I was deeply impressed by his kindness and enthusiasm. At that time I have decided to devote my Ph.D. study in his group at McGill University. During these five years, I have benefited tremendously from his profound knowledge, thinking and integrity. He can always provide insights to solve all my experimental problems. He is also always considerate of his students.

I would like to thank other professors in the photonics system group: Prof. David Plant, Prof. Andrew Kirk, Prof. Martin Rochette, and Prof. Odile Liboiron-Ladouceur. Their contribution and management make for the world-class photonic research lab. I would like to thank Prof. Zetian Mi and Prof. Martin Rochette, who serve as my Ph.D. committee member to provide guidance. I also would like to thank Dr. Philip Roche and Dr. Zhaobing Tian, who made great efforts to keep the lab running smoothly and efficiently.

Special thanks to Dr. Bhavin Shastri from Princeton University. He provided me with the graphene saturable absorber samples, and helped a lot for our pulsed laser experiments.

I would like to thank the people in the photonics system group who helped me during my Ph.D. study: Dr. Abdul Sarmani, Dr. Jia Li, Dr. Junjia Wang, Dr. Chunshu Zhang, Mr. Kishor Ramaswamy, Dr. Ming Ma, Ms. Maria-Iulia Comanici, Ms. Zifei Wang, Dr. Meng Qiu, Dr. Lizhu Li, Mr. Peicheng Liao, Dr. Thibault North, Dr. Alaa Al-kadry and Dr. Sandrine Fillion-Côté. Special thanks to Mr. Nurmemet Abdukerim, who provides a lot of guidance for my experiments.

I would also like to thank all the students devoting for McGill Electrical Engineering Graduate Student Society and McGill Chinese Graduate Student Association.

Last but not least, I would like to express my sincere gratitude to my wife, who accompanies me during my Ph.D. study. Also I would like to thank my parents for their love and support.

TABLE OF CONTENTS

LIST OF FIGURES

LIST OF ABBREVIATIONS

ASE	Amplified spontaneous emission
CNT	Carbon nanotube
CW	Continuous wave
DBR	Distributed Bragg reflector
DC	Double cladding
DFB	Distributed feedback
ECL	External cavity laser
EDFA	Erbium-doped fiber amplifier
$\mathbf{Er^{3+}}$	Erbium
ESA	Electrical spectrum analyzer
FBG	Fiber Bragg grating
FWHM	Full width at half maximum
Hi-Bi	High birefringence

LIDAR	Light detection and ranging
Mid-IR	Mid-infrared
NA	Numerical aperture
Near IR	Near-infrared
OC	Optical coupler
ODL	Optical delay line
OSA	Optical spectrum analyzer
PC	Polarization controller
PDI	Polarization dependent isolator
PI-ISO	Polarization independent isolator
PMF	Polarization maintaining fiber
RF	Radio frequency
SA	Saturable absorber
SBS	Stimulated Brillouin scattering

SLM	Single longitudinal mode
SNR	Signal-to-noise ratio
TBWP	Time bandwidth product
TDFL	Thulium-doped fiber laser
Tm^{3+}	Thulium
UV	Ultra-violet
VCSEL	Vertical-cavity surface-emitting laser
WDM	Wavelength division multiplexing
YDFL	Ytterbium-doped fiber laser
ZBLAN	ZrF_4-BaF_2-LaF_3-AlF_3-NaF

Chapter 1

Introduction

1.1 Introduction

LASER is the acronym for **L**ight **A**mplification by **S**timulated **E**mission of **R**adiation. In 1917, Albert Einstein first introduced the theory of stimulated emission, becoming the basis of the laser. In 1957, Gordon Gould first publicly used the word “LASER”, which is the first recorded use of this acronym [1]. In 1960, Theodore Maiman from Hughes Research Laboratories invented the first working laser based on ruby [2]. The invention of fiber laser has a history almost as long as the laser itself. In 1961, Elias Snitzer from American Optical Company invented the first fiber laser, which was a Neodymium-doped fiber laser at 1060 nm pumped by a flash lamp [3]. Due to the lack of low loss fibers and high efficiency pump sources, progress on fiber lasers developed slowly for the next two decades. However, since the first demonstration of Erbium fiber laser amplifier by David Payne in 1987 [4], research on different fiber lasers has progressed rapidly and made great achievements.

Recognized as one of the top ten technological achievements in the twentieth century, laser is ubiquitous with an increasing important role. Different from other light sources, lasers emit light coherently offering a narrow linewidth and low dispersion in a modern coherent communication system. Lasers have many important applications in optical disk drives, laser printers, laser surgery, industrial cutting, fiber-optic communication, etc. More especially, near infrared (near-IR) fiber lasers, from 800 nm to 2500 nm, play a vital role as a high intensity source for applications in telecommunication, eye safe laser radar, and medicine.

In this chapter, the motivation for building near-IR fiber lasers as well as our objectives are introduced in Section 1.2. The main contributions of the thesis along with the corresponding published papers are described in Section 1.3. Following that, a brief outline of this thesis is presented in Section 1.4.

1.2 Motivation and Objectives

Lasers have played an important role with the development of fiber communication in the past few decades. Narrow linewidth lasing outputs from lasers guarantee a coherent communication system with low dispersion and nonlinearity. Especially, the all-fiber configurations make an easy integration of laser sources into the fiber networks propagating in the 1550 nm transmission window. However, only the 1550 nm window cannot satisfy the increasing needs for telecommunication and other applications.

All-fiber lasers in the near-IR region from 0.8 μm to 2.5 μm have drawn much attention from scientists all over the world. 0.81 μm corresponds to the first telecommunication windows (800-900 nm). Even though the fiber losses are relatively high in this region, 0.81 μm lasers are suitable for short-distance transmission. In addition, 1.48 μm is situated in the S-band of the third telecommunication window which cannot be amplified by Erbium-doped fiber amplifier (EDFA). 1.48 μm laser is a good source to excite the $^4I_{13/2}$ energy level of the Er^{3+} ion in order to provide gain at 1.55 μm through the $^4I_{13/2}\rightarrow{}^4I_{15/2}$ transition. The 1.48 μm wavelength also lies near an overtone absorption peak of liquid water and can provide a convenient means for water detection in various liquids. Furthermore, fiber lasers near 1.9 μm have received intense research interest in the past decade, as the eye-safe laser radiation around 1.9 μm coincides with some absorption lines of chemical compounds (H_2O, N_2O, CO_2, etc.). The thulium (Tm^{3+}) doped fiber amplifier offers a remarkably broadband emission spectrum of transition covering about 30 THz (~1700 to ~2100 nm) [5]. It is also an ideal pump for mid-IR lasers. At last, the 2.3 μm atmospheric window gives access to many gaseous species of interest such as CH_4, NH_3, CO, HF, without H_2O or CO_2 interference, while these molecules have strong absorption lines near 2.3 μm which are suitable for isotope ratio measurement applications [6]. Therefore, the near-IR laser sources are of great importance and need to be investigated further.

Additionally, recognized as the most stable heavy metal fluoride glass, ZBLAN fiber has distinctive advantages over silica fiber due to its lower phonon energies. The higher phonon energy in silica glass limits the effectiveness of self-quenching and shortens the $^3F_4$ laser lifetime, while the lower phonon energies in ZBLAN glass reduce competition of multiphonon processes and fluorescent decay processes, which make it possible for more lasing transitions in the near-IR region [7]. Moreover, higher transmittance around 2 μm in ZBLAN host makes it a better choice for near-IR lasers. In short, due to these huge potentials and advantages of near-IR lasers and ZBLAN glasses, ZBLAN fiber lasers operating in the near-IR region will become a promising technology, and are worth to investigate in detail.

In the recent years, Tm^{3+} fiber lasers have attracted much attention from scientists all over the world and made rapid development since the past few decades. In the silica host, Tm^{3+} ions are mainly used to generate light emission around 1900 nm through the transition $^3F_4 \rightarrow ^3H_6$. An output of over 200 W from 1927 nm to 2097 nm with a slope efficiency of 65% has been achieved by pumping at 790 nm [8]. A switchable dual-wavelength Tm^{3+} fiber laser at 1.94 μm has been realized by high-birefringence fiber Bragg gratings (FBGs) [9]. A tunable multi-wavelength Tm-doped fiber laser has been achieved by pumping at 1550 nm into Tm-doped polarization maintaining fiber (PMF) [10]. In addition, passive mode-locked Tm^{3+} laser near 2 μm has been realized by employing a carbon nanotube (CNT) as a saturable absorber (SA) [11].

In the ZBLAN host, a much longer lifetime (1350 μs) at the $^3H_4$ state [7] makes it possible to induce three lasing transitions including $^3H_4 \rightarrow ^3H_6$ (λ=0.81 μm), $^3H_4 \rightarrow ^3F_4$ (λ=1.48 μm) and $^3H_4 \rightarrow ^3H_5$ (λ=2.3 μm). In [12-14], a Tm^{3+}:ZBLAN gain medium was pumped at around 1110 nm to achieve lasing at 785/810 nm respectively. In our group, dual-wavelength emission using a single transition has also been demonstrated; around 800 nm using the $^3H_4 \rightarrow ^3H_6$ transition [15] and around 1480 nm using the $^3H_4 \rightarrow ^3F_4$ transition[16]. In both cases, up-conversion pumping at 1064 nm in a Tm^{3+}:ZBLAN fiber was used. Additionally, dual-band operation at 810/1480 nm in a single piece of Tm^{3+}:ZBLAN fiber has been achieved, with both lasing transitions sharing the same upper energy level ($^3H_4 \rightarrow ^3H_6$, $^3H_4 \rightarrow ^3F_4$) [17].

This thesis will focus specifically on one lanthanide ion, Tm^{3+}, and its lasing applications as a doping agent in a ZBLAN fiber. In the near infrared region, Tm^{3+} ions can provide gain at 810 nm, 1480 nm, 1900 nm and 2300 nm. 810 nm is situated in the first communication window for short distance tele-communication; 1480 nm is situated to the S-band of the third communication window, where the amplification provided by the EDFA is relatively low; eye safe radiation at 1900 nm and 2300 nm coincides with some absorption lines of several chemical compounds. Therefore, we will use the Tm^{3+}:ZBLAN fiber to realize multi-band near-IR fiber lasers at 810 nm, 1480 nm, 1900 nm and 2300 nm with different output manners (CW, Q-switched and mode-locked). Furthermore, this thesis will also focus on the use of Tm^{3+}:silica fiber for widely tunable and switchable operation at 1900 nm, as ASE (amplified spontaneous emission) at 1900 nm of Tm^{3+}:silica fiber is broader than that of Tm^{3+}:ZBLAN fiber.

Firstly, continuous wave (CW) multi-band and multi-wavelength fiber lasers have attracted much attention for their applications in wavelength division multiplexing (WDM) transmission system, fiber component testing, and fiber optical sensing. They can be realized by pumping at different wavelengths, and combining various kinds of optical filters, such as FBGs, compound fiber rings, Sagnac loop filters and Fabry-Pérot cavities. In certain practical applications, it is also desirable to introduce and enhance the flexibility and functionality of multi-wavelength fiber lasers. Hence, the tunable and switchable operation, the lasing locations and the number of channels are worth to investigate. In this thesis, we demonstrate the use of Tm^{3+}:ZBLAN fiber to achieve a dual-band CW fiber laser at 810 nm and 1487 nm using a single linear configuration pumped at 1064 nm, along with a dual-band CW fiber laser at 1460/1503 nm and 1873 nm using two different linear cavities pumped at 1064 nm and 1560 nm, respectively. Moreover, we demonstrate the use of Tm^{3+}:silica fiber to achieve a widely tunable and switchable dual-wavelength fiber laser with a tuning range of 70 nm and alternate wavelength switching operation by 5.4 nm separation.

Secondly, high power optical pulses play an increasingly important role in industrial material processing, medical treatment, high capacity telecommunication and terahertz generation. Q-switching and mode-locking are the two main methods enabling pulse generation [18]. Q-switching is a modulation process of the quality factor Q to generate a high intensity pulse with typical durations ranging from μs to ns; on the other hand, mode-locking is a technique to balance the intra-cavity dispersion and nonlinearity, and to induce a fixed-phase in order to obtain ultrashort pulses with typical duration ranging from ps down to fs. Recently, graphene has emerged as an innovative and promising material as an SA for passively Q-switched and mode-locked fiber lasers to facilitate pulse generation [19, 20]. Its unique electrical and optical properties, such as ultra broadband operation, fast response time and ease of fabrication, make it as a suitable SA to be integrated in fiber lasers for passive pulse generation. In this thesis, we demonstrate the use of Tm^{3+}:ZBLAN fiber along with the graphene SA to obtain (1) a passively synchronized Q-switched dual-band fiber ring laser at 1480 nm and 1840 nm with a synchronized repetition rate from 20 kHz to 40.5 kHz, and (2) a simultaneous mode-locked dual-band fiber linear laser at 1480 nm and 1845 nm with synchronized or unsynchronized mode-locked pulses.

Thirdly, there are increasing needs for fiber lasers emitting in the 1.9-2.5 μm spectral range for varieties of applications in the fields of LIDAR, remote sensing, gas absorption spectroscopy, material processing, as well as medical therapy and diagnostics. Compared with the silica host, the ZBLAN host has a reduced multiphonon emission rate and a longer radiative lifetime of the upper laser level, especially for the $^3F_4 \rightarrow ^3H_5$ transition with resulting emission around 2300 nm [21]. In addition, the $^3H_4 \rightarrow ^3H_6$ transition with resulting emission around 1900 nm can be further improved by the simultaneous laser oscillation around 2300 nm to increase the branching ratio from $^3F_4$ to $^3H_4$ [22, 23]. In this thesis, we demonstrate a CW Tm^{3+}:ZBLAN all-fiber laser at 1875 nm and 2320 nm, along with a passively Q-switched Tm^{3+}:ZBLAN all-fiber laser at 1895 nm and 2315 nm using a graphene SA with a synchronized repetition rate from 10.8 kHz to 25.2 kHz.

1.3 Contributions

1.3.1 Significance of the work

The objective of this thesis is to use the Tm^{3+}:ZBLAN fiber to realize multi-band near-IR fiber lasers at 810 nm, 1480 nm, 1900 nm and 2300 nm with different output manners (CW, Q-switched and mode-locked), and to use the Tm^{3+}:silica fiber to achieve CW widely tunable and switchable operation at 1900 nm. Our work can be categorized into the following parts, as shown in Fig. 1.1. The contributions of our work are highlighted and summarized as follows.

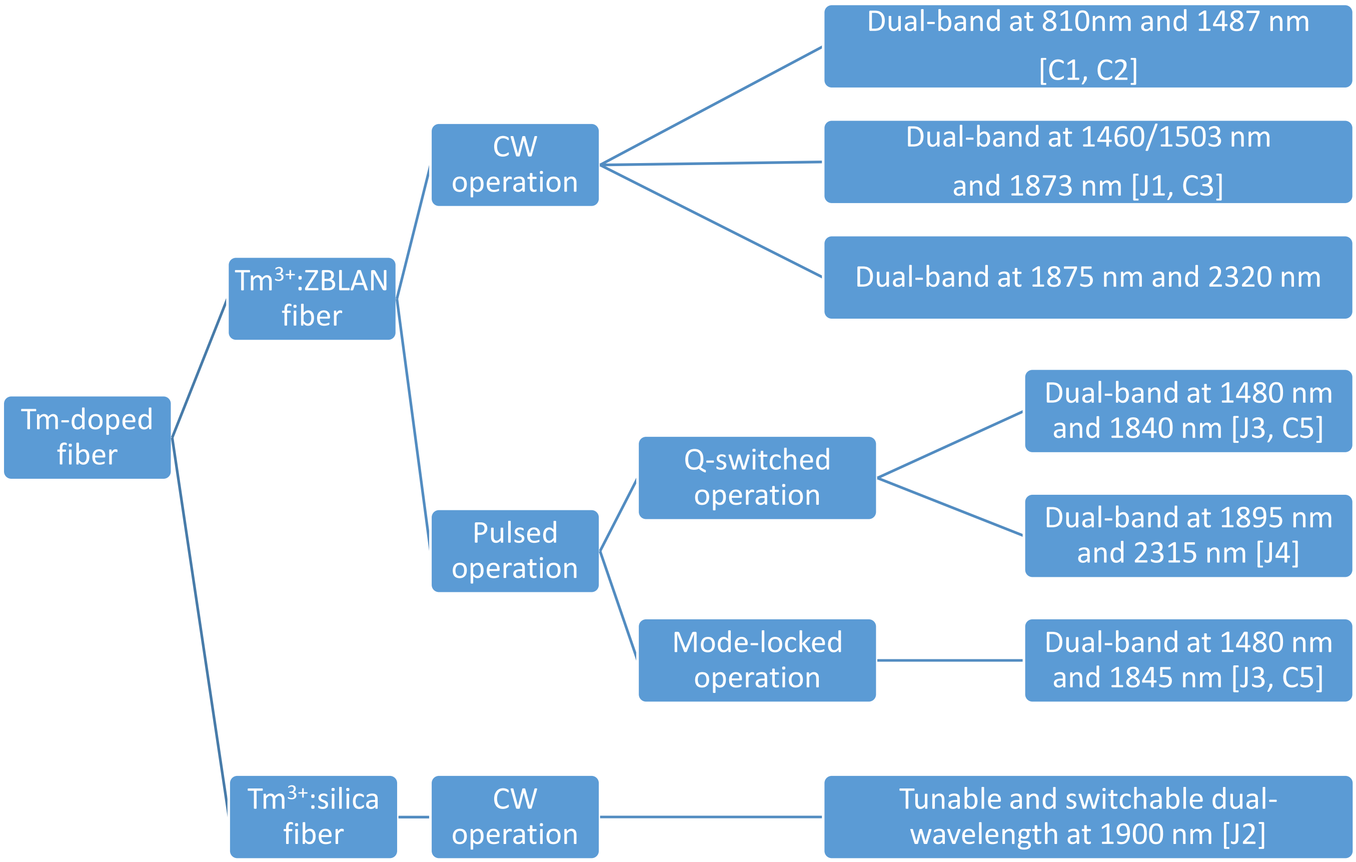

Fig. 1.1 Contributed research on Tm-doped fiber lasers.

CW Dual-band at 810 nm and 1487 nm: a CW dual-band Tm^{3+}:ZBLAN fiber laser at 810 nm and 1487 nm using a single linear cavity configuration and two FBGs at each wavelength is demonstrated. Dual-band lasing operation is achieved using a single pump at 1064 nm. By controlling the pump power at 1064 nm, switchable operation at the two wavelengths is realized. Both lasing wavelengths can emit output powers more than 25 mW. These dual-band lasers working in different bands are useful for chemical detection and sensing by simultaneously measuring the fluorescence spectrum, the reflectance, and the optical attenuation at several wavelengths.

CW Dual-band at 1460/1503 nm and 1873 nm: a three-wavelength Tm^{3+}:ZBLAN fiber laser emitting simultaneously at 1460 nm, 1503 nm and 1873 nm is demonstrated for the first time. One cavity is pumped by 1064 nm with switchable lasing operation at 1460 nm and 1503 nm, while the other cavity is pumped by 1560 nm with lasing operation at 1873 nm. All these three lasing wavelengths can emit output powers above 10 mW. Such a three-wavelength laser has been successfully applied in the sensing application in single-pass absorption measurements for detecting and quantifying water concentration in acetone [24].

CW Dual-band at 1875 nm and 2320 nm: a CW Tm^{3+}:ZBLAN all-fiber laser at 1875 nm and 2320 nm is demonstrated for the first time in an all-fiber configuration. CW co-lasing operation at the two wavelengths is obtained under a bidirectional pumping scheme at 795 nm. The maximum output powers at 1875 nm and 2320 nm can reach ~4.6 mW and ~1.5 mW, respectively. Such sources can add new capabilities in the newly exploited optical transmission window around 2000 nm or for sensing and gas concentration detection.

Q-switched dual-band at 1480 nm and 1840 nm: a passively synchronized dual-band Q-switched Tm^{3+}:ZBLAN fiber laser at 1480 nm and 1840 nm based on a graphene SA is demonstrated for the first time. Q-switched pulses at these two wavelengths with synchronized repetition rate from 20 kHz to 40.5 kHz are achieved using single gain medium. Such ultra-broadband synchronized Q-switched pulses can provide low-cost and convenient high power nanosecond pulses for applications in the fields of nonlinear frequency conversion, spectroscopy and chemical sensing.

Q-switched dual-band at 1895 nm and 2315 nm: a passively Q-switched dual-band Tm^{3+}:ZBLAN all-fiber laser at 1895 nm and 2315 nm using a graphene SA is demonstrated for the first time. Using bidirectional pumping at 795 nm, simultaneous Q-switching operation is obtained with a synchronized repetition rate from 10.8 kHz to 25.2 kHz, and pulse durations as short as 4.5 μs at 1895 nm and 4.9 μs at 2315 nm. Such a dual band Q-switched laser around 1900 nm and 2300 nm can provide a high-power nanosecond pulse source for applications on the newly exploited optical transmission window around 2000 nm, along with the near-IR dual-band pulse source for the chemical sensing measurements.

Mode-locked dual-band at 1480 nm and 1845 nm: a simultaneous mode-locked dual-band Tm^{3+}:ZBLAN fiber laser at 1480 nm and 1845 nm based on a graphene SA is demonstrated for the first time. By adjusting the cavity lengths at the two wavelengths, synchronized and unsynchronized mode-locked fiber lasers with controllable fundamental frequencies are realized.

These dual-band mode-locked fiber lasers can find important applications in developing optical transmitters in the S-band and around 1900 nm.

CW tunable and switchable dual-wavelength at 1900 nm: a widely tunable and switchable dual-wavelength CW Tm^{3+}:silica fiber laser based on the Sagnac loop mirror is demonstrated with a tuning range from 1857 nm to 1927 nm. Such a tuning range over 70 nm is the largest tuning range obtained from a dual-wavelength Tm^{3+}:silica fiber laser. Alternate/sequential switching operation is realized with ~5.4 nm wavelength spacing. The output of each lasing operation has an SNR larger than 50 dB, while its full width at half maximum (FWHM) is smaller than 0.06 nm. The center wavelength variation is less than 0.02 nm, while its output power fluctuations are less than 0.7 dB during 15 minutes. Such a widely tunable and switchable dual-wavelength laser operating at 1900 nm will be important in the fields of LIDAR, multi-wavelength absorption spectroscopy, and fiber cavity ring-down spectroscopy.

1.3.2 List of published journal and conference papers

The following is a list of journal and conference papers that have been published or submitted for publication.

J1. N. L. P. Andrews, A. G. MacLean, J. E. Saunders, J. A. Barnes, H.-P. Loock, **C. Jia**, K. Ramaswamy, L. R. Chen, M. Saad, "Quantification of different water species in acetone using a NIR-triple-wavelength fiber laser," *Optics Express,* vol. 22, pp. 19337-19347, 2014.

J2. **C. Jia**, X. Liang, M. Rochette, and L. R. Chen, "Alternate wavelength switching in a widely tunable dual-wavelength Tm^{3+}-doped fiber laser at 1900 nm," *IEEE Photonics Journal,* vol. 7, pp. 1-7, 2015.

J3. **C. Jia**, B. J. Shastri, N. Abdukerim, M. Rochette, P. R. Prucnal, M. Saad, L. R. Chen, "Passively synchronized Q-switched and mode-locked dual-band Tm^{3+}:ZBLAN fiber lasers using a common graphene saturable absorber," *Scientific Reports,* vol. 6, p. 36071, 2016.

J4. **C. Jia**, B. J. Shastri, P. R. Prucnal, M. Saad, L. R. Chen, " Simultaneous Q-switching of a Tm^{3+}:ZBLAN fiber laser at 1.9 μm and 2.3 μm using graphene", *IEEE Photonics Technology Letters*, vol. 29, pp. 405-408, 2017.

C1. K. Ramaswamy, **C. Jia**, M. Dastmalchi, L. R. Chen, and M. Saad, "Dual-band 810/1480 nm Tm^{3+}: ZBLAN fiber laser," in *IEEE Photonics Conference*, pp. 273-274, 2013, Bellevue, WA.

C2. K. Ramaswamy, **C. Jia**, M. Dastmalchi, B. Frison, A. R. Sarmani, L. R. Chen, and M. Saad., "Dual-Wavelength Tm^{3+}:ZBLAN Fiber Lasers," in *Workshop on Specialty Optical Fibers and their Applications*, p. F2.4, 2013, Sigtuna, Sweden.

C3. **C. Jia**, K. Ramaswamy, L. Chen, A. G. Maclean, N. L. P. Andrews, J. Saunders, J. A. Barnes, H.-P. Loock, and M. Saad, "Three-wavelength Tm^{3+}:ZBLAN fiber laser and its applications in water detection," in *IEEE Photonics Conference,* pp. 479-480, 2014, San Diego, CA.

C4. **C. Jia**, B. J. Shastri, M. Rochette, L. R. Chen, and M. Saad, "Graphene-based passively Q-switched Tm^{3+}:ZBLAN fiber laser at 1480 nm," in *IEEE Photonics Conference*, pp. 326-327, 2015, Reston, VA.

C5. **C. Jia**, B. J. Shastri, N. Abdukerim, M. Rochette, P. R. Prucnal, L. R. Chen, and M. Saad, "Passively synchronized Q-switched and simultaneous mode-locked dual-band Tm^{3+}: ZBLAN fiber laser at 1.48-and 1.85-μm using common graphene saturable absorber," in *Specialty Optical Fibers*, p. SoTu1G. 4, 2016, Vancouver, BC.

1.4 Outline of the thesis

In this chapter, some background knowledge of the near-IR fiber lasers are introduced. The motivations, objectives along with the significance of the research described in this thesis are also discussed. The remainder of this thesis is organized as follows.

In Chapter 2, background on the properties of glass and rare earth ion doping is introduced first. Then brief introduction on fiber lasers including the population inversion and various laser cavities is discussed. Properties of graphene as SA are presented at last.

Chapter 3 discusses the CW Tm-doped fiber lasers at 1480 nm and 1900 nm. First, a dual-band Tm^{3+}:ZBLAN fiber laser at 810 nm and 1487 nm, along with a dual-band three-wavelength Tm^{3+}:ZBLAN fiber laser at 1460/1503 nm and 1873 nm are discussed. Then, a widely tunable and switchable dual-wavelength Tm^{3+}:silica fiber laser at 1900 nm with a tuning range of 70 nm is presented. Chapter 3, in part, is a reprint of the material as it appears in proceedings of the *2013 IEEE Photonics Conference* authored by K. Ramaswamy, **C. Jia**, M. Dastmalchi, L. R. Chen, and M. Saad, "Dual-band 810/1480 nm Tm^{3+}: ZBLAN fiber laser," in *Optics Express* authored by N. L. P. Andrews, A. G. MacLean, J. E. Saunders, J. A. Barnes, H.-P. Loock, **C. Jia**, K. Ramaswamy, L. R. Chen, and M. Saad, "Quantification of different water species in acetone using a NIR-triple-wavelength fiber laser," and in *IEEE Photonics Journals* authored by **C. Jia**, X. Liang, M. Rochette, and L. R. Chen, "Alternate wavelength switching in a widely tunable dual-wavelength Tm^{3+}-doped fiber laser at 1900 nm". I designed, implemented and characterized the laser.

Chapter 4 discusses the pulsed dual-band Tm^{3+}:ZBLAN fiber laser. A passively synchronized Q-switched dual-band fiber ring laser at 1480 nm and 1840 nm is discussed first, and a simultaneous mode-locked dual-band fiber linear laser at 1480 nm and 1845 nm with synchronized or unsynchronized mode-locked pulses is presented later. Chapter 4, in part, is a reprint of the material as it appears in *Scientific Reports* authored by **C. Jia**, B. J. Shastri, N. Abdukerim, M. Rochette, P. R. Prucnal, M. Saad, and L. R. Chen, "Passively synchronized Q-switched and mode-locked dual-band Tm^{3+}:ZBLAN fiber lasers using a common graphene saturable absorber". I designed, implemented and characterized the laser.

Chapter 5 discusses the dual-band Tm^{3+}:ZBLAN all-fiber laser at 1900 nm and 2300 nm. A CW Tm^{3+}:ZBLAN all-fiber laser at 1875 nm and 2320 nm is discussed first, and then a passively Q-switched Tm^{3+}:ZBLAN all-fiber laser at 1895 nm and 2315 nm using a graphene SA with a synchronized repetition rate from 10.8 kHz to 25.2 kHz is presented. Chapter 5, in part, is a reprint of the material as it appears in *IEEE Photonics Technology Letters* authored by **C. Jia**, B. J. Shastri, P. R. Prucnal, M. Saad, and L. R. Chen, " Simultaneous Q-switching of a Tm^{3+}:ZBLAN fiber laser at 1.9 µm and 2.3 µm using graphene". I designed, implemented and characterized the laser.

Chapter 6 summarizes the work and the contributions that have been done in this thesis. Also several future works are discussed briefly at the end of this chapter.

Chapter 2

Background

The invention of optical fiber by Charles Kuen Kao in 1960s has led to a revolution of telecommunication in the past few decades. Until now, silica fiber with lower loss and lower dispersion has widely served as the information transmission medium for high-speed telecommunication network all over the world. Special kinds of optical fibers, such as ZBLAN fiber, phosphate glass fiber, and tellurite glass fiber, also have important applications in different fields. Furthermore, doping of rare earth ions in optical fibers makes it possible for high-power fiber amplifiers and lasers. Before the presentation of our work, it is necessary to introduce the basic background knowledge in this chapter. Here, we first introduce the concepts of glass definition and rare earth doping. Then, some important parameters and configurations of fiber laser are discussed. Finally, the properties of graphene as SA are presented.

2.1 Glasses

2.1.1 Glasses definition

Glass is an amorphous (non-crystalline) material with a high degree of homogeneity. It shows a glass transition when heated towards the liquid state. Unlike crystals, glasses are ordered on a local scale among particles yet they lack long range order due to the variations in length and angle of the bands. Glasses demonstrate a high degree of optical uniformity over a long distance. By doping the glass matrix appropriately, its nonlinear, mechanical, thermal and spectral parameters can be modified [25].

Glasses do not have a melting point as crystals do. When the temperature is changed, glasses transit from a hard and brittle state into a molten or rubber-like state. The temperature point relating the transition from a liquid to a brittle state is called the glass transition temperature [25]. Glasses transition is not a thermodynamic equilibrium state; it suffers spontaneous crystallization [26]. The minimum critical cooling rate and the Hruby factor are two important values to describe the glass stability.

2.1.2 Silica Glass

Silica glass is the most commonly used material for fiber fabrication. Silica-based fibers are composed of silicon dioxide (SiO_2) and some certain particles acting as network formers or modifiers for different applications. Silica-based fiber has many advantages compared with other kinds of glass fiber. It is easy to manufacture a high-quality silica-based fiber over long length. The wide range of its optical transparency allows the lowest loss for fiber communication window. Its robust mechanical qualities, high degree of chemical resistance, relatively low optical nonlinearity and the availability of the material all make silica as an ideal material for fiber manufacturing. However, the most obvious disadvantage of the silica glass is its high phonon energy which is around ~1,100 cm^{-1}. Its low rare earth ions saturation concentration and high transmission loss in the near-IR also limit its development [27].

2.1.3 ZBLAN

ZBLAN is an abbreviation of fluorozirconate glass composition ($ZrFM_4$-BaF_2-LaF_3-AlF_3-NaF) which was discovered in 1975 by Poulain and Lucas at the University of Rennes in France [28]. It is known as the most stable fluoride glass and is commonly used to make most fluoride glass and fiber. ZBLAN has a very broad transmission window from the UV (ultra-violet, as short as 250 nm) to the mid-IR (mid-infrared, as long as 7 μm), low refractive index (around 1.5), low dispersion, a relatively low glass transition temperature (260℃) and a negative and low temperature dependence of refractive index (dn/dt). Fig. 2.1 shows the typical ZBLAN refractive index and attenuation loss under different wavelengths. Recent developments of ZBLAN fiber manufacturing have demonstrated significant improvement in mechanical properties and attenuation loss. ZBLAN fiber has been widely used in many different applications such as fiber lasers, spectroscopy and sensing [7, 29-32].

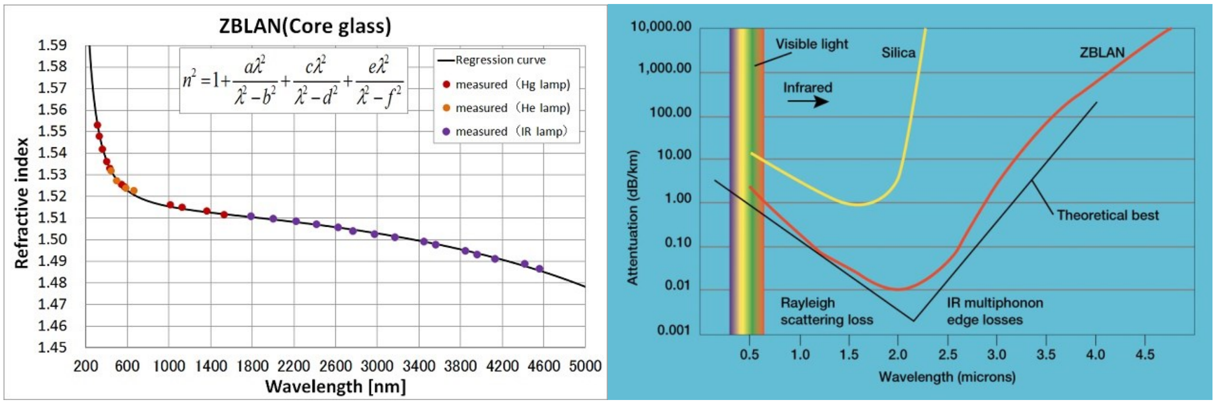

(a) (b)

Fig. 2.1 (a) Refractive index [33] and (b) attenuation loss [34] of typical ZBLAN fiber as a function of wavelength.

2.2 Rare earth

As defined by the International Union of Pure and Applied Chemists (IUPAC), the term rare earth element or rare earth metal is one of a set of seventeen chemical elements in the periodic table, specifically elements 57 (La) to 71 (Lu) plus Sc and Y [35]. The term lanthanide elements are used to describe the group of elements from 57 (La) to 71 (Lu). Due to their similar valence layer configuration as lanthanum, they are termed as lanthanide and have similar chemical characteristics.

The key to the optical behavior of lanthanide elements is that they possess a particular incomplete sub-shell - *4f* [36]. The *4f* sub-shell is situated closer to the core than the valence layer, and its electrons are not involved in bonding with any nearby atoms. Therefore, they can partially avoid the influence from local environment. Electrons could move freely between different energy levels of the *4f* sub-shell with well-circumscribed energy transition. When dissolved in a glass, Lanthanide ions' transition spectra are similar to their free ion spectra. On the contrary, transition metals with an incomplete *d* sub-shell do not possess the same shielding phenomenon as lanthanide ions. The spectral lines of transition metals ions in glass hosts are broader than those of lanthanide ions.

On the basis of Laporte's selection rule, electric transitions in centrosymmetric atoms can only occur between two states with different parity, indicating that *f-f* transitions are forbidden. However, in a lanthanide ion, the breaking of symmetry induced by perturbations such as spin orbit coupling makes electronic transitions possible.

Transition cross sections

A cross section is the effective area that govern the probability of an ion to absorb and emit light, which has a close relationship with Einstein A and B coefficients. Given the energies of two states are E_1 and E_2 (E_1 less than E_2), the absorption cross section σ_{12} is proportional to the transition probability for the absorption of a phonon (E_2-E_1), while the emission cross section σ_{12} is proportional to the transition probability for the emission of a phonon.

Lifetimes

Lifetime is in inverse proportion to the probability of an ion exiting from the excited level per unit time. It is a time constant for a given level of excited ions to decay exponentially. Usually, two main paths for decay, radiative and non-radiative, are considered for the lifetime of a given rare earth level.

$$\frac{1}{\tau} = \frac{1}{\tau_r} + \frac{1}{\tau_{nr}} \tag{2.1}$$

where τ, τ_r and τ_{nr} are the total lifetime, the radiative lifetime and the non-radiative lifetime respectively. The radiative lifetime depends on the fluorescence from the excited level to other levels below it, while the non-radiative lifetime arises from the nature of the glass host and the coupling between the states of rare earth ions.

Linewidths and Broadening

The linewidth of a transition contains both homogeneous and inhomogeneous contribution. The homogeneous broadening, including both the radiative and non-radiative processes, is a natural emission spectrum broadening resulting from the lifetime and dephasing time of the state. If an optical emitter shows homogeneous broadening, its spectral linewidth is a Lorentzian profile with its natural linewidth. The inhomogeneous broadening is actually a superposition of a set of homogeneous broadening. With variations in the local environment of an ion, the local electric field is different for each emitter, and the Stark effect changes the energy levels leading to inhomogeneous broadening. Compared with crystals, both of the homogeneous and inhomogeneous spectrum broadenings are much larger in glasses.

Spectroscopy of the Tm^{3+} ion

Tm^{3+}-doped fiber lasers and amplifiers are some of the most interesting fiber laser-based systems. They can provide lasing operation in a wide spectral range and fall into the eye-safe wavelength range which is of great importance with potential applications in free-space communications, coherent radars and hydrocarbon gases detection. Fig. 2.1 shows the typical energy levels of Tm^{3+} ions covering from UV to IR region.

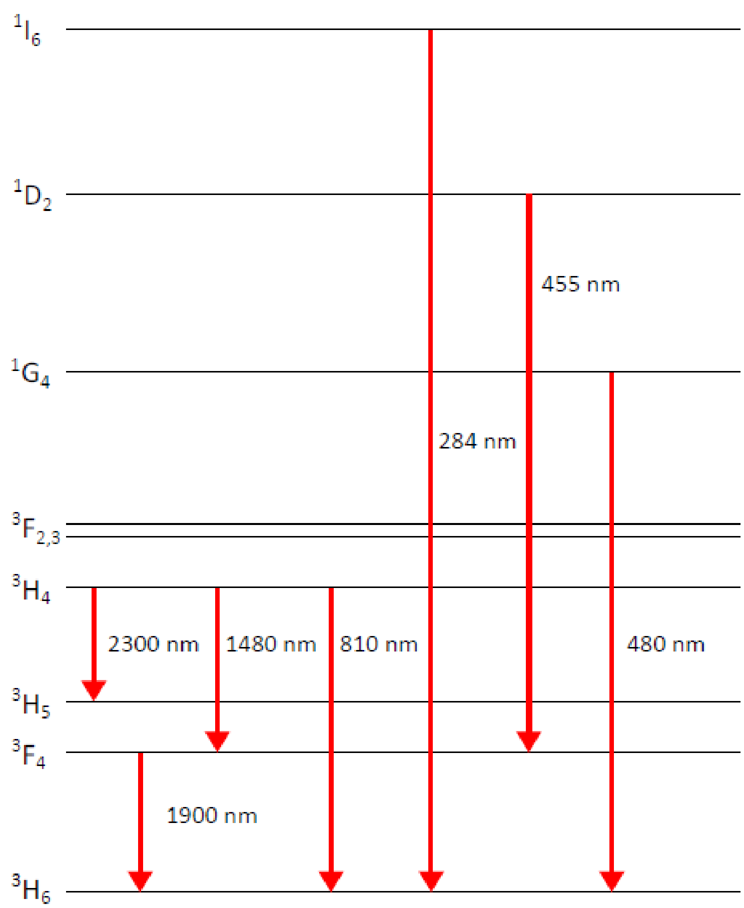

Fig. 2.2 Energy levels of the Tm^{3+} ion[37].

In the silica glass host, research for Tm^{3+} ions mainly focuses on lasing operation at 1900 nm through the transition $^3F_4 \rightarrow ^3H_6$. Direct pumping at 1575 nm and indirect pumping at 795 nm to excite $^3H_4$ have been achieved to generate lasing near 1900 nm [38].

Due to lower phonon energy in the ZBLAN host, the $^3H_4$ level's lifetime (1350 μs) is much longer than that in the silica host (14.2 μs) [7]. This makes the ZBLAN host possible to induce lasing from one upper level $^3H_4$ through three different transitions: $^3H_4 \rightarrow ^3H_5$ (λ=2.3 μm), $^3H_4 \rightarrow ^3F_4$ (λ=1.48 μm) and $^3H_4 \rightarrow ^3H_6$ (λ=0.81 μm).

When pumped at 795 nm through the $^3H_6 \rightarrow ^3H_4$ transition, lasing at 2.3 μm from $^3H_4 \rightarrow ^3H_5$ suffers a bottleneck problem from the 5 times lifetime of electrons in the $^3F_4$ level comparing with the $^3H_4$ level, slowing down electrons' return to the ground level [39]. Also lasing at 1.48 μm from $^3H_4 \rightarrow ^3F_4$ has the same problem as lasing at 2.3 μm. Therefore, co-lasing at 1.9 μm [40] or pumping at 1064 nm [41] was used to depopulate the $^3F_4$ level and to increase the efficiency of lasing at 2.3 μm or 1.48 μm. For lasing at 0.81 μm, there is no need to depopulate the $^3F_4$ level. Electrons can directly reach the ground level without the influence of the $^3F_4$ level.

2.3 Fiber lasers

2.3.1 Population inversion: three- and four-energy level systems

Population inversion plays an important role in laser physics, as it makes electromagnetic waves amplified and oscillated. For a better understanding of population inversion, the basic statistics of the particles' distribution in thermal equilibrium should be reviewed first. Boltzmann distribution is followed by the number of particles at two neighboring non-degenerated energy levels at thermal equilibrium:

$$N_2 = N_1 \exp\left(-\frac{E_2 - E_1}{k_B T}\right) = N_1 \exp\left(-\frac{h \cdot v_0}{k_B T}\right) \tag{2.2}$$

where $E_2 > E_1$ $(E_2 - E_1 = h \cdot v_0)$ and v_0 is the resonant frequency between two neighboring energy levels. The total number of particles is:

$$N = N_1 + N_2 \tag{2.3}$$

In thermal equilibrium state, the higher energy level is always less populated than the lower one. Therefore, the atomic system is naturally relaxed and does not emit light. In order to realize amplification of electromagnetic waves through stimulated emission, a non-equilibrium condition needs to be achieved. Two basic pumping schemes of laser operation, four-energy level laser system and three-energy level laser system, have been proposed to achieve such a non-equilibrium situation.

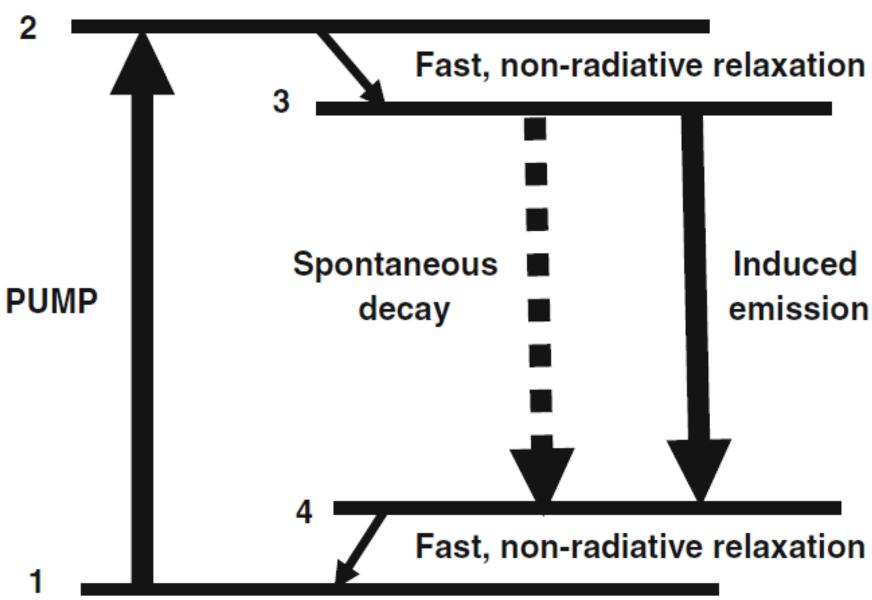

Fig. 2.3 Four-energy-level diagram of laser operation [25].

Fig. 2.2 shows the four-energy-level diagram of laser operation, offering the highest efficiency as well as the lowest laser threshold for most laser applications. The full excitation circle of the four-energy-level scheme is as followed: atoms are pumped and excited from the ground level 1 to the excited level 2 and then drop to level 3 through fast non-radiative relaxation; atoms decay spontaneously to level 4, and return to the original ground level 1 again through non-radiative relaxation. The laser operation occurs during the spontaneous decay from level 3 to level 4. Therefore, the precondition for population inversion is that spontaneous decay has to be slower than the non-radiative relaxation from level 4 to level 1.

Fig. 2.3 presents the three-energy-level scheme of laser operation. The main difference between these two schemes is that the lowest level (level 1 shown in Fig. 2.2) and the lower laser level (level 4 shown in Fig. 2.2) become a single level (level 1 shown in Fig. 2.3). Within the three-energy-level system, after spontaneous decay, particles do not return to the unpopulated terminal level but return to the original and populated ground state instead, which means the laser-terminating level is always populated. 50% or more particles have to be excited to the upper level in order to create the population inversion. Therefore, three-energy-level laser operation scheme provides an increased laser threshold and a lower efficiency. However, the three-energy-level scheme is still very important and has many different applications in fiber amplifiers and lasers.

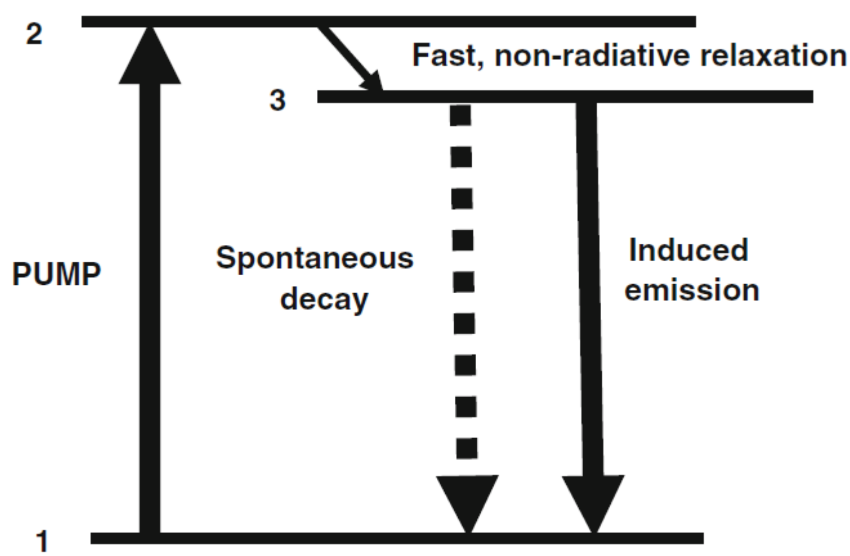

Fig. 2.4 Three-energy-level diagram of laser operation [25].

2.3.2 Fiber laser cavities

The principle of fiber laser cavities is similar to that of the traditional laser cavities. The main differences result from geometry of the active medium and the intra-cavity components. The active medium of fiber lasers is a longer optical waveguide but with very small diameter, indicating the generation of optical nonlinearities and the difficulty to achieve short Q-switch pulse durations. Currently, the ring laser cavity and the linear laser cavity are two fundamental types of laser cavities which both play an important role in fiber lasers.

Fig. 2.4 shows the typical scheme of the fiber ring laser cavity. WDM is used to couple the pump light into the ring cavity. Active fiber is employed to provide enough gain in order to achieve the threshold condition. Isolator guarantees the unidirectional propagation, and the use of filter can improve the stability of output wavelength. Despite of the complex structure, the ring laser cavity can avoid the spatial hole burning effects and be easy to achieve a tunable multi-wavelength laser with narrow linewidth output.

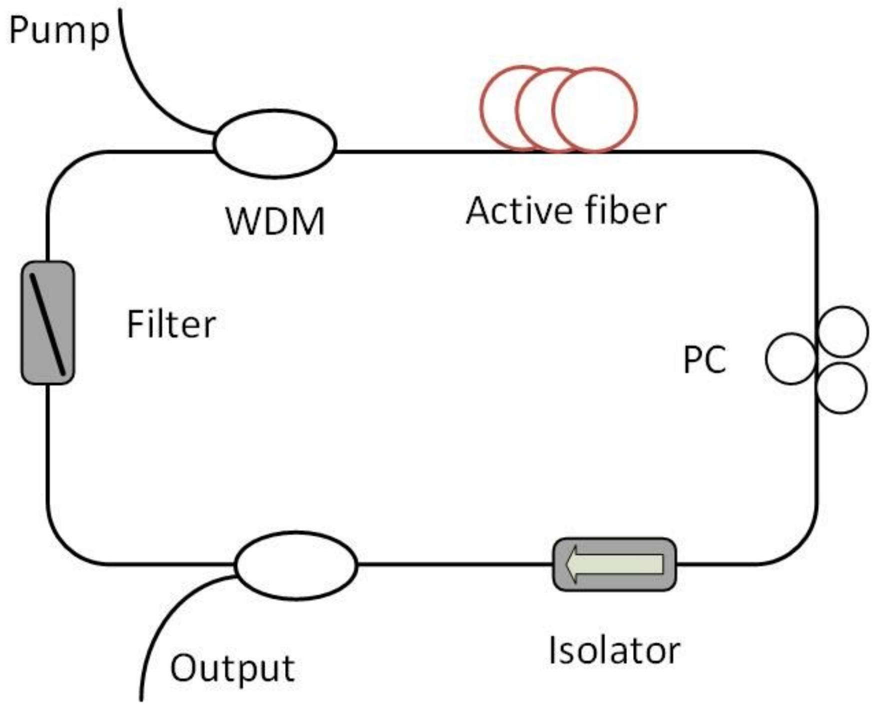

Fig. 2.5 Typical fiber ring laser cavity scheme.

Fig. 2.5 shows the typical fiber linear laser cavities including the distributed feedback (DFB) scheme and the distributed Bragg reflector (DBR) scheme. As shown in Fig. 2.5(a), DFB laser uses a phase-shifted FBG to achieve optical feedback and wavelength selection, thus producing an output with more stable frequency. It can also avoid the fusion splicing loss between the active fiber and the FBG. As shown in Fig. 2.5(b), DBR laser consists of two wavelength-matched FBGs as reflectors of Fabry- Pérot cavity. The FBGs act as dielectric mirrors allowing light to bounce back and forth inside the cavity, thus an amplified signal is created as light propagates through the gain medium each round trip.

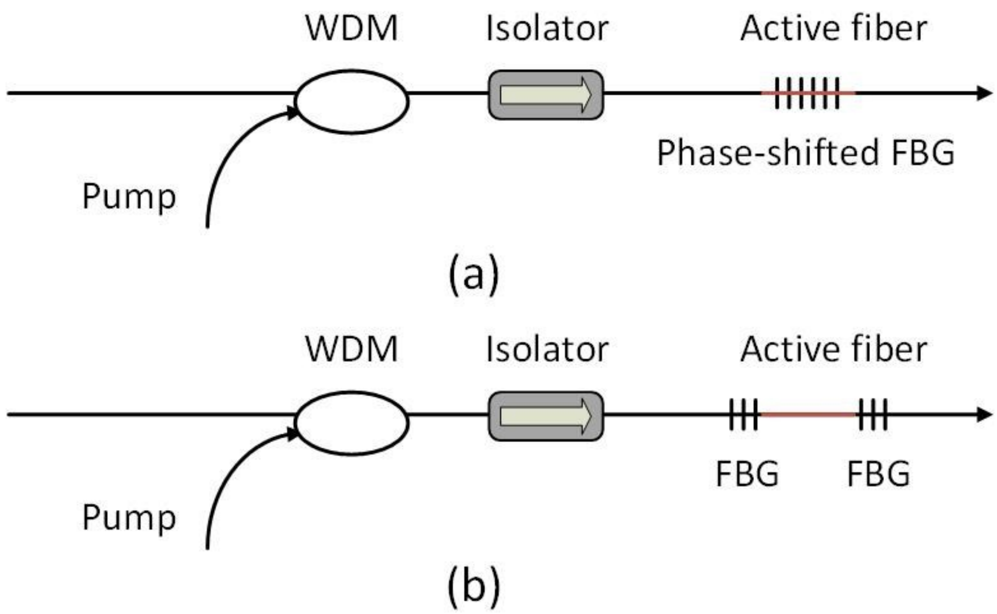

Fig. 2.6 Typical fiber linear laser cavity scheme: (a) DFB scheme; (b) DBR scheme.

2.4 Graphene

Graphene is an allotrope of carbon, a hexagonally monolayer in the form of a two-dimensional, atomic-scale lattice in which one carbon atom forms each vertex. At low energy, it has a linear energy-momentum relation near the six corners of the two-dimensional hexagonal Brillouin zone. Despite of only a single atom thick (~0.3 nm), single-layer graphene can absorb ~2.3% white light. For few-lay graphene, its optical absorption is proportional to its number of layers. Owing to Pauli blocking, saturable absorption with ultrafast responses down to 100 fs can be observed. There is always an electron-hole pair in resonance for any excitation, due to the linear dispersion of the Dirac electrons. Therefore, graphene is an ideal ultra-broadband SA material for ultrafast pulse generation.

Since the first demonstration of graphene SAs in 2009 [42, 43], research on graphene has been progressing rapidly in Q-switched and mode-locked fiber lasers to facilitate pulse generation [19]. Scientists were attracted by its relatively easy fabrication techniques and the possibility of adopting methods previously developed for CNT-based fiber lasers. Compared with other SAs such as SESAMs and CNTs, graphene has intrinsic ultra-broadband operation ranging from the ultraviolet to the far-infrared region, due to its linear energy dispersion relation [20], along with low saturation intensity and ease of fabrication. In addition, graphene SAs are suitable for ultrafast pulse generation, owing to its ultrafast response time (around a few 100 fs). However, graphene SAs are not wavelength independent; the saturation fluence is higher at shorter wavelength, which favors the use of graphene SAs in the near-IR regions. Moreover, the low modulation depth, which is typically around 1% [44], is another challenge for single-layer graphene SA. Despite stacking multiple single layers of graphene SA can improve the modulation depth, it will also introduce more saturation fluence for more wavelength dependence.

2.5 Summary

In this chapter, we began with the definition of glass along with properties of different glasses (silica and ZBLAN). Then we introduced the rare-earth doping including some key parameters as well as the energy level of Thulium ions. Three- and four-energy level systems are shown as follows. Different fiber laser cavities including the ring and linear (DFB and DBR) configurations are also presented. At last, we described the properties of the newly exploited SA—graphene.

Chapter 3

Continuous wave Tm-doped fiber lasers at 0.81 µm, 1.48 µm and 1.9 µm

3.1 Introduction

Recently ZBLAN fiber has drawn increasing attention due to its unique advantages such as low phonon energy, high stability and mid-IR transparency. Compared with silicate and phosphate fiber, ZBLAN fiber is an excellent host for rare-earth ions to generate lasing covering from UV to mid-IR regions, where emission is difficult to be obtained from silicate and phosphate fiber. Compared with chalcogenide fiber with broader transmission window, ZBLAN fiber allows high doping levels (up to 10 mol%), high stability, high strength and low background loss (<0.05 dB/m). Especially Tm^{3+}:ZBLAN fiber laser can produce UV and visible upconversion emission at 284 nm, 350 nm, 365 nm, 455 nm, 480 nm and 515 nm through transitions $^1I_6 \rightarrow {}^3H_6$, $^1I_6 \rightarrow {}^3F_4$, $^1D_2 \rightarrow {}^3H_6$, $^1D_2 \rightarrow {}^3F_4$, $^1G_4 \rightarrow {}^3H_6$, respectively, as shown in Fig. 2.1. In the infrared region, three radiative de-excitation transitions from the $^3H_4$ level emit at ~810 nm, ~1480 nm and ~2300 nm, while emission at ~1900 nm results from the transition $^3F_4 \rightarrow {}^3H_6$.

In this chapter, we will discuss a dual-band CW Tm^{3+}:ZBLAN fiber laser at 810 nm and 1487 nm using a single linear cavity, as well as a dual-band three-wavelength CW Tm^{3+}:ZBLAN fiber laser at 1460 nm, 1503 nm and 1873 nm using two separate linear cavities along with one common branch. Then, we will present a widely tunable and switchable CW dual-wavelength Tm^{3+}:silica fiber laser based on the Sagnac loop mirror.

3.2 Dual-band CW Tm^{3+}:ZBLAN fiber laser

The $^3H_4 \rightarrow {}^3H_6$ transition with resulting lasing emission at ~810 nm corresponds to the first tele-communication window, which is applicable for short-distance transmission. The $^3H_4 \rightarrow {}^3F_4$

transition with resulting lasing emission at ~1480 nm is located in the S-band of the third tele-communication window, which is an ideal pump source for EDFAs and Raman amplifiers. Also the ~1480 nm lasing line can be applied to water detection in various liquids as it coincides with an absorption peak of liquid water. In addition, using a dual-band fiber laser located in the first and third tele-communication windows can provide a more compact approach without the use of any additional wavelength multiplexing, as both lasing wavelengths are produced from a single fiber. Furthermore, the $^3F_4 \rightarrow {}^3H_6$ transition with resulting lasing emission at ~1900 nm around the eye-safe region coincides with the absorption line of the OH overtone, which is important for chemical sensing and medical applications. Also lasing operation at ~1900 nm can be applied for the newly exploited fiber transmission window from 1850 nm to 2100 nm [5], and as pump sources for supercontinuum operation in the mid-IR region [45].

Dual band laser sources have widespread applications on nonlinear frequency conversion [46], multi-color pump-probe processes [47] and Raman scattering spectroscopy [48]. A laser operating simultaneously in two wavelength bands can provide new capabilities and enhanced functionality in LIDAR, microwave generation and dual-band OCT imaging spectroscopy. Many different schemes of dual-band fiber lasers have been proposed with two different gain media and wavelength-selecting mechanical filters to achieve two lasing lines, inducing less flexibility, high cost, complexity and limited stability [49, 50]. Previously, Liu *et al*. [51] reported a C- and L-band dual-wavelength Erbium-doped fiber laser operating from ~1520 nm to ~1635 nm to assist four-wave mixing self-stability. Lee *et al*. [52] presented a simultaneous dual-band wavelength-swept fiber laser at the 1310 nm and 1550 nm bands based on active mode locking. Boullet *et al*. [53] demonstrated a dual-band Er/Yb co-doped fiber laser at the 1060 nm and 1550 nm bands to generate tunable coherent light in the red spectral range. However, there are seldom reports on the dual-band ZBLAN all-fiber laser sources at the 810 nm, 1480 nm, or 1900 nm bands.

In this section, we focus on the use of a single gain medium, Tm^{3+}:ZBLAN fiber, along with FBGs as reflectors to demonstrate (1) a dual-band CW Tm^{3+}:ZBLAN fiber laser at 810 and 1487 nm using a single 1064 nm pump, and (2) a dual-band CW Tm^{3+}:ZBLAN fiber laser at 1460/1503 nm using a 1064 nm pump and at 1873 nm using a 1560 nm pump. These dual-band laser sources will find important applications in communications, instrumentation, spectroscopy and chemical sensing.

3.2.1 Dual-band CW Tm^{3+}:ZBLAN fiber laser at 810/1487 nm

A. Experimental setup

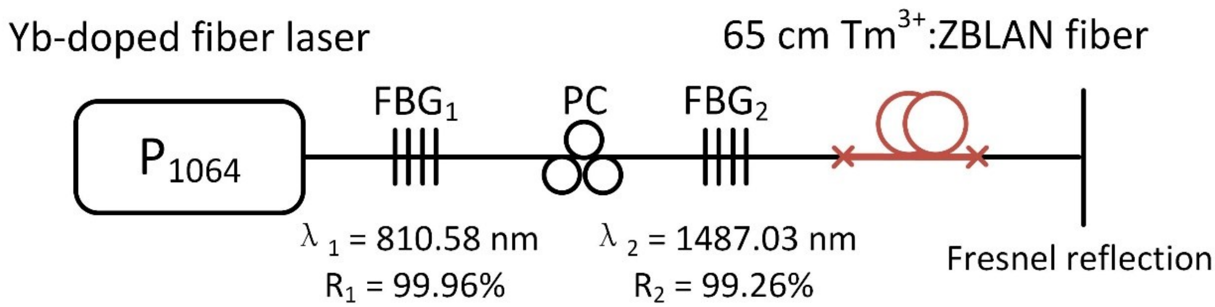

Fig. 3.1 Configuration of dual-band CW Tm^{3+}:ZBLAN fiber laser at 810 nm and 1487 nm.

Fig. 3.1 shows the schematic of the dual-band CW Tm^{3+}:ZBLAN fiber laser at 810 nm and 1487 nm. An Ytterbium-doped multi-mode fiber laser (YDFL, P_{1064}) at 1064 nm is employed as the pump source for the $^3H_4 \rightarrow {}^3H_6$ transition at 810 nm, along with the $^3H_4 \rightarrow {}^3F_4$ transition at 1487 nm, as shown in Fig. 3.2. No WDM coupler is used to separate the pump and the lasing signals. The gain medium is a 65 cm length of Tm^{3+}:ZBLAN fiber. Manufactured by IRphotonics/Thorlabs, the double cladding (DC) Tm^{3+}:ZBLAN fiber has a doping concentration of 8,000 ppm Tm^{3+} ions and a numerical aperture (NA) of 0.13, has an 8 μm core diameter, a 125 μm cladding diameter with a 15 μm coating of mixed fluoroacrylate and acrylate. The Tm^{3+}:ZBLAN fiber is coupled with silica-based SMF-28 fiber through mechanical splices, which are represented by × as shown in Fig. 3.1. Each pair of mechanical splices induce around 2 dB loss. Note that the mechanical splicing can be replaced by laser splicing [54] or filament splicing in order to further reduce the splicing losses between ZBLAN and silica fiber. In addition, Tm^{3+}:ZBLAN fiber supports single-mode operation at ~1487 nm, but it supports multi-mode operation at ~810 nm.

The dual-band operation is realized by two separate cavities. Each cavity is defined by one FBG as a reflector on one end, and a 4% Fresnel air reflection is used to form the other end of cavity. For 810 nm lasing cavity, written in SM-780-HP fiber, FBG_1 with a center wavelength of 810.58 nm, a bandwidth of 0.2 nm and peak reflectivity of 99.96% is used for single-mode lasing operation at 810 nm. For 1487 nm lasing cavity, written in SMF-28 fiber, FBG_2 with a center wavelength of 1487.03 nm, a bandwidth of 0.4 nm and peak reflectivity of 99.26% is employed. FBG_1 is placed outside of the 1487 nm lasing cavity as SM-780-HP fiber is optimized to operate around 810 nm, but has a high transmission loss at 1487 nm. The second mode cut-off wavelength of SM-780-HP fiber is 730±30 nm, so FBG_1 only supports single mode operation around 810 nm. In addition, as the emission cross section at 810 nm is much larger than that at 1487 nm, more insertion losses are induced inside the 810 nm lasing cavity by placing the FBG_1 before FBG_2. Furthermore, a polarization controller (PC) is placed between FBG_1 and FBG_2 in order to balance the output power of two lasing signals and optimize the intra-cavity polarization.

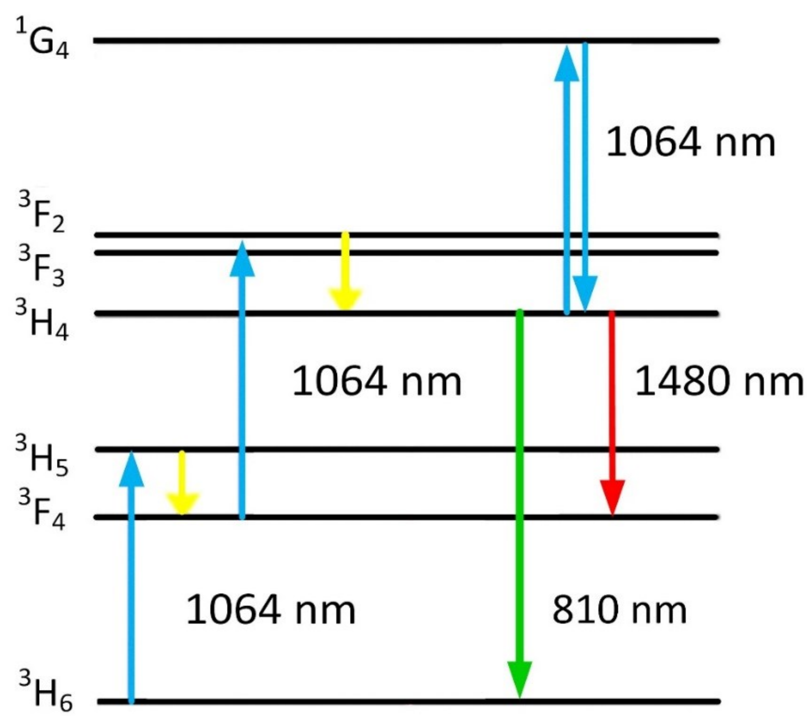

Fig. 3.2 Energy level transitions when pumped at 1064 nm to produce dual-band lasing emission at ~810 nm and ~1480 nm.

The 4% Fresnel air reflection is created as the output coupler by placing two cleaved facets from fiber pigtails on two XYZ translation stages. One fiber pigtail is connected to the Tm^{3+}:ZBLAN fiber, while the other fiber pigtail is connected to an optical spectrum analyzer (OSA, HP70952) with a power limit of ~15 dBm and wavelength scanning range from 600 nm to 1700 nm. Using a microscope, the two translation stages are employed to align the two facets to maintain an air gap with a loss of ~10 dB in order to limit the optical power injected into the OSA. The OSA is used to measure the output power at each wavelength, as there is no WDM coupler to separate the pump along with two lasing signals. The pump power is measured by the power meter (Thorlabs, PM100D) along with a thermal power sensor (Thorlabs, S302C) with a wavelength range from 0.19 μm to 25 μm and a resolution of 1 μW.

B. Results and discussion

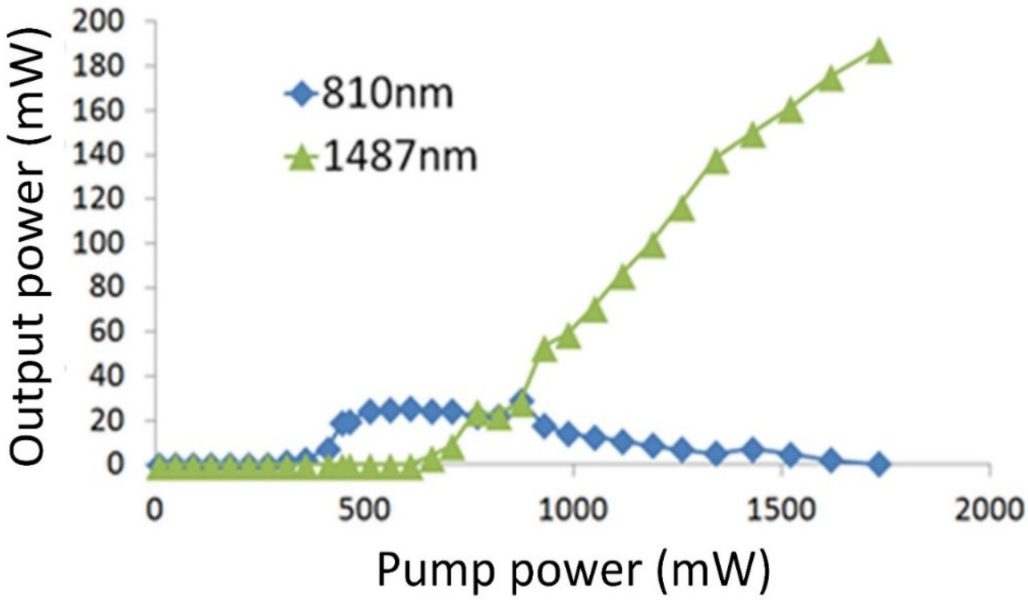

Fig. 3.3 Measured output powers at 810 nm and 1487 nm as a function of the pump power. Lasing wavelengths at 810 nm and 1487 nm are shown as blue diamond and green triangles, respectively.

For our experiment, the results are measured by sweeping the DC power supply's current from 1 A to 7 A with steps of 0.2 A, which equals an average increment of 25 mW of pump power. By carefully tuning the PC inside the cavity, dual-band lasing operation at 810 nm and 1487 nm is achieved. The results shown here are measured with a fixed position of PC. Fig. 3.3 shows the output powers at 810 nm and 1487 nm as a function of the pump power. Lasing operation at 810 nm starts first at a threshold of 355 mW, mainly due to the relative larger emission cross section at 810 nm. Then lasing at 810 nm continues to increase with a slope efficiency of 15% up to a saturated output power of 25 mW. Lasing at 1487 nm appears at a pump power of 656 mW with lasing at 810 nm simultaneously. When 766 mW < P_{1064} < 873 mW, the laser emits at both 810 nm and 1487 nm with approximately equal output powers. As P_{1064} increases further up to 1730 mW, the output power at 1487 nm increases to a maximum output power of 188 mW with a slope efficiency of 18.6%, while the output power at 810 nm gradually decreases down to zero. When P_{1064} = 1730 mW, only single-wavelength lasing operation at 1487 nm is observed. Since lasing at 1487 nm is four-energy-level with a higher efficiency while lasing at 810 nm is three-energy-level, most of the pump power is used to generate lasing at 1487 nm, and lasing at 810 nm disappears. In order to protect the mechanical splices between the Tm^{3+}:ZBLAN fiber and SMF-28 fiber, the maximum pump power used is controlled as 1730 mW. But we believe that if the splicing between the Tm^{3+}:ZBLAN fiber and SMF-28 fiber can handle more optical power, single-wavelength lasing operation at 1487 nm would continue as the pump power increases above 1730 mW.

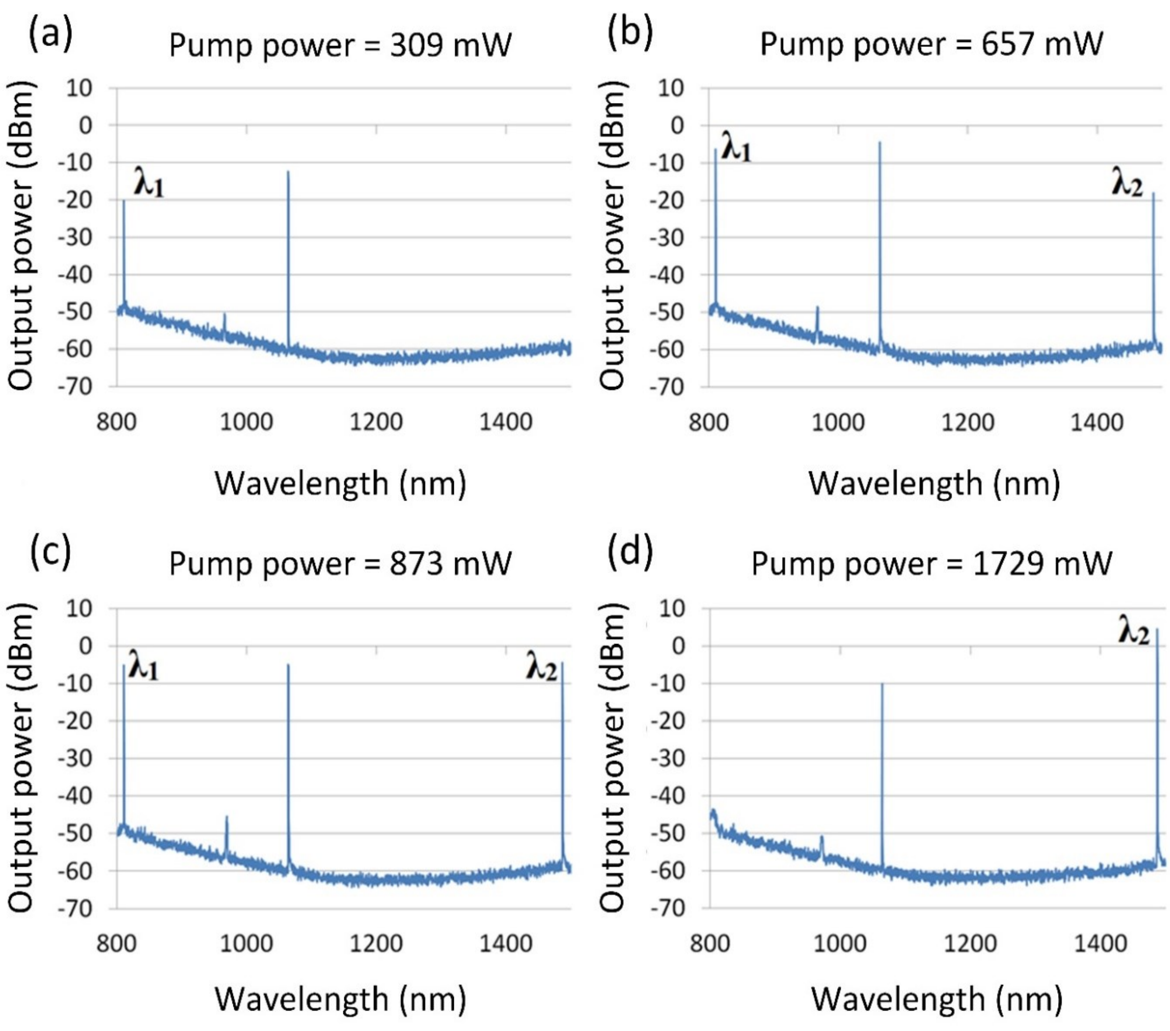

Fig. 3.4 Evolution of optical output spectra for different pump powers: (a) single-wavelength lasing operation at λ_1; (b) dual-wavelength lasing operation when λ_2 is just above threshold; (c) dual-wavelength lasing operation with approximately equal output power; (d) single-wavelength lasing operation at λ_2.

Fig. 3.4 shows the optical output spectra evolution of the lasing operation at λ_1 and λ_2. Note that these spectra are applied by ~10 dB loss from the air gap to protect the OSA; two peaks at 980 nm and 1064 nm result from the Yb-doped fiber laser pump. A FBG centered at 1064 nm is expected to remove the pump signal from the total output.

C. Summary

Using a linear cavity configuration without the use of WDM coupler, dual-band lasing at 810 nm and 1487 nm is achieved. These dual-band lasing shares the same upper energy level $^3H_4$, but supports two different lasing transitions, the $^3H_4 \rightarrow {}^3H_6$ transition at 810 nm and the $^3H_4 \rightarrow {}^3F_4$ transition at 1487 nm, simultaneously. By controlling the 1064 nm pump power, single-wavelength operation at 810 nm or 1487 nm, and dual-wavelength operation at both wavelengths are observed. Each wavelength can emit an output power more than 25 mW. Such a dual-band laser located in the first and third tele-communication windows may find important applications in bio-sensing, communication and instrumentation.

3.2.2 Dual-band CW Tm^{3+}:ZBLAN fiber laser at 1460/1503 and 1873 nm

A. Experimental setup

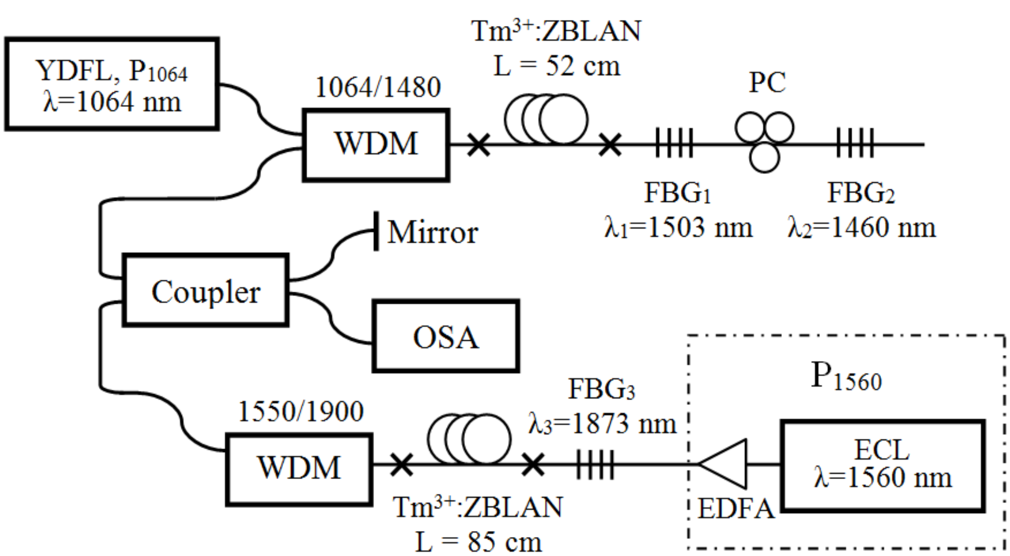

Fig. 3.5 Tm^{3+}:ZBLAN three-wavelength fiber laser configuration.

Fig. 3.5 shows a schematic of the Tm^{3+}:ZBLAN three-wavelength fiber laser. It consists of two independent branches, which generate dual-band lasing at 1460/1503 nm (top) and 1873 nm (bottom), respectively, as well as a third shared branch which combines the above two linear cavities and functions as the output. The gain fiber for lasing operation at 1460/1503 nm is a 52 cm Tm^{3+}:ZBLAN fiber, while the gain fiber for lasing operation at 1873 nm is an 85 cm Tm^{3+}:ZBLAN fiber. As before, these two lengths of gain fiber are the same DC Tm^{3+}:ZBLAN fiber, which are coupled to the SMF-28 fiber through mechanical splices (represented by $\times$ in Fig. 3.5), inducing around 2 dB loss per pair.

In the top branch, a 1064 nm YDFL (P_{1064}) is employed for the $^3H_4 \rightarrow {}^3F_4$ transition at ~1480 nm. The pump is coupled via a 1064/1480 nm WDM coupler into a 52 cm Tm^{3+}:ZBLAN gain fiber. The cavity is formed on one end by two FBGs (FBG_1 and FBG_2), which serve as the wavelength selectors to define the lasing wavelengths. FBG_1 has a center wavelength of λ_1=1503 nm with a 3-dB bandwidth $\Delta\lambda_1$ of 0.15 nm, and FBG_2 has a center wavelength of λ_2=1460 nm with a 3-dB bandwidth $\Delta\lambda_2$ of 0.486 nm. A PC is put between FBG_1 and FBG_2 in order to adjust intra-cavity polarization and to equalize the output powers generated at λ_1 and λ_2.

In the bottom branch, a 1560 nm pump (P_{1560}) consisting of an external cavity laser (ECL) and an EDFA is used to pump directly through FBG_3 into an 85 cm length of Tm^{3+}:ZBLAN fiber. The cavity is formed on one end by FBG_3 with a center wavelength of λ_3=1873 nm and a 3-dB bandwidth $\Delta\lambda_3$ of 0.3 nm. These above three FBGs in the setup are all written in SMF-28 fiber with peak reflectivities above 99%. A 1550/1900 nm WDM coupler is employed to eliminate the residual pump power.

These two branches are both connected with a third shared branch including an optical coupler and a common gold-tipped fiber mirror. The optical coupler has a splitting ratio of 50:50 at 1460/1503 nm, and a splitting ratio of 87:13 at 1873 nm (87% to the gold-tipped fiber mirror). One port of the optical coupler is connected with the gold-tipped fiber mirror as the reflector to form the other end of their respective cavities. The common gold-tipped fiber mirror has a reflectivity above 90% for all the three lasing wavelengths. The other port of the optical coupler is connected with an OSA (Yokogawa, AQ6375) to measure the optical output for all the three lasing wavelengths. The OSA has a scanning range from 1200 nm to 2400 nm with a resolution bandwidth of 0.05 nm. The pump power is measured by the same power meter as used in previous experiments.

B. Results and discussion

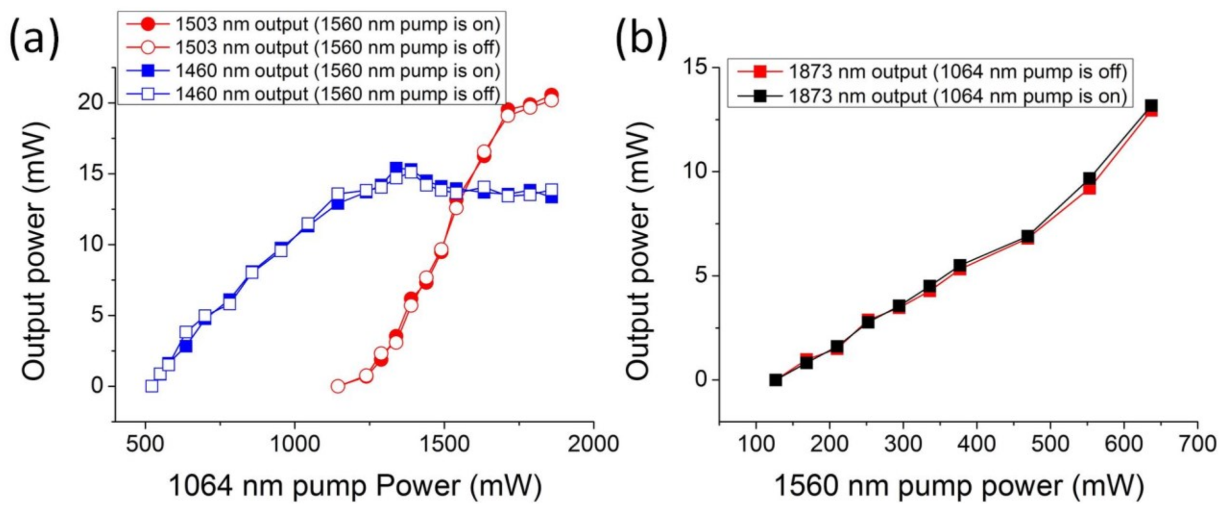

Fig. 3.6 Measured output powers (a) at 1460 nm (blue squares) and 1503 nm (red circles) as a function of P_{1064} when P_{1560} is on (solid symbols) and off (open symbols); (b) at 1873 nm as a function of P_{1560} when P_{1064} is on (black square) and off (red square).

Fig. 3.6 shows the measured output powers at 1460 nm and 1503 nm as a function of 1064 nm pump power, along with the output power at 1873 nm as a function of 1560 nm pump power. We first characterize the two branches operating independently. For the top branch, as shown in Fig. 3.6(a), lasing at 1460 nm starts first when P_{1064} exceeds a threshold of 522 mW. As P_{1064} is increased further, single-wavelength at 1460 nm continues to increase with a slope efficiency of 2.2% up to a saturated output power of 15 mW. When P_{1064} reaches a threshold of 1144 mW, lasing at 1503 nm appears and increases with a slope efficiency of 3.4%. As 1144 mW $< P_{1064} <$ 1580 mW, the laser operates at both wavelengths, and lasing operation at 1460 nm has a higher output power. When P_{1064} is increased to ~1580 mW, dual-wavelength lasing at both wavelengths emits with approximately equal output powers of ~15 mW. As P_{1064} is increased further up to 1859 mW, output power at 1460 nm keeps a saturated level of 15 mW, while output power at 1503 nm continues to increase up to a maximum output of 21 mW, as the emission cross section at 1460 nm is higher than that at 1503 nm. In order to protect the mechanical splices between the Tm^{3+}:ZBLAN fiber and SMF-28 fiber, P_{1064} is controlled below 1859 mW. But if higher pump power at 1064 nm is applied, higher output power at 1503 nm would be expected. For the bottom branch, as shown in Fig. 3.6 (b), lasing at 1873 nm occurs at a threshold of 126 mW, and continues to increase with P_{1560} with a slope efficiency of 2.5%. When P_{1560} is 637 mW, the maximum output power at 1873 nm is ~13 mW.

Following this, we re-measure the output powers at 1460 nm and 1503 nm when lasing output at 1873 nm is set to operate at 6.8 mW, as well as the output power at 1873 nm when lasing outputs at 1460 nm and 1503 nm are set to operate at 13.17 mW and 13.95 mW, respectively. As shown in Fig. 3.6(a) and (b), the output curves are identical regardless whether the other pump is on or off, demonstrating that the laser cavities of the two branches work independently.

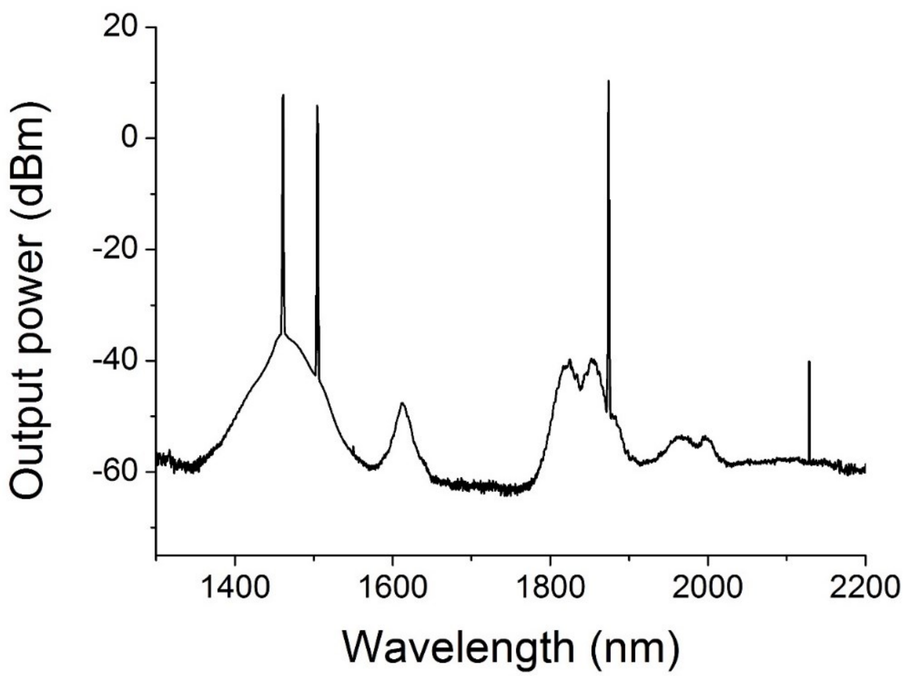

Fig. 3.7 Optical output spectrum for three-wavelength operation when P_{1064}=1520 mW and P_{1560}=480 mW.

Fig. 3.7 shows the optical output spectrum of the three lasing wavelengths at 1460 nm, 1503 nm and 1873 nm when P_{1064}=1520 mW and P_{1560}=480 mW. These three lasing lines are measured with peak values all above 5 mW. Note that the lasing peak at 2128 nm results from the higher-order diffraction of P_{1064}.

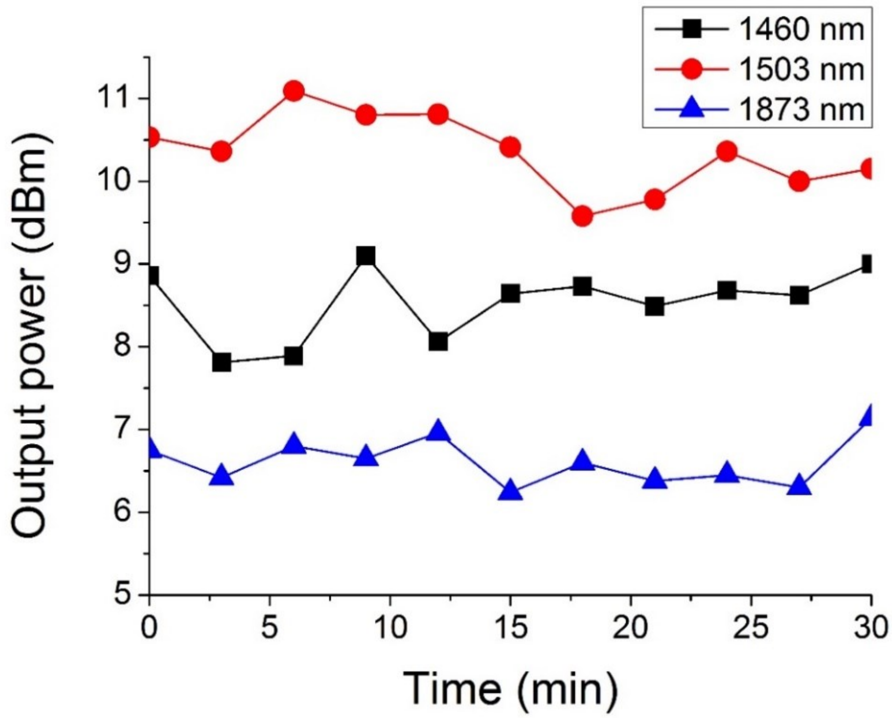

Fig. 3.8 Output power fluctuations of three lasing wavelength when P_{1064}=1650 mW and P_{1560}=480 mW. Three lasing wavelengths λ_1, λ_2 and λ_3 are shown as black squares, red circles and blue triangles, respectively.

Fig. 3.8 shows the output power fluctuations of the three lasing wavelengths over 30 minutes. The power fluctuations of the three lasing wavelengths are observed all less than 1.5 dB, indicating three relatively stable lasing outputs. These power fluctuations mainly result from the environmental variations, gain competition, and mechanical splices between the Tm^{3+}:ZBLAN fiber and SMF-28 fiber. By replacing the mechanical splices with the fusion splices, we expect the laser's stability, as well as corresponding slope efficiency, could be further improved. Furthermore, environmental influences can be reduced by packaging the laser in order to improve the stability. Finally, using cascaded cavities [16] or inhomogeneous loss mechanisms [55] can reduce the gain competition between wavelengths sharing the same gain fiber.

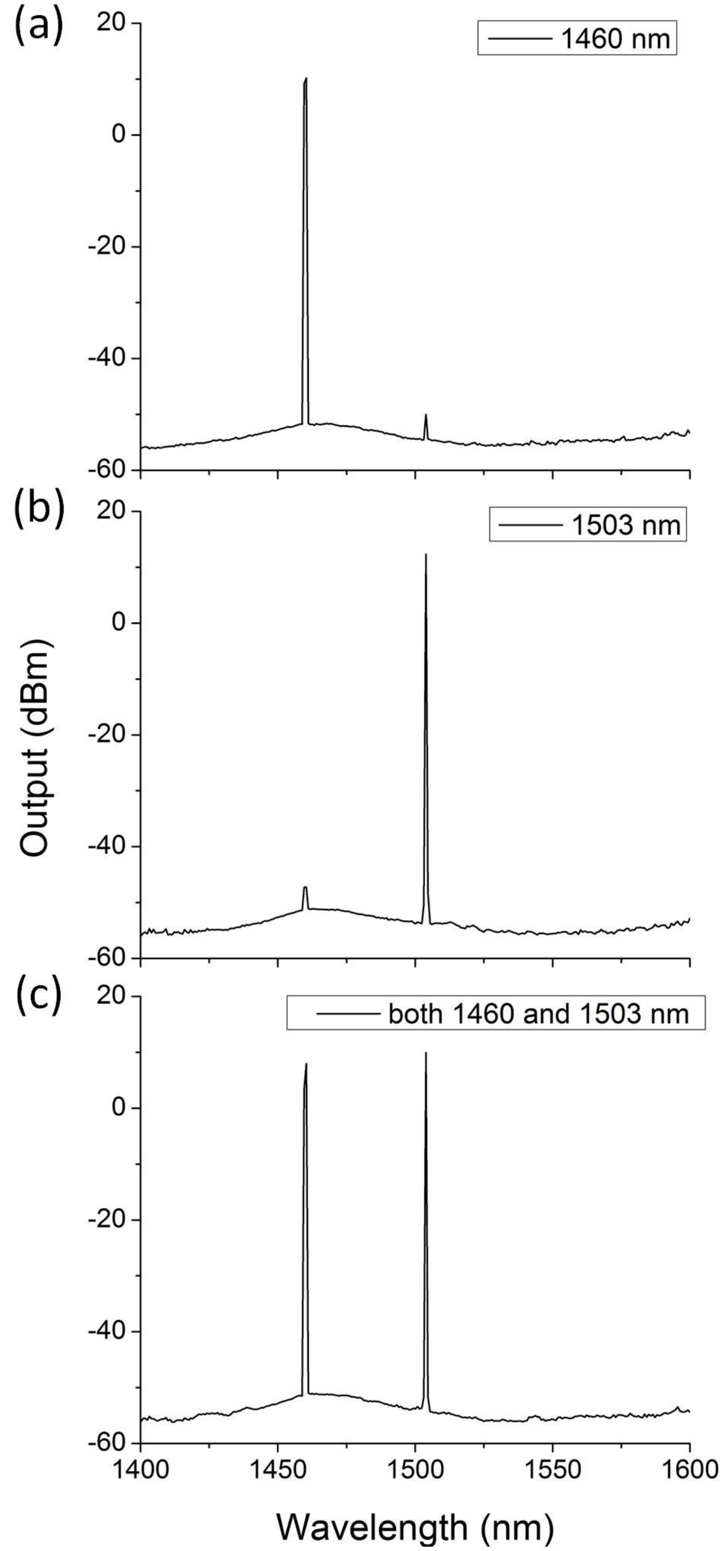

Fig. 3.9 Optical output spectra showing switchable operation at (a) 1460 nm; (b) 1503 nm; (c) both 1460 and 1503 nm.

For the top branch, switchable dual-wavelength operation can be obtained by carefully adjusting the polarization state of the top cavity. As shown in Fig. 3.9, when P_{1064} is set to ~1.7 W, the Tm^{3+}:ZBLAN fiber laser can be switched to operate at single-wavelength at 1460 nm or 1503 nm, or dual-wavelength at 1460 nm and 1503 nm. In addition, tuning the PC plays an important role in realizing the dual-wavelength lasing operation simultaneously; without the PC, the gain competition would only allow 1460 nm to lase. If the positions of FGB_1 and FGB_2 are reversed, no dual-wavelength lasing operation is observed even by tuning the PC, as the emission cross section at 1460 nm is higher than that at 1503 nm.

C. Summary

We have demonstrated a three-wavelength Tm^{3+}:ZBLAN fiber laser emitting simultaneously at 1460 nm, 1503 nm and 1873 nm. Its power fluctuations at three wavelengths are less than 1.5 dB over 30 minutes. Also switchable dual-wavelength operation at 1460 nm and 1503 nm is obtained. Such a three-wavelength fiber laser has been successfully applied in the sensing application in single-pass absorption measurements for detecting and quantifying water concentration in acetone [24].

3.3 Widely tunable and switchable dual-wavelength CW Tm^{3+}:silica fiber laser at 1900 nm

Near-IR Tm^{3+}:silica fiber lasers (TDFLs) at eye-safe 1900 nm has potential applications in the fields of chemical sensing, medical surgery and atmospheric light detection and ranging (LIDAR) measurements. Features such as multi-wavelength operation, wavelength tunability and switchability offer enhanced functionality and new flexibility in different applications.

Previously, a number of tunable single-wavelength TDFLs have been reported. Clarkson *et al*. reported a cladding-pumped tunable TDFL from 1860 nm to 2090 nm based on grating filters [56]. Ma *et al*. demonstrated a tunable TDFL based on optofluidically tunable multimode interference fiber filters [57]. Li *et al*. presented a wavelength selectable TDFL based on different FBGs [58]. Li *et al*. realized an ultra-wideband tunable TDFL with a continuous tuning range as large as 250 nm [59]. There are also a number of reports on the dual-wavelength TDFLs using FBGs [9, 60, 61]. Tunable spacing between the dual lasing wavelengths was achieved using cascaded FBGs in a nonlinear amplifier loop mirror [60] or volume Bragg gratings [62]. Tunable dual-wavelength operation with a fixed wavelength spacing was demonstrated with a limited tuning range of ~ 7 nm [61]. Moreover, alternate switching between single- and dual-wavelength operation was investigated by adjusting a PC in a linear cavity incorporating FBGs in high birefringence (Hi-Bi) fiber as wavelength selective elements [9]. TDFLs with Sagnac loop mirrors as comb filters incorporating a length of Hi-Bi fiber were also demonstrated [63, 64]. Alternate switching between single- and multiple- wavelengths with a tuning range of up to 20 nm is obtained. However, until now there is no report to demonstrate the capability to provide both alternate wavelength switching and tunable multi-wavelength operation over a broad wavelength range (>50 nm).

In this section, we present a broadly tunable and switchable dual-wavelength Tm^{3+}:silica fiber laser at 1900 nm. A ring configuration with a comb filter based on a Sagnac loop incorporating a length of Hi-Bi fiber is employed to define the lasing wavelengths. A polarization dependent isolator (PDI) is used to suppress mode competition [65, 66], as well as to provide polarization selectivity for tunable and stable dual-wavelength operation. By simple control of a PC in the laser cavity, we realize tunable and alternate wavelength-switching over an operating range of 70 nm from 1857 nm to 1927 nm. This is the largest tuning range reported on a dual-wavelength Tm^{3+}:silica fiber laser.

3.3.1 ASE measurement

The schematics of the forward and backward ASE measurement of Tm^{3+}:silica fiber are shown in Fig. 3.10(a) and (b), respectively. The active fiber used in the two setups is a 30 cm length of DC Tm^{3+}:silica fiber manufactured by CorActive. The gain fiber is doped with 40,000 ppm Tm^{3+}, has a 6 μm core diameter with a core NA of 0.23, a 125 μm cladding diameter with a cladding NA larger than 0.45, and is coated with 67.5 μm of acrylate. The fiber's clad absorption coefficient at 790 nm is ~1.4 dB/m. The Tm^{3+}:silica gain fiber is coupled to the SMF-28 fiber pigtails through fusion splices with a loss of ~0.9 dB per pair, and is pumped by a 1560 nm pump source. The 1560 nm pump consists of a 1560 nm external cavity laser and a high-power EDFA with a maximum launched output power of 2 W. Compared with 800 nm or 1060 nm pumping, the gain fiber is pumped at 1560 nm due to a relatively higher photon conversion efficiency [67]. In Fig. 3.10(a), the 1560 nm source is directly pumped into Tm^{3+}:silica fiber, and then through a 1560/1900 nm WDM coupler. An OSA (Yokogawa, AQ6375) is connected to the pass port of WDM for the forward ASE output measurement, while the residual 1560 nm pump power is coupled into the reflection port in order to protect the OSA. On the contrast, in Fig. 3.10(b), the 1560 nm source is pumped through WDM first, and then coupled into Tm^{3+}:silica fiber. The OSA is connected to the pass port of WDM to measure the backward ASE output.

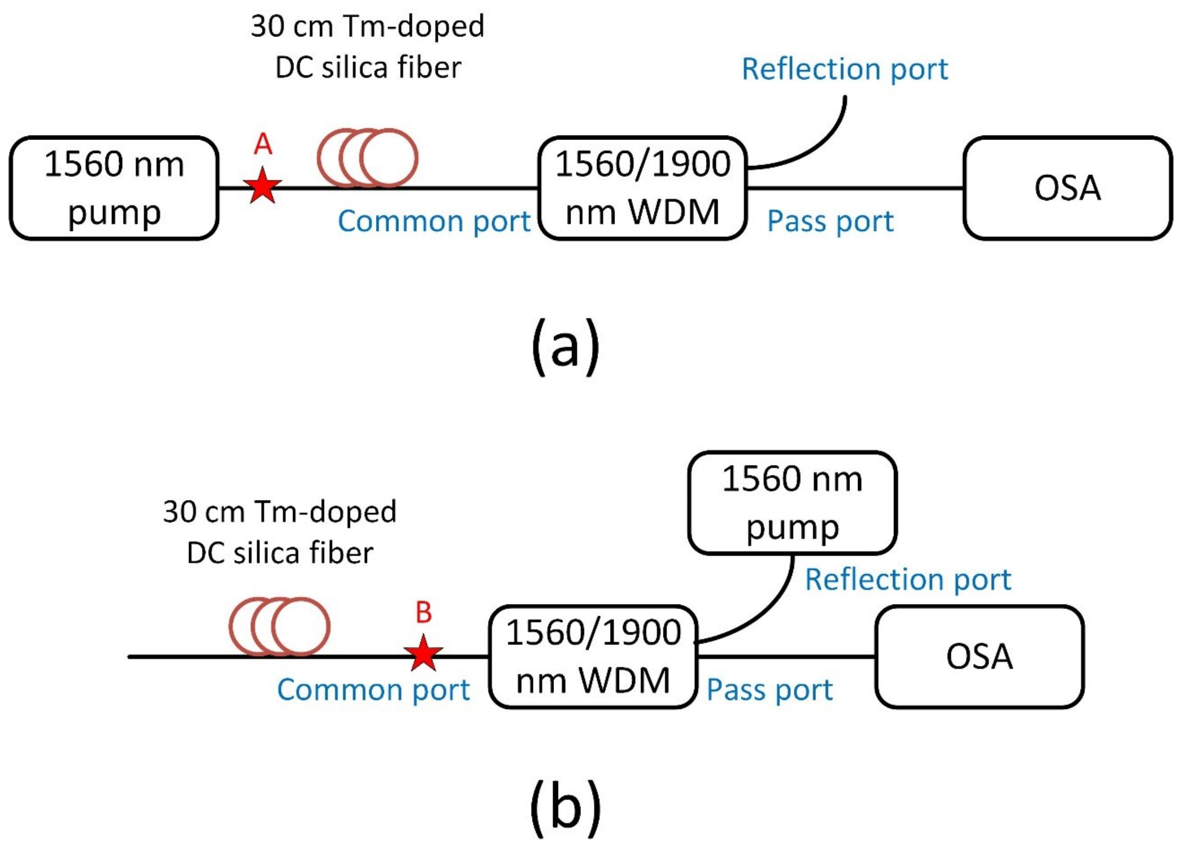

Fig. 3.10 Experimental setup of the Tm^{3+}:silica fiber ASE measurement based on (a) forward and (b) backward output.

Fig. 3.11 shows the forward and backward ASE spectra measured by the OSA at pump powers of 400 mW, 600 mW, 800 mW and 1000 mW, respectively. The 1560 nm pump powers are measured at Point "A" and "B" in order to provide the same launched power for further comparison. We can observe that both of the forward and backward ASE amplification regions increase as the 1560 nm pump power increases, but the ASE peaks remain unchanged at around 1860 nm. When the launched power is 1000 mW, the forward ASE spectrum spanning over 230 nm from ~1800 nm to ~ 2030 nm with an FWHM bandwidth of ~80 nm is achieved; on the other hand, the backward ASE spectrum covers over 230 nm from 1790 nm to 2020 nm with an FWHM bandwidth of ~70 nm. Moreover, due to larger cross-section and higher average inversion level, the total forward ASE output is higher than the backward one under the same input power. Therefore, the forward pumping scheme for Tm^{3+}:silica fiber is adopted for further investigation.

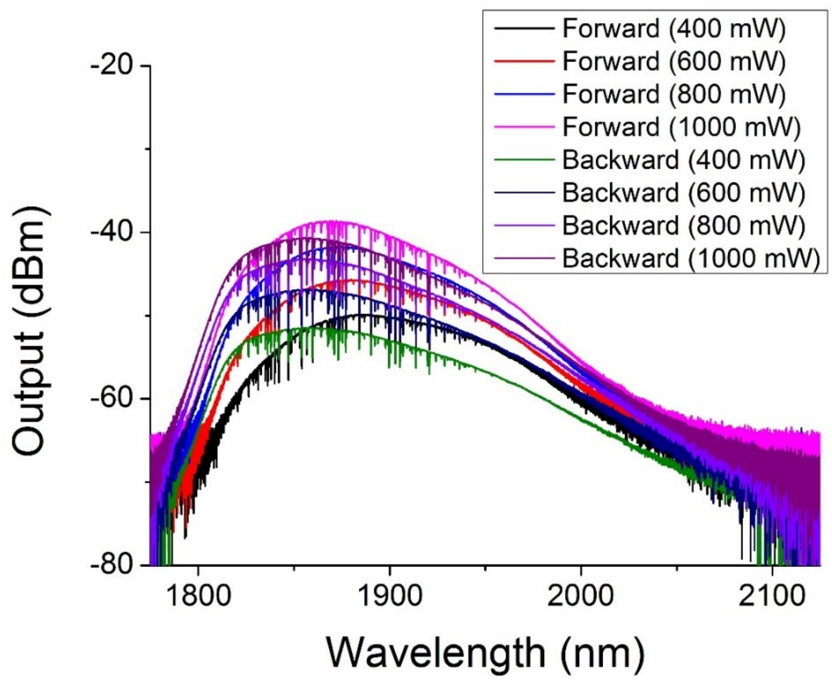

Fig. 3.11 Measured forward and backward ASE spectra of 30 cm Tm^{3+}:silica fiber under different 1560 nm pump powers.

Fig. 3.12 shows the measured forward ASE spectra with different lengths of Tm^{3+}:silica fiber when the 1560 nm pump power is set as 2 W. As the length of Tm^{3+}:silica fiber increases, the forward ASE peak shifts towards longer wavelength, and the corresponding FWHM bandwidth becomes slightly broader. From all the chosen lengths of Tm^{3+}:silica fiber, 30 cm fiber has a relatively higher ASE output. Therefore, the 30 cm length of Tm^{3+}:silica fiber is chosen as the gain fiber for the upcoming experiment.

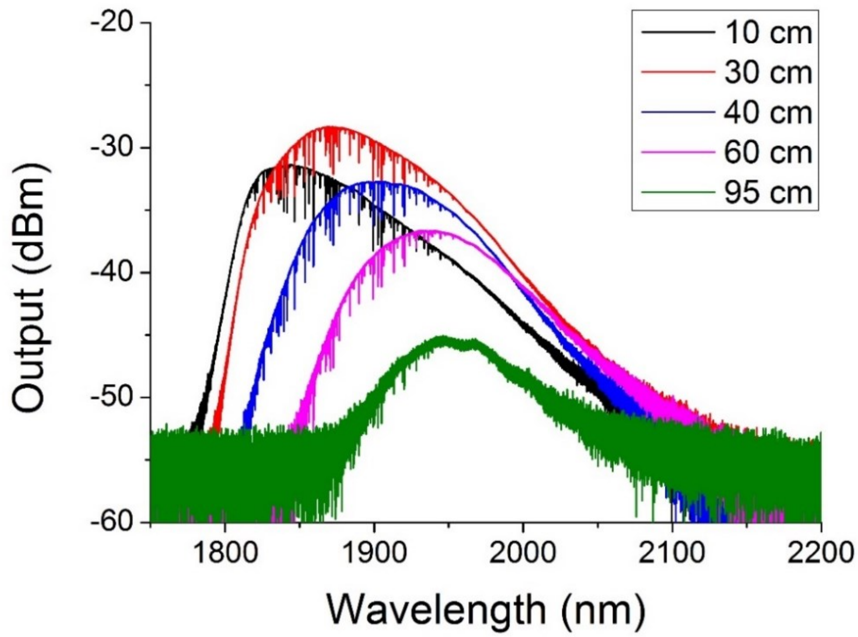

Fig. 3.12. Measured forward ASE spectra with different lengths of Tm^{3+}:silica fiber when the 1560 nm pump power is 2 W.

3.3.2 Hi-Bi loop mirror response

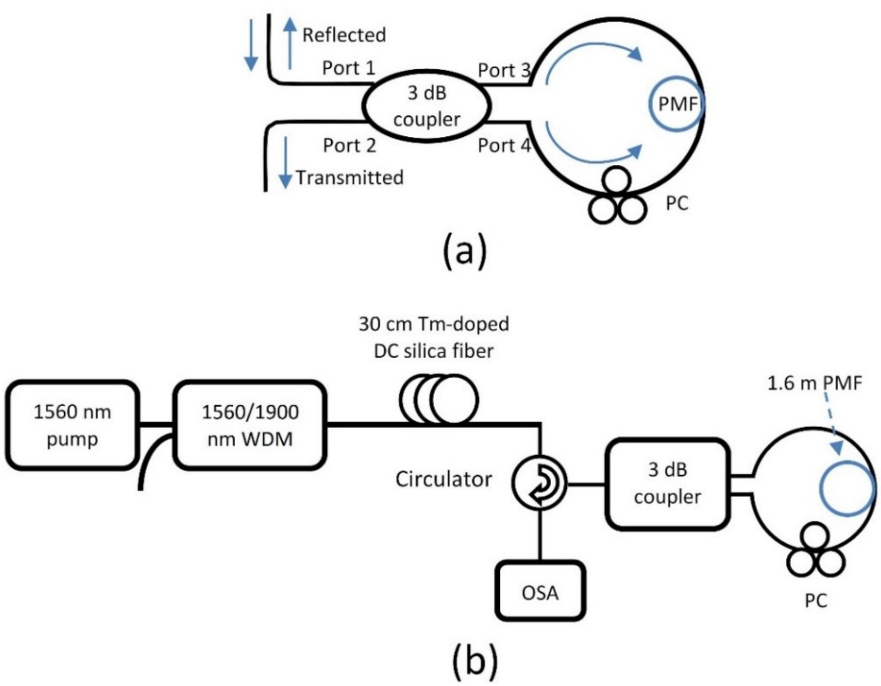

Fig. 3.13 (a) Configuration of the Sagnac loop mirror. (b) Experimental setup of the filter response measurement of the Sagnac loop mirror.

A Sagnac loop mirror, which serves as a wavelength filter, is shown schematically in Fig. 3.13(a). It consists of a 3 dB coupler at 1900 nm, PMF manufactured by Thorlabs Inc., and a PC. The principle of the Sagnac loop mirror as a wavelength filter is illustrated as follows. The input light at Port 1 is split into two counter-propagating beams by the coupler. After travelling through the Sagnac loop mirror, the clockwise beam from Port 3 and the counter-clockwise beam from Port 4 recombine at the coupler. As for an arbitrary polarized beam, it can always be decomposed into x-polarized and y-polarized components transmitted from the fast axis and slow axis, respectively. If no PC is placed into the Sagnac loop, two x-polarized (y-polarized) components on the fast (slow) axes experience the same optical path length after travelling clockwise and counter-clockwise around the loop. However, when the PC is placed into the Sagnac loop and set to produce a pure rotation of 90° as a half-wave-plate near Port 4, the results will be different. More precisely, the x-polarized component of the clockwise beam from Port 3 remains as the fast mode when travelling the Hi-Bi fiber, but is changed to the y-polarized component after the PC. On the other hand, the x-polarized component of the counter-clockwise beam from Port 4 becomes the y-polarized component after the PC and then transmits through the Hi-Bi fiber as the slow mode. Although these two components travel through the same fiber length, they suffer different optical lengths due to different modes. When they leave the coupler, these two counter-propagating x-polarized components interfere with a phase difference, $\delta\Phi=\Delta\beta L$, where $\Delta\beta=2\pi\Delta n/\lambda$ is the fiber modal birefringence with Δn as the normalized birefringence and λ as the wavelength, and L is the length of Hi-Bi fiber. Similarly, two counter-propagating y-polarized components also interfere at the coupler with an opposite phase difference $-\delta\Phi$. By using the Jones matrix theory described in [68], the reflectivity of the Hi-Bi loop mirror is approximately a periodic function of the wavelength, namely, $R(\lambda)=2K(1-K)[1+2\cos\delta\Phi(\lambda)]$, where K is the power coupling ratio of the coupler. When K=0.5, the Hi-Bi loop mirror has the largest contrast. The wavelength spacing of the Sagnac loop mirror is determined by the separation of the peaks in the reflectivity and is given by $\delta\lambda=\lambda2/(\Delta nL)$. If the PC produces a rotation not equal to 90°, only parts of the counter-propagating beams interfere and the reflectivity contrast decreases, but the wavelength spacing of the comb filter keeps unchanged.

Fig. 3.13(b) shows the experiment setup to measure the filter response of the Sagnac loop mirror. 1560 nm forward pumping scheme and 30 cm Tm^{3+}:silica DC silica fiber as gain medium are used to provide enough amplification at around 1900 nm. A circulator at 1900 nm is used to ensure unidirectional propagation. ASE at 1900 nm region are transmitted into the Hi-Bi loop mirror first, and then reflected back to an OSA. In the Sagnac loop, 1.6 m PMF is used to produce a ~5.4-nm wavelength spacing at 1900 nm. Fig. 3.14(a) shows the measured reflection response of the Sagnac loop mirror when the PC is adjusted to different angles. When the PC is set to produce no rotation to the input beam, the Sagnac loop mirror produces no comb filter response; on the other hand, when the PC is set to produce a 90° rotation as a half-wave-plate, it produces a comb filter response with the greatest peak-to-notch contrast (more than 20 dB). We also measure the reflection responses with the same length of Tm^{3+}:ZBLAN fiber and Tm^{3+}:silica fiber, as shown in Fig. 3.14(b). Both kinds of fiber produce the same ~5.4-nm wavelength spacing, but the Tm^{3+}:silica fiber has a broader bandwidth, albeit ZBLAN has a higher ASE output. Therefore, in order to realize a widely tunable and switchable multi-wavelength TDFL, we choose Tm^{3+}:silica fiber with a broader bandwidth as the gain fiber.

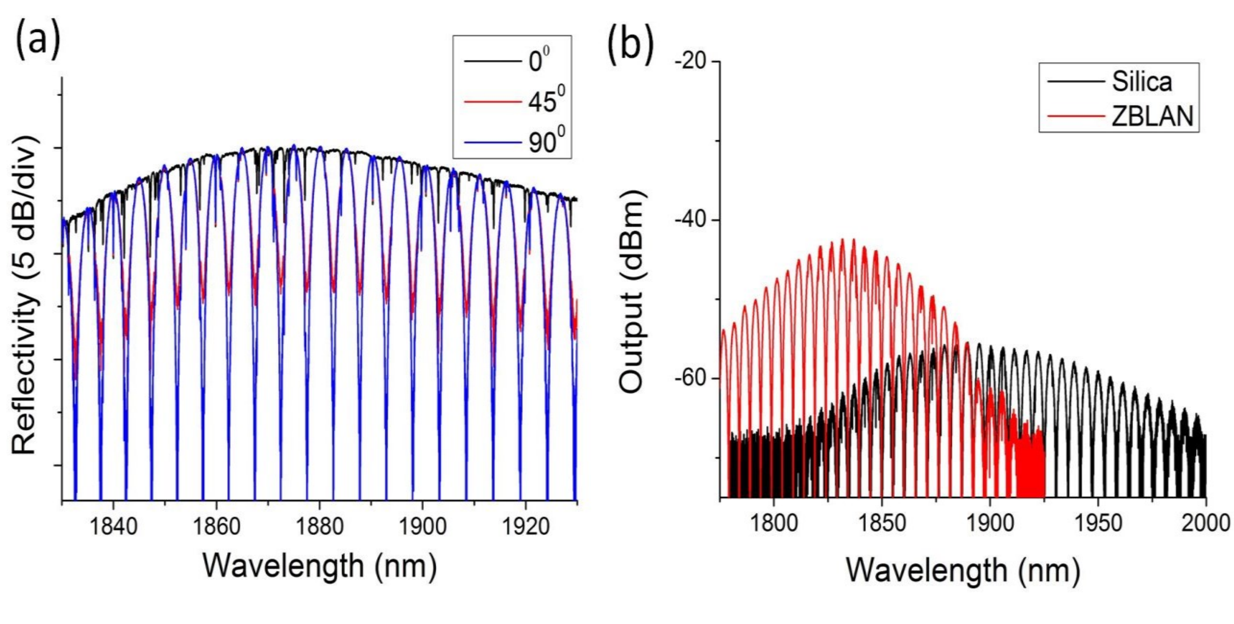

Fig. 3.14 Measured comb filter reflection response of (a) Tm^{3+}:silica fiber with PC set to provide rotations of 0°, 45° and 90°; (b) Tm^{3+}:silica and Tm^{3+}:ZBLAN fiber with PC set to provide a rotation of 90°.

3.3.3 Widely tunable and switchable lasing operation

A. Experimental setup

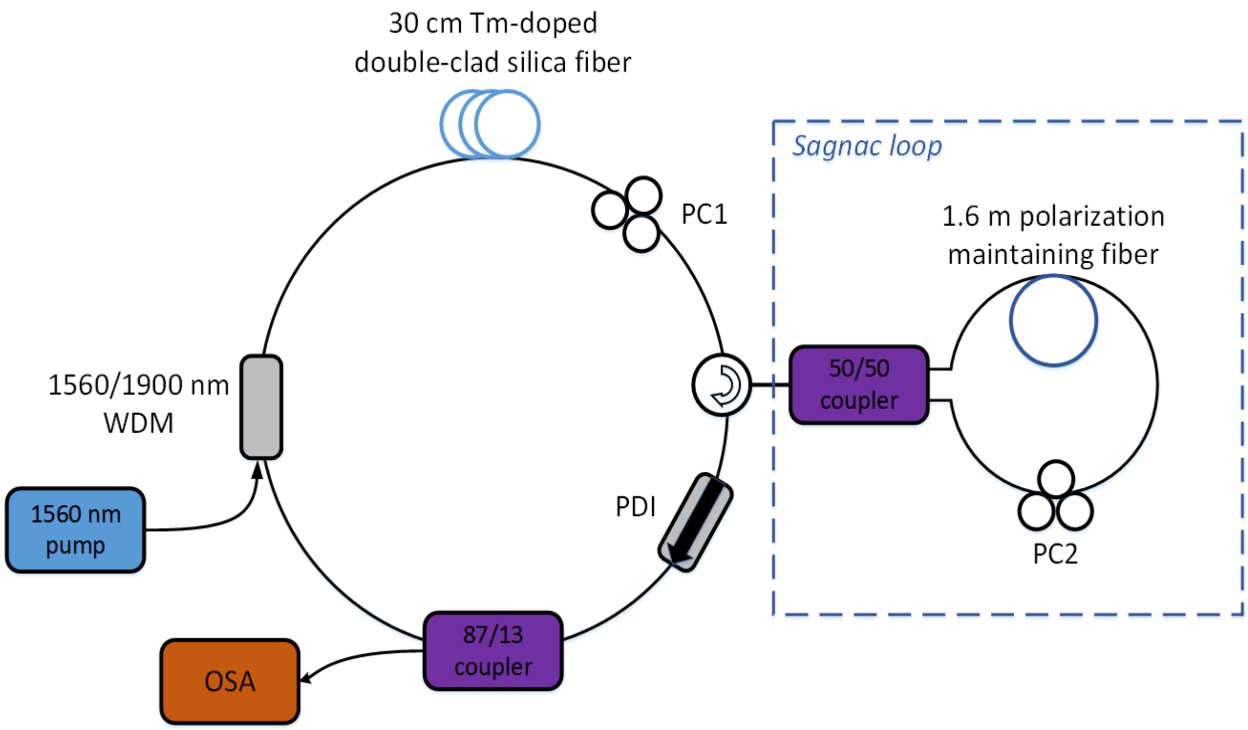

Fig. 3.15 Experimental setup of widely tunable and switchable dual-wavelength TDFL.

Fig. 3.15 shows the schematic of the proposed widely tunable and switchable dual-wavelength TDFL. The 30 cm length of Tm^{3+}:silica DC silica fiber used for the previous measurement is employed as the gain medium. The 1560 nm forward pumping scheme with a maximum output power of 2 W is adopted. The pump is coupled into the Tm^{3+}:silica fiber via a 1560/1900 nm WDM coupler with an insertion loss of ~2.2 dB. Hence, the maximum launched pump power into the gain fiber is ~1.2 W. The first PC (PC1) placed after the gain fiber is employed to adjust the polarization of the lasing signals propagating in the main lasing cavity.

The comb filter is based on a Sagnac loop incorporating a 1.6 m length of PMF, an optical coupler, and the second PC (PC2). The 1.6 m PMF is used to produce a wavelength spacing or free spectral range of ~5.4 nm at 1900 nm. The optical coupler with a splitting ratio of 50:50 at

1900 nm is applied to separate and to recombine the lasing signals. PC2 is used to adjust the reflectivity of the Sagnac loop.

Connected with the gain fiber, the Sagnac loop and a PDI, a polarization independent circulator with a loss of ~0.6 dB ensures the lasing signals to propagate clockwise in the main lasing cavity. The PDI with a loss of ~1 dB is used to suppress mode competition and to provide enhanced stability by its wavelength dependent loss induced by the wavelength dependent polarization rotation mechanism [65, 66]. The PDI can also provide the polarization selectivity for the laser cavity. Note that a single polarization dependent circulator can be used to replace the combination of the polarization independent circulator and the PDI. An optical coupler with a splitting ratio of 87/13 is used to extract the output from the main lasing cavity (13% as the output port). The laser output is measured by an OSA with a resolution of 0.05 nm. The laser cavity length is around ~22 m, while the estimated cavity loss is ~18 dB which mainly results from losses in the Sagnac loop mirror and the 1560/1900 nm WDM coupler.

B. Results and discussion

First, PC2 is optimized to provide a 90° rotation with a peak-to-notch contrast higher than 20 dB, and then the 1560 nm pump power is increased. Single-wavelength lasing is observed at a threshold of 560 mW, while dual-wavelength lasing becomes possible when the pump power is increased further to 580 mW. When the pump power is increased over 700 mW, alternate wavelength switching over a 70 nm range from 1857.95 nm to 1927.25 nm is observed. Such an alternate wavelength switching operation is realized by simply adjusting PC1, while PC2 is unchanged from its initial position. Particularly, we have achieved the following three operations: (a) single-wavelength tuning operation in discrete steps of 5.4 nm; (b) dual-wavelength tuning operation in discrete steps of 5.4 nm; (c) alternate switching operation between single- and dual-wavelength outputs in discrete steps of 5.4 nm over the 70 nm tuning range. The results of the above three operations are summarized in Fig. 3.16. For the whole tuning operations, the signal-to-noise ratios (SNRs) of all lasing wavelengths exceeds 50 dB. If both PC1 and PC2 are adjusted simultaneously, it is possible to shift the fringes of the Sagnac loop mirror and hence to achieve tunable single- and dual-wavelength operation in a continuous manner as in [63, 64]. If the PDI is removed, no stable single- and dual-wavelength tuning operation is observed.

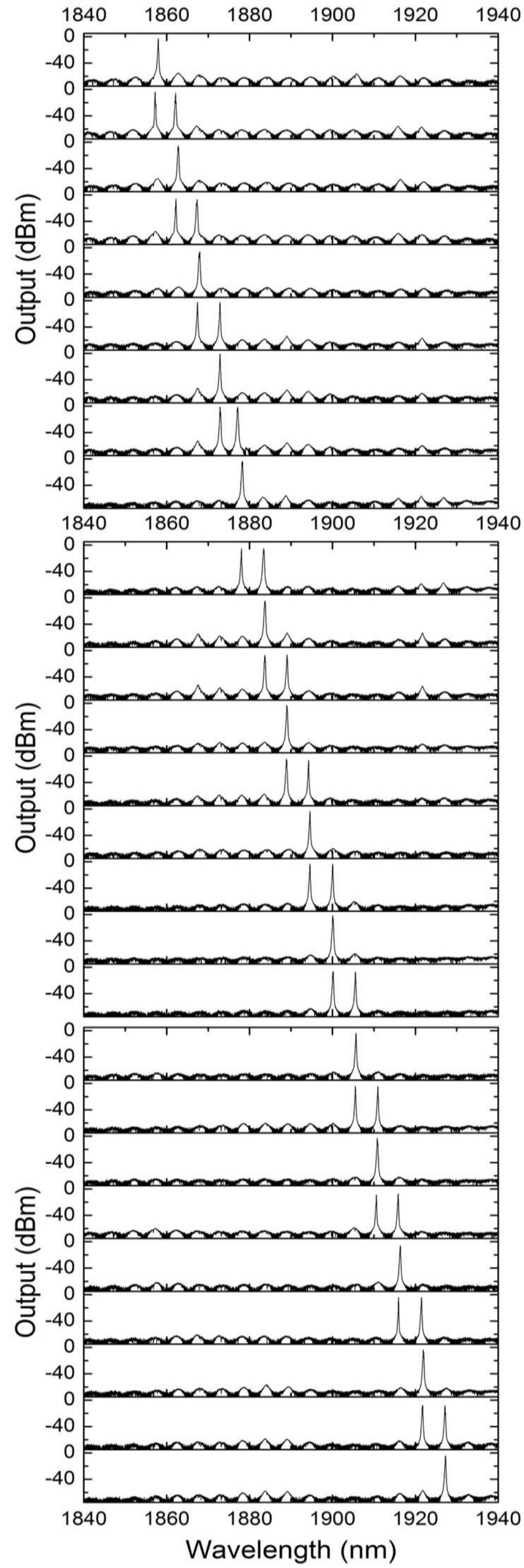

Fig. 3.16 Optical output spectra of dual-wavelength TDFL with tuning and alternate wavelength switching operation from 1857.95 nm to 1927.25 nm.

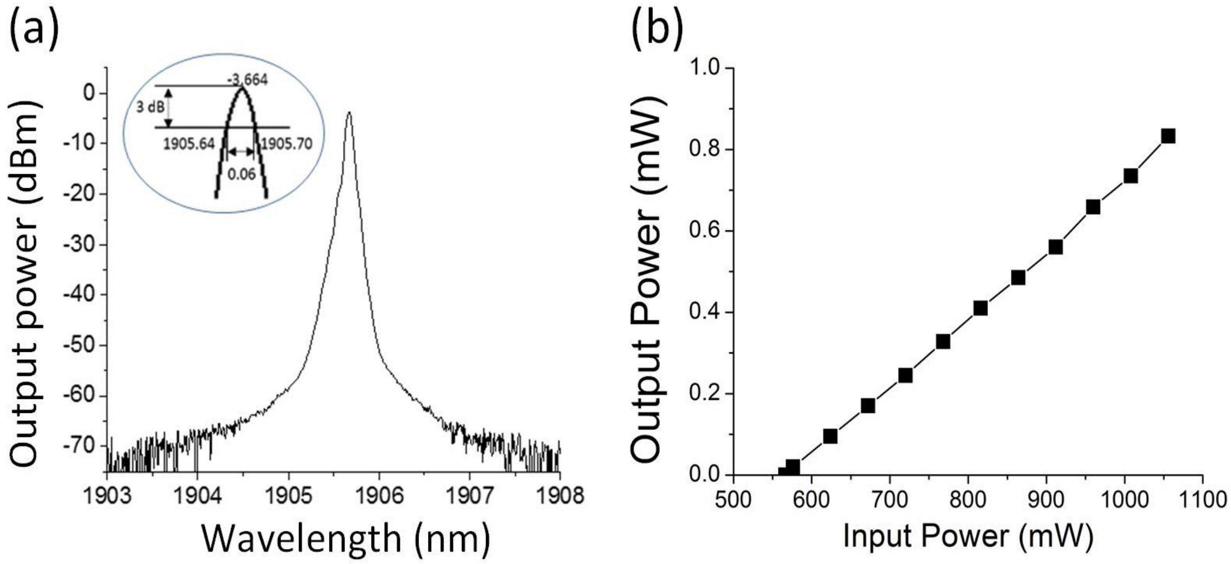

Fig. 3.17 (a) Full width at half maximum of the proposed single-wavelength lasing operation at 1905.6 nm. (b) Measured single-wavelength lasing output power at 1905.6 nm as a function of the 1560 nm pump power.

Fig. 3.17(a) shows the optical output spectrum of the single-wavelength lasing operation at 1905.6 nm. The measured FWHM is smaller than 0.06 nm, which is limited by the resolution bandwidth of the OSA. Due to the relatively long cavity length, the laser is not expected to operate in single longitudinal mode (SLM). To realize the SLM operation, approaches such as incorporating a compound ring cavity into the main cavity [69], using a SA such as a length of unpumped active fiber [70] or graphene [71], employing an equivalent phase-shifted FBG [72], incorporating a semiconductor optical amplifier [73] are required. Fig. 3.17(b) shows the output power as a function of the pump power. Single-wavelength lasing at 1905.6 nm starts at a threshold of 560 mW and increases with a slope efficiency of ~0.2%. Similar characteristics at other wavelengths are observed. Such a low slope efficiency mainly results from the high cavity loss and the strong mode competition. By reducing the component insertion loss and splicing losses, the laser's output efficiency can be further improved. For example, replacing the circulator and PDI with a single polarization dependent circulator can reduce ~1 dB cavity loss, while using a 50:50 coupler instead of a 87:13 coupler can double the output efficiency despite of increasing the lasing threshold. In addition, if a polarizer at 1900 nm is available, linear configuration can be adopted to replace the circulator and the PDI, thus the output efficiency can be greatly improved (>2%).

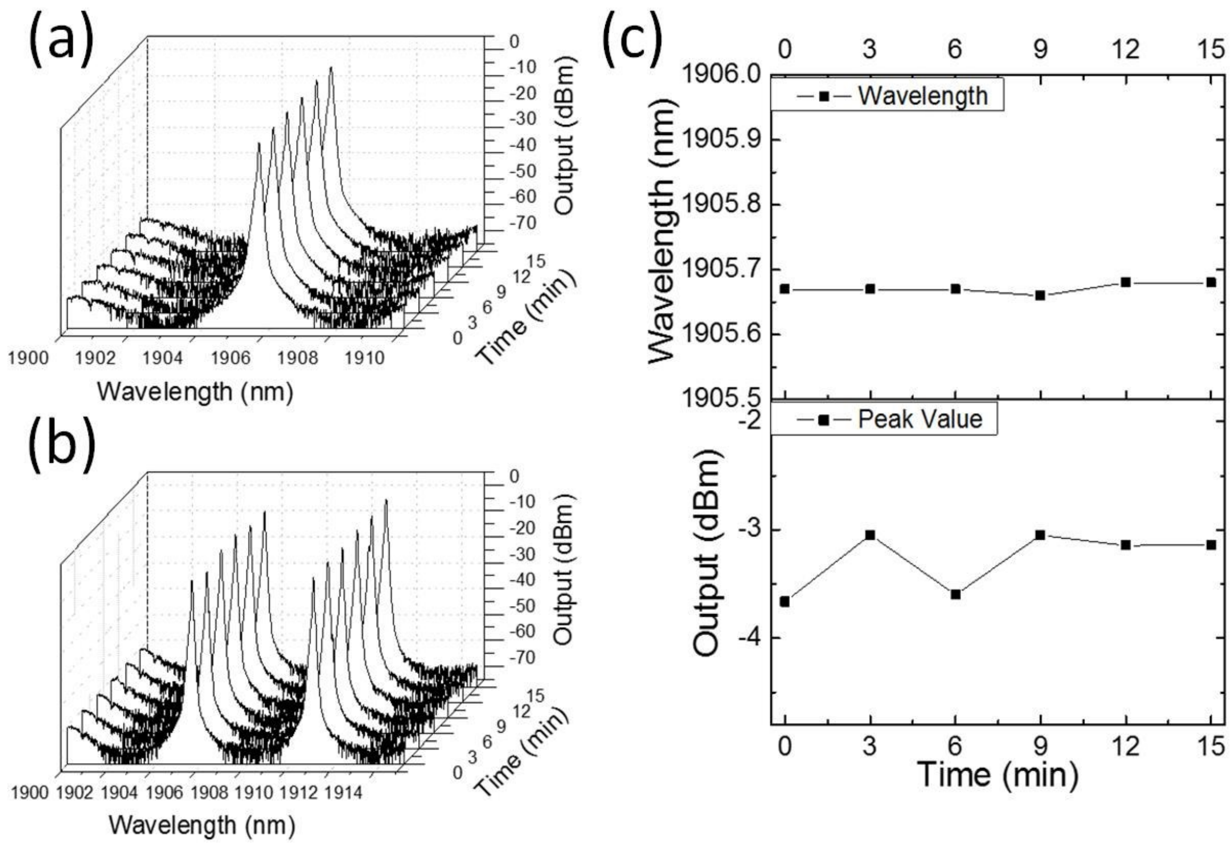

Fig. 3.18 Six repeated optical spectra scans of (a) single-wavelength lasing output at 1905.6 nm and (b) dual-wavelength lasing output at 1905.6 nm and 1911 nm with a span of 15 nm over 15 minutes. (c) Measured lasing center wavelength shifts and output power fluctuations of single-wavelength lasing operation at 1905.6 nm.

The lasing output stability is also of great importance for the dual-wavelength TDFL. Fig. 3.18(a) and (b) show the repeated six scans (recorded every 180 seconds) of the laser output spectra for single-wavelength operation at 1905.6 nm and dual-wavelength operation at 1905.6 nm and 1911 nm, respectively. For the single-wavelength lasing operation at 1905.6 nm, its center wavelength variations are less than 0.02 nm, while its output power fluctuations are less than 0.7 dB in 15 minutes, as shown in Fig. 3.18(c). Although these measurements do not show continuous fast variations, they provide a reasonable indication of the long term stability of the dual-wavelength TDFL.

C. Summary

We have demonstrated a widely tunable and switchable dual-wavelength TDFL based on the Sagnac loop mirror and Tm^{3+}:silica DC silica fiber, with a tuning range over 70 nm from 1857 nm to 1927 nm. Only by simply controlling the PC in the ring cavity, alternate/sequential switching operation is realized with ~5.4 nm wavelength spacing. The output of each lasing operation has an SNR larger than 50 dB, while its FWHM is smaller than 0.06 nm. The center wavelength variation is less than 0.02 nm, while output power fluctuations are less than 0.7 dB during 15 minutes, which show good stability. We believe that such a laser can offer capabilities in the fields of fiber optic sensing in the 1900 nm wavelength range, such as LIDAR [74], multi-wavelength absorption spectroscopy [24] and fiber cavity ring-down spectroscopy [75].

3.4 Conclusion

In this chapter, we have demonstrated the use of Tm^{3+}:ZBLAN fiber to realize a dual-band CW Tm^{3+}:ZBLAN fiber laser at 810 nm and 1487 nm and a three-wavelength Tm^{3+}:ZBLAN fiber laser emitting simultaneously at 1460 nm, 1503 nm and 1873 nm, and the use of Tm^{3+}:silica fiber to achieve a widely tunable and switchable dual-wavelength TDFL with a 70 nm tuning range. These CW dual-band fiber laser sources will be attractive in the fields of spectroscopy, instrumentation, and communications.

We have demonstrated a dual-band CW Tm^{3+}:ZBLAN fiber laser at 810 nm and 1487 nm using upconversion pumping at 1064 nm. This dual-band fiber laser shares the same upper energy level $^3H_4$, and supports two different electron transitions, the $^3H_4 \rightarrow {}^3H_6$ transition at 810 nm and the $^3H_4 \rightarrow {}^3F_4$ transition at 1487 nm, simultaneously. Output powers at both wavelengths can exceed 25 mW. By controlling the 1064 nm pump power, single-wavelength operation at 810 nm or 1487 nm, and dual-wavelength operation at both wavelengths are achieved.

We have also demonstrated a three-wavelength Tm^{3+}:ZBLAN fiber laser emitting simultaneously at 1460 nm, 1503 nm and 1873 nm. The 1064 nm pump source is used for lasing operation at 1460 nm and 1503 nm in one branch, while the 1560 nm pump source is used for lasing operation at 1873 nm in the other branch. A shared branch serves as the output coupler for these three lasing wavelengths. The power fluctuations at three wavelengths are all less than 1.5 dB over 30 minutes. Also switchable dual-wavelength operation at 1460 nm and 1503 nm is obtained by controlling the PC.

We have used the Tm^{3+}:silica DC fiber to develop a widely tunable and switchable dual-wavelength TDFL based on Sagnac loop mirror with a tuning range over 70 nm from 1857 nm to 1927 nm. Alternate switching operation is realized with ~5.4 nm wavelength spacing by controlling the rotation of PC. The output of each lasing operation has an SNR larger than 50 dB, and an FWHM smaller than 0.06 nm. The TDFL shows good stability, as its center wavelength variation is less than 0.02 nm and its output power fluctuations are less than 0.7 dB during 15 minutes.

Chapter 4

Pulsed Tm^{3+}:ZBLAN fiber lasers based on a graphene SA

4.1 Introduction

Different from CW operation, pulsed lasers emit light in the form of optical pulses with certain repetition rates and higher peak powers. Q-switching and mode-locking are the two main methods enabling pulse generation [18].

Q-switching is a modulation process of the quality factor Q, which is the ratio between the energy stored and that lost in the gain medium per oscillation cycle. In Q-switching process, lasing is initially prevented with high losses by a low Q factor, and the pump energy is stored and accumulated in the gain medium. When the stored energy reaches some maximum level, the gain medium is gain saturated. At this point, lasing is allowed with low losses by a high Q factor, and the stored energy in the gain medium is released in a high intensity pulse with typical durations ranging from μs to ns. Q-switching has distinctive advantages such as low cost, efficient operation, and easy implementation. Q-switched fiber lasers are important in metal cutting, environmental sensing, pulsed holography, range finding and long-pulse nonlinear experiments, which require high laser intensities in nanosecond pulses [76-78].

On the other hand, mode-locking is a technique to obtain ultrashort pulses from lasers. The laser cavity contains either a nonlinear passive element (a SA) or an active element (an optical modulator), which leads to the formation of ultrashort pulses circulating in the laser cavity. By balancing the intra-cavity dispersion and nonlinearity, as well as inducing a fixed-phase, a single pulse is produced with typical duration ranging from ps down to fs, and a repetition rate corresponding to the cavity round-trip time. The pulse peak power of mode-locked fiber lasers can be several orders of magnitude higher than the average optical output power. These femtosecond ultrafast mode-locked pulses have widespread applications in the fields of tele-communications, instrumentation and spectroscopy.

Compared with active pulse generation, passively pulsed (Q-switched and mode locked) fiber lasers based on a SA provide the advantages of low cost, simplicity and compactness. Recently, graphene has emerged as an innovative and promising material as a SA for passively Q-switched and mode-locked fiber lasers to facilitate pulse generation [20, 79]. Its unique electrical and optical properties, such as ultra-broadband operation, fast response time and ease of fabrication, make it as a suitable SA to be integrated in fiber laser for passive pulse generation. Compared with other pulse generation SAs (doped bulk crystals, semiconductor SA mirrors, single wall carbon nanotubes, etc.), graphene has distinctive advantages such as low saturation intensity, ultra-broadband operating wavelength range and high optical damage threshold [20]. In the ZBLAN host, it has been successfully applied on Q-switched laser at 1.19 μm and 3 μm by Ho^{3+}-doped ZBLAN fiber [80, 81] and at 2.78 μm by Er^{3+}-doped ZBLAN fiber [82], as well as on mode-locked laser at 2.8 μm by Er^{3+}-doped ZBLAN fiber [83].

Fiber lasers operating simultaneously in two different wavelength bands can provide enhanced functionality and new capabilities in sensing, communications and instrumentation. A number of dual-band laser sources (CW and pulsed) have been demonstrated on fiber lasers [24], semiconductors (e.g. VCSEL, [84]) and parametric oscillators [47]. Especially dual band pulsed laser sources have been applied in the fields of nonlinear frequency conversion [46], multi-color pump-probe processes [47] and Raman scattering spectroscopy [48]. In particular, the passive dual-band pulsed fiber laser based on a common SA has attracted considerable attention due to its unique properties such as compactness, environmental invulnerability and flexibility. Previously, Wu *et al*. [85] presented passive synchronization of Q-switched fiber lasers at 1.06 μm with Yb-doped silica fiber and 1.53 μm with Er:Yb-codoped silica fiber by sharing a common graphene SA. Zhang *et al*. [86] reported passive synchronization of mode-locked fiber lasers at 1.06 μm with Yb-doped silica fiber and 1.54 μm with Er-doped silica fiber by sharing a common single-wall carbon nanotube SA. Sotor *et al*. [87, 88] demonstrated dual-band mode-locked fiber lasers (with and without synchronization) operating simultaneously at 1.56 μm with Er-doped silica fiber and 1.94 μm with Tm-doped fiber by sharing a common graphene SA. However, all of these demonstrations used two separate gain media with increased complexity in laser design and implementation.

In this chapter, we combine the use of a single gain medium – Tm^{3+}:ZBLAN fiber, and a common graphene SA to achieve ultrabroad dual-band pulsed operation. We demonstrate for the first time the use of Tm^{3+}:ZBLAN fiber to obtain (1) a passively synchronized Q-switched dual-band fiber ring laser at 1480 nm and 1840 nm with a synchronized repetition rate from 20 kHz to 40.5 kHz, and (2) a mode-locked dual-band fiber linear laser at 1480 nm and 1845 nm with synchronized or unsynchronized mode-locked pulses.

4.2 Passively synchronized dual-band Q-switched Tm^{3+}:ZBLAN fiber laser at 1480 nm and 1840 nm based on a graphene SA

A. Experimental setup

Fig. 4.1 shows the schematic of the passively synchronized Q-switched dual-band Tm^{3+}:ZBLAN fiber ring laser at 1480 nm and 1840 nm. It consists of two ring cavities along with one common branch incorporating the graphene SA. In the top 1480 nm loop, an 80 cm length of Tm^{3+}:ZBLAN fiber is pumped by a 1064 nm Yb-doped fiber laser (P_{1064}) via a 1064/1480 nm WDM coupler. A 1480 nm polarization independent isolator (PI-ISO) is employed to keep the 1480 nm signal propagating clockwise. In the bottom 1840 nm loop, a 35 cm length of Tm^{3+}:ZBLAN fiber is pumped by a 1560 nm Er-doped amplified fiber laser (P_{1560}) via a 1560/1840 nm WDM coupler. An 1840 nm PI-ISO is employed to keep the 1840 nm signal propagating counter-clockwise. The Tm^{3+}:ZBLAN gain fiber, which is the same as that used in the previous chapter, is coupled with SMF-28 fiber based devices through mechanical splices, inducing ~2 dB loss per pair. Two PCs optimized at each wavelength are used to adjust intra-cavity polarization state and to optimize the laser output in each cavity, respectively. Two optical couplers with a splitting ratio of 90:10 at each wavelength are used to extract the 10% outputs from the two ring cavities, respectively. Two 1480/1840 nm WDM couplers are employed to combine and separate back both signals. The graphene film is deposited and sandwiched between two FC/APC fiber pigtails to form the SA [79]. The preparation of the graphene film uses a similar process to that in

[89]. Characterization of the samples show that they comprise ~ 6 layers of graphene; moreover, the modulation depth is 40% - 50% and the saturation intensity is ~ 0.7 MW/cm^2 at 1550 nm. The total 1480 nm loop cavity length is ~12 m with an estimated cavity loss of 13.5 dB, while the total 1840 nm loop cavity length is ~13.5 m with an estimated cavity loss of 14.2 dB.

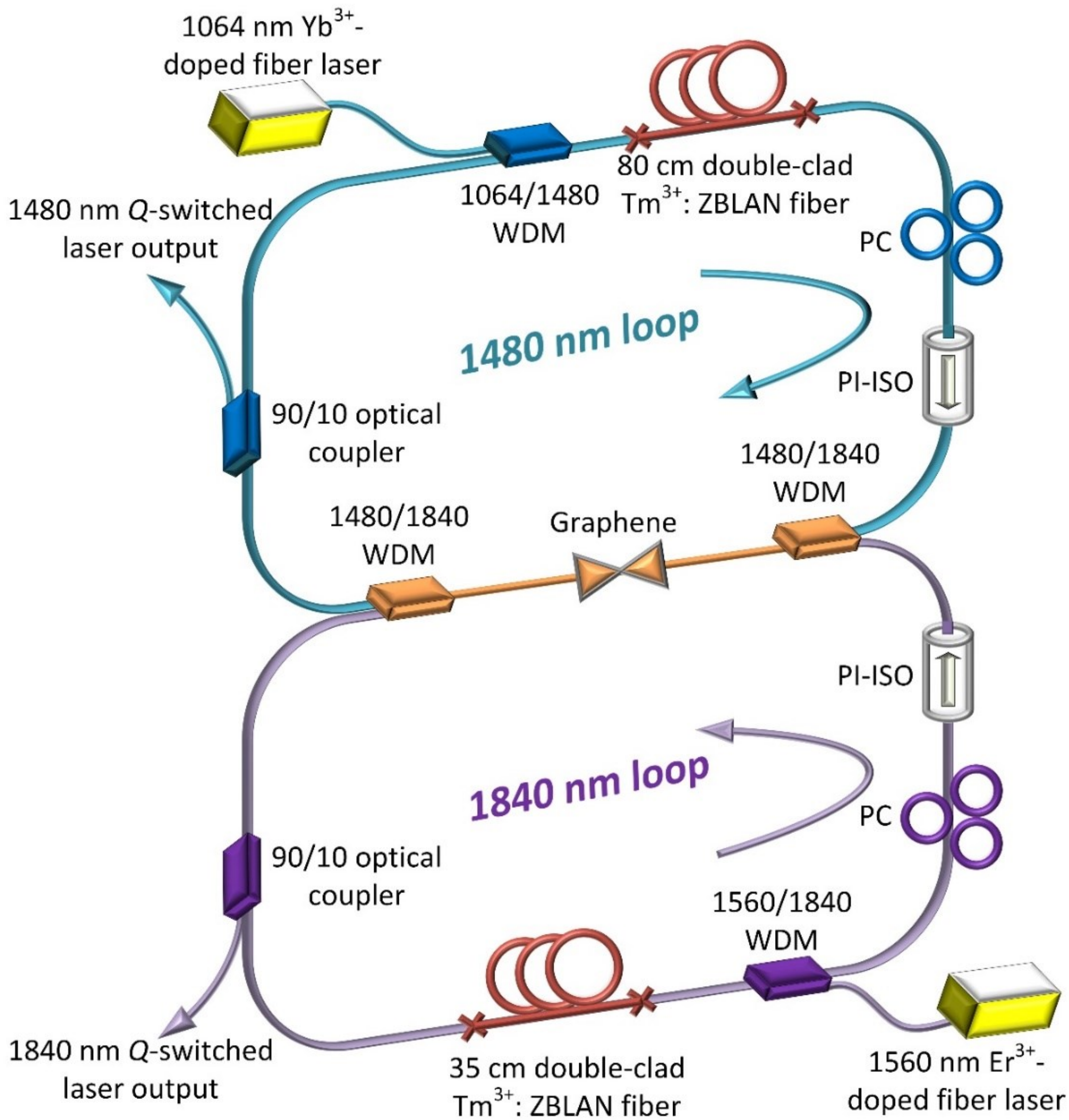

Fig. 4.1 Experimental setup of passively synchronized Q-switched dual-band Tm^{3+}:ZBLAN fiber laser.

For the dual-band Q-switched operation, the laser output is measured (1) directly at the output from the 1480 nm or 1840 nm cavity in order to characterize either cavity operating independently; and (2) after a 1480/1840 nm WDM coupler combining two individual outputs from the two cavities in order to observe the dual-band output when both cavities are active. The optical output powers are measured by a power meter (Thorlabs, PM100D) along with a thermal power sensor (Thorlabs, S302C). Note that all the pump powers are measured after WDM couplers. The optical spectrum is measured by an OSA (YOKOGAWA, AQ6375). The pulse trains in the time domain are measured by a combination of a 7.5 GHz photodetector (Newport, 818-BB-51F) and a 60 MHz oscilloscope (Agilent, 54621A), while the RF spectra is monitored by a combination of the 7.5 GHz photodetector and an electrical spectrum analyzer (ESA, Anritsu, MS2668C) with a frequency range from 9 kHz to 40 GHz.

B. Results and discussion

Fig. 4.2 shows the characteristics, including the repetition rate, pulse width, average output power and calculated pulse energy, of each loop operating when the other loop is either on or off. We first characterize the 1480 nm loop when the 1840 nm loop is turned off (P_{1560}=0 mW). CW lasing operation at 1480 nm starts when P_{1064} exceeds a threshold of ~526 mW. When P_{1064} is increased to ~538 mW, Q-switched pulses are observed with an initial repetition rate of 16 kHz. As P_{1064} is increased further up to ~682 mW, stable Q-switched operation is maintained with a repetition rate ranging from 16 kHz to 47.5 kHz at a rate of 219 Hz/mW, a typical signature of Q-switching operation. Meanwhile, the corresponding pulse duration first decreases exponentially from ~14 µs to ~4.2 µs, and then keep a constant level of ~4.2 µs, indicating the graphene SA is almost saturated. The corresponding average output power increases linearly up to ~792 µW with 0.48% slope efficiency. Such a low slope efficiency mainly results from the relatively high cavity loss including the WDM coupling loss, splicing loss between Tm^{3+}:ZBLAN fiber and SMF-28 fiber, and the graphene transmission loss. The corresponding pulse energy increases linearly and then keep at a saturated level of ~16 nJ, further demonstrating the saturation of the graphene SA. When P_{1064} is 682 mW, Q-switched output pulses have a repetition rate of 47.5 kHz, an average output power of 0.78 mW, a pulse energy of 16.47 nJ, and a peak power of 3.77 mW. When P_{1064} is above 682 mW, no stable Q-switching or other pulse operation is observed.

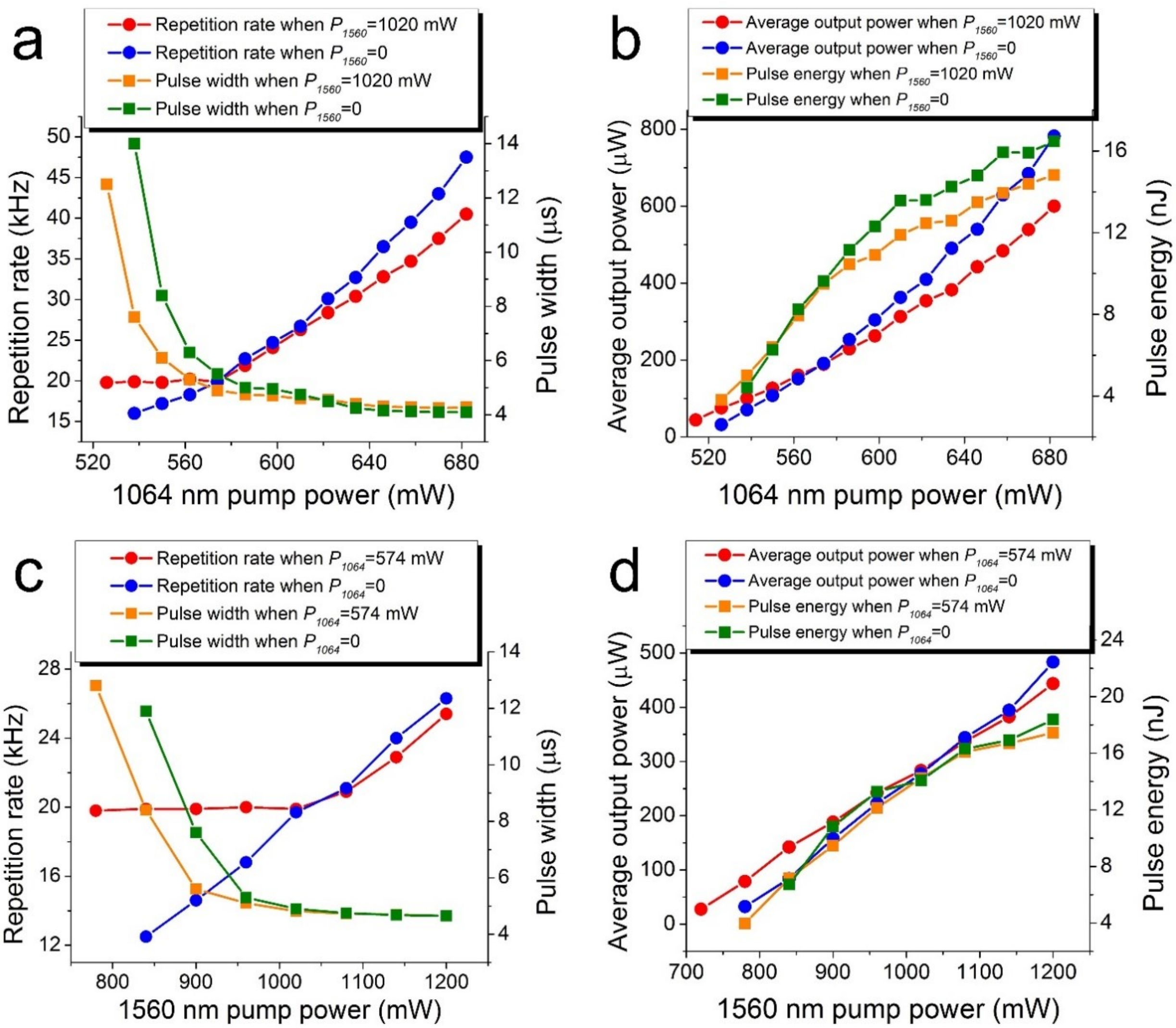

Fig. 4.2 Characteristics of the passively synchronized dual-band Q-switched Tm^{3+}:ZBLAN fiber laser. (a) Repetition rate and pulse width and (b) average output power and calculated pulse energy of the Q-switched pulses at 1480 nm when the 1560 nm pump power is 0 and 1020 mW; (c) repetition rate and pulse width and (d) average output power and calculated pulse energy of the Q-switched pulses at 1840 nm when the 1064 nm pump power is 0 and 574 mW.

In our experiment, these two cavities do not work independently. Q-switched pulse synchronization is observed when both loops operate together. In particular, the cavity with a higher repetition rate dominates the other cavity. As an example, we preset the 1560 nm pump power as 1020 mW so that the 1840 nm loop produces Q-switching pulses at 20 kHz, and then re-characterize the 1480 nm loop. CW lasing operation at 1480 nm occurs at a threshold P_{1064} of 502 mW, lower than the threshold when the 1480 nm loop operate alone, owing to the transmission loss change of the graphene SA. As P_{1064} is increased from 526 mW to 574 mW, Q-switched pulses at 1480 nm keep a fixed repetition rate of 20 kHz (as opposed to the increasing rate when P_{1560}=0 mW) with pulse durations decreasing from 12.5 μs to 4.9 μs, as shown by the red dots and orange squares in Fig. 4.2(a). Meanwhile, the 1840 nm cavity also produces Q-switched pulses with the same repetition rate of 20 kHz. As P_{1064} is increased from 574 mW to 682 mW, the repetition rates of the two cavities both simultaneously increase from 20 kHz to 40.5 kHz, indicating that the repetition rate of the 1480 nm cavity dominates that of the 1840 nm cavity (as opposed to being fixed at 20 kHz when P_{1064}=0 mW).

We observe similar operation characteristics in the 1840 nm loop. For example, we first preset the 1064 nm pump power as 0 mW and characterize the 1840 nm loop. CW lasing operation occurs at a threshold P_{1560} of 720 mW. As P_{1560} is varied from 780 mW to 1200 mW, stable Q-switched pulses are then established with a repetition rate from 12.5 kHz to 26.3 kHz. The corresponding pulse energy and peak power can reach up to 18.38 nJ and 3.71 mW, respectively. Second, we preset the 1064 nm pump power as 574 mW to produce 20-kHz Q-switched pulses at 1480 nm, and then re-characterize the 1840 nm loop. As P_{1560} is increased from 780 mW to 1020 mW, synchronized Q-switched pulses at 1480 nm and 1840 nm are both observed with a fixed repetition rate of 20 kHz. As P_{1560} is increased from 780 mW further up to 1200 mW, the repetition rates of Q-switched pulses at 1480 nm and 1840 nm both increase simultaneously from 20 kHz to 25.8 kHz.

These passive pulse synchronization is attributed to the graphene's saturable absorption effect. When the Q-switched pulses at these two wavelengths are non-overlapping temporally, both loops operate independently with individual repetition rates controlled by their respective pump powers, mainly due to the ultrafast response and broadband operation of graphene. On the contrary, when the Q-switched pulses at these two wavelengths are overlapped temporally, the combined intensity through the common graphene SA is higher compared with one wavelength operating along, resulting in the changes of balance between gain and loss from graphene. Hence, passive pulse synchronization occurs. These dual-band Q-switched outputs are sensitive with the intra-cavity polarization state of each loop. By simply adjusting the PCs in each loop, the central lasing lines can be shifted by ~5 nm, while the corresponding average output powers, pulse durations as well as the repetition rates can be changed by ~20% under the same pump power. For the dual-band Q-switched outputs, the pulse durations and peak powers can be optimized by using a higher dopant gain fiber, shortening the cavity length and losses, along with optimizing the graphene SA by evanescent field interaction [90].

Fig. 4.3 shows the output spectra from the dual-band laser. Black curve shows the combined output when it operates in synchronized Q-switched mode with P_{1064}=574 mW and P_{1560}=1020 mW. Blue and red curves show separate outputs when one loop operates alone, respectively. Note there is no residual output from the inactive cavity.

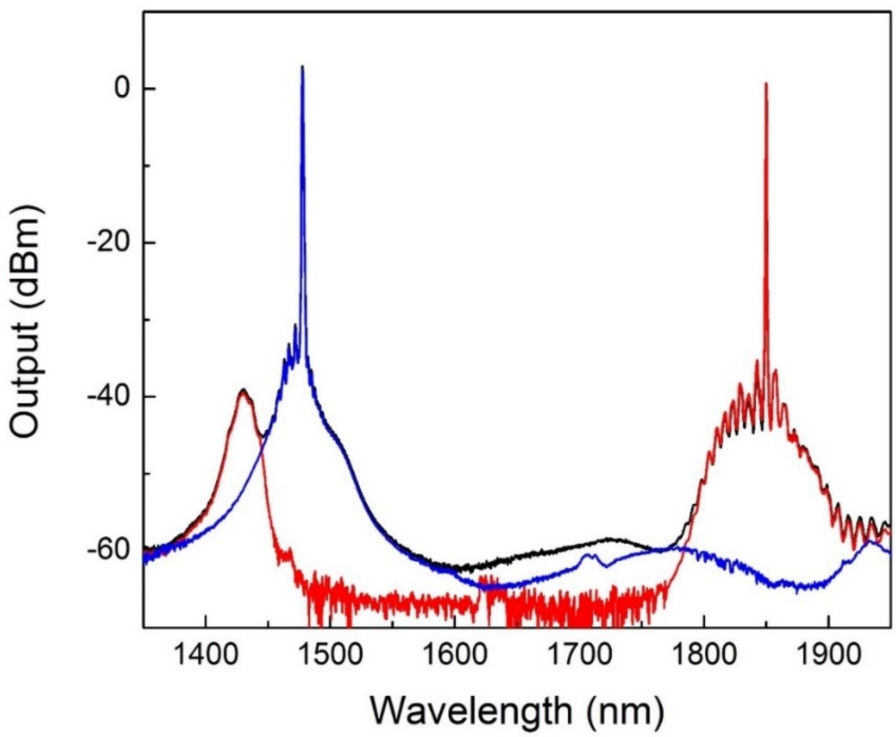

Fig. 4.3 Optical output spectra from the passively synchronized dual-band Q-switched Tm^{3+}:ZBLAN fiber laser. Simultaneous output at 1480 nm and 1840 nm when both cavities operate (P_{1064}= 574 mW, P_{1560}=1020 mW, black curve), output at 1480 nm only when the 1840 nm cavity is off (P_{1064}= 574 mW, P_{1560}=0 mW, blue curve), and output at 1840 nm only when the 1480 nm cavity is off (P_{1064}= 0 mW, P_{1560}=1020 mW, red curve)

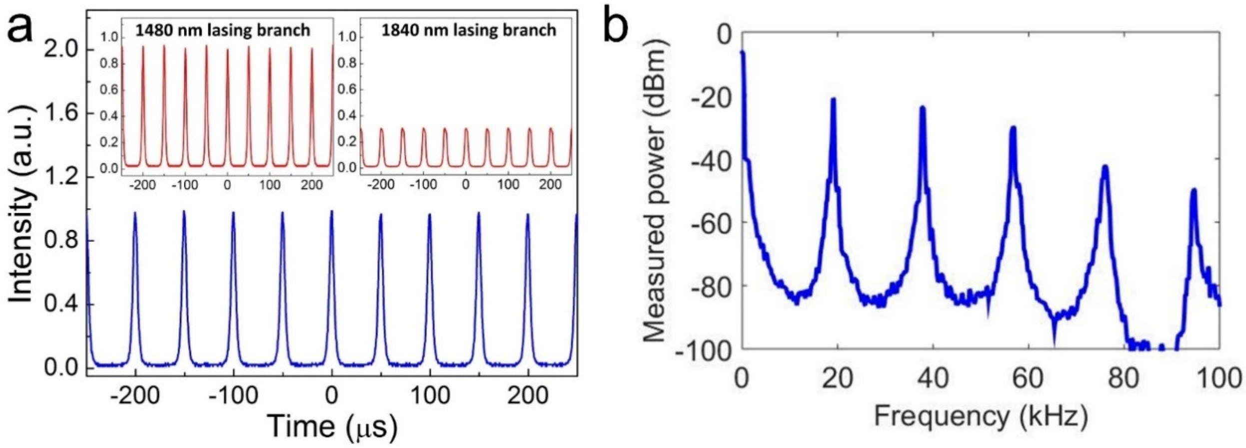

Fig. 4.4 (a) Combined Q-switched pulse trains in the time domain and (b) corresponding RF spectrum of the passively synchronized dual-band Q-switched Tm^{3+}:ZBLAN fiber laser when P_{1064}=574 mW and P_{1560}=840 mW. The insets in (a) show Q-switched pulses at these two wavelengths before they are combined by the optical coupler

Fig. 4.4 shows the temporal pulse trains and the corresponding RF spectrum after two Q-switched outputs are combined by the optical coupler. For example, when P_{1064}= 574 mW and P_{1560}=840 mW, the combined pulse trains coincide with the two individual pulse trains as shown in insets, further confirming that Q-switched pulses at the two wavelengths are completely synchronized. No amplification modulation in the pulses at the two wavelengths is observed, demonstrating the absence of self-mode-locking effects in Q-switching operation. The RF spectrum of the dual-band Q-switched operation shows a repetition rate of ~20 kHz with an RF SNR exceeding 60 dB, further indicating the stable nature of the synchronized Q-switched operation. Similar RF spectra at 1480 nm and 1840 nm are observed before the two Q-switched outputs are combined.

C. Summary

We have demonstrated a passively synchronized dual-band Q-switched Tm^{3+}:ZBLAN fiber laser at 1480 nm and 1840 nm. Based on a common graphene SA, dual-band Q-switched operation with synchronized repetition rate from 20 kHz to 40.5 kHz is achieved. Such ultra-broadband synchronized Q-switched pulses will find important applications in the fields of nonlinear frequency conversion, spectroscopy and chemical sensing.

4.3 Simultaneous mode locked Tm^{3+}:ZBLAN fiber laser at 1480 nm and 1845 nm based on a graphene SA

A. Experimental setup

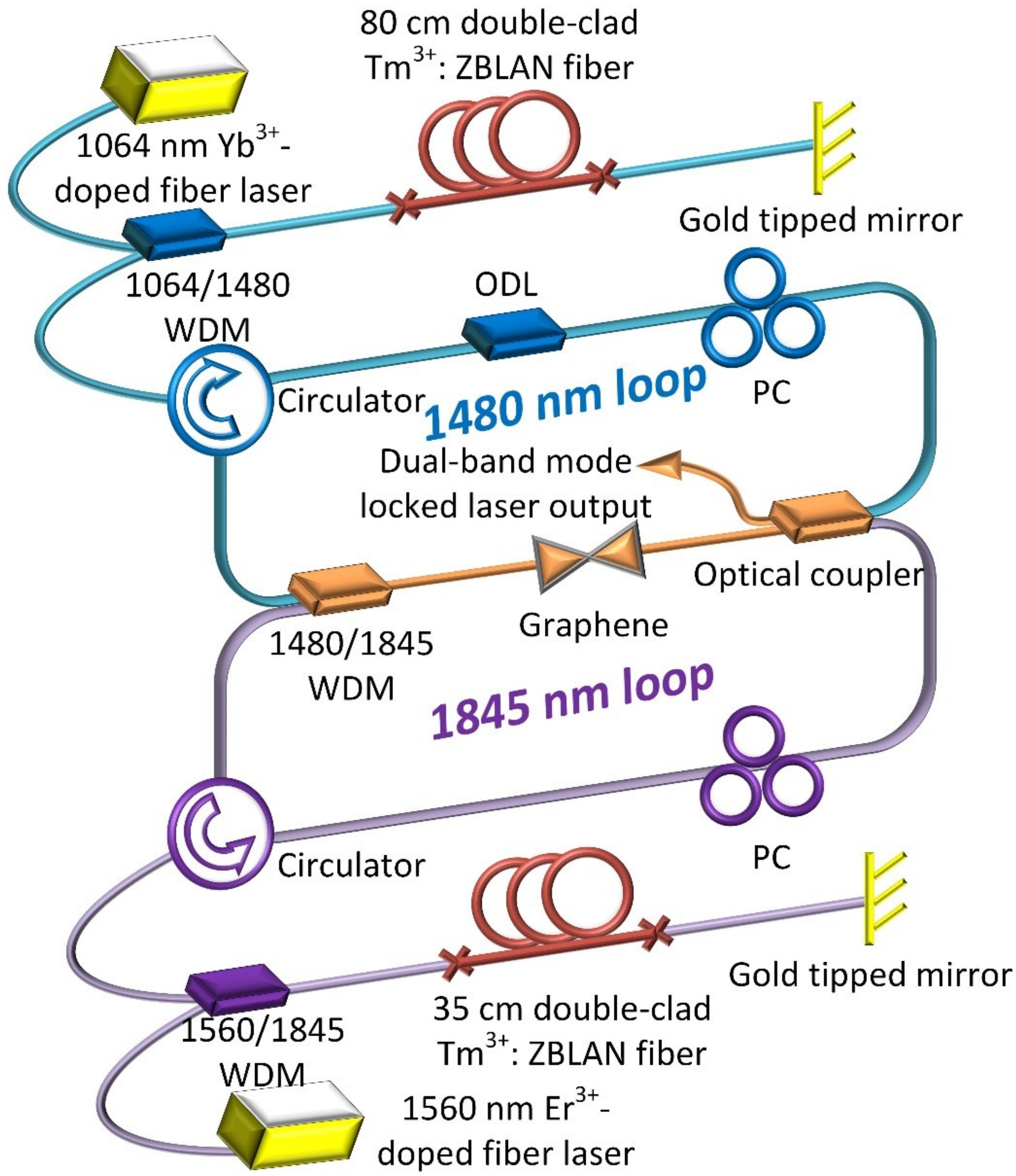

Fig. 4.5 Experimental setup of simultaneous mode-locked dual-band Tm^{3+}:ZBLAN fiber laser at 1480 nm and 1845 nm.

In order to improve the lasing output efficiency and to initial the dual-band simultaneous mode-locking operation, two linear cavities with shorter cavity lengths along with one shared branch is adopted, as shown in Fig. 4.5. This laser consists of two independent linear cavities, which generate lasing at 1480 nm and 1845 nm, respectively, as well as one common branch including the graphene SA and one output coupler. The same gain fibers used for the previous synchronized Q-switched dual-band Tm^{3+}:ZBLAN fiber laser are used again for the 1480 nm and 1845 nm cavities, respectively.

In the top 1480 nm branch, the 80 cm Tm^{3+}:ZBLAN fiber is pumped by a 1064 nm YDFL (P_{1064}) via a 1064/1480 nm WDM coupler. In the bottom 1845 nm branch, the 35 cm Tm^{3+}:ZBLAN fiber is pumped by a 1560 nm EDFL(P_{1560}) via a 1560/1845 nm WDM coupler. Two gold-tipped fiber mirrors serve as two reflectors to form one end of each cavity, respectively. Two circulators optimized at 1480 nm and 1845 nm are used to keep light unidirectional propagation and to allow the light to oscillate in each linear cavity, respectively. Two PCs are used to adjust the intra-cavity polarization and to initiate the mode-locking. Varying lengths of single mode fiber and an optical delay line (ODL) are added into the 1480 nm loop for the cavity length tuning in order to obtain synchronized or unsynchronized mode-locking operation.

The common branch consists of one optical coupler, the graphene SA, along with one 1480/1845 WDM coupler. The optical coupler with a splitting ratio of 50:50 at 1480 nm and 90:10 at 1845 nm is used to combine the 1480 nm and 1845 nm signals and to couple out the light (10% as the output port). The 1480/1845 WDM coupler separates the 1480 nm and 1845 nm signals back to their respective cavities. The total cavity lengths of the 1480 nm branch and 1845 nm branch is ~13.4 m and ~19.1 m, respectively.

The simultaneous mode-locked dual-band laser's outputs in the optical domain and in the time domain are measured with the same devices as used for the synchronized Q-switched dual-band laser in Section 4.2. The pulse widths at 1480 nm and 1845 nm are characterized using two different autocorrelators, FR-103XL for 1480 nm and FR-103HS for 1845 nm, both manufactured by Femtochrome Research Inc..

B. Unsynchronized results and discussion

We first tune the cavity lengths at 1480 nm and 1845 nm as ~16.3 m and ~17.2 m, respectively. Unsynchronized simultaneous mode-locked dual-band operation is observed as follows.

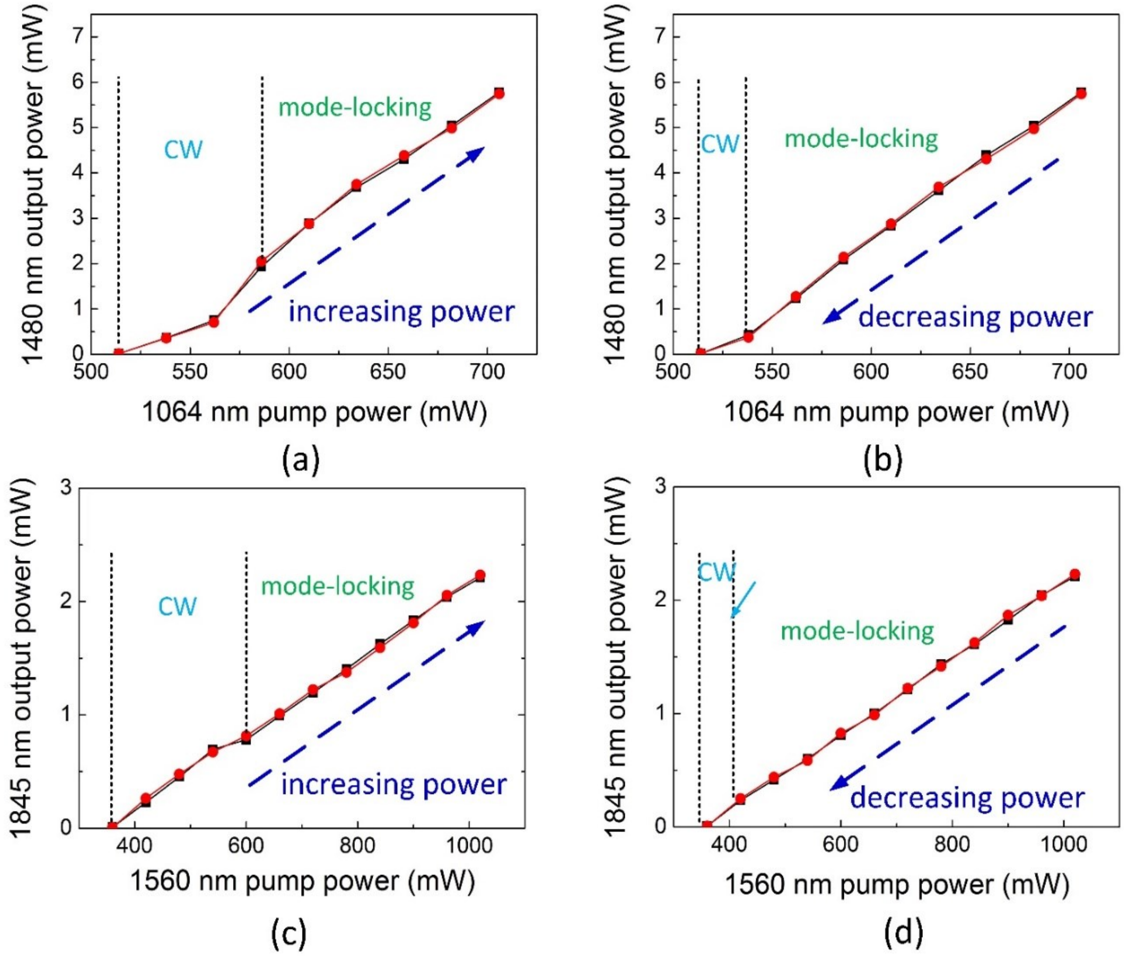

Fig. 4.6 Characteristics of the unsynchronized mode-locked dual-band Tm^{3+}:ZBLAN fiber laser. Measured output power at 1480 nm when the 1845 nm cavity is on (P_{1560}=900 mW, black curve) and off (P_{1560}=0 mW, red curve) as P_{1064} increases (a) and decreases (b). Measured output power at 1845 nm when the 1480 nm cavity is on (P_{1064}=682 mW, black curve) and off (P_{1064}=0 mW, red curve) as P_{1560} increases (c) and decreases (d).

In our experiment, similar characteristics in terms of output power as a function of pump power and independent operation of the two cavities are observed for the unsynchronized dual-band mode-locking operation. Fig. 4.6 shows the laser output power at 1480 nm and 1845 nm along with the corresponding lasing operation regimes as a function of 1064 nm and 1560 nm pump power[(a, c) show increasing pump power, while (b, d) show decreasing pump power], respectively.

CW lasing at 1480 nm occurs at a threshold P_{1064} of 514 mW. When the 1064 nm pump power is increased to 586 mW, the laser's output power at 1480 nm increases significantly and its corresponding optical spectrum is broadened by carefully adjusting the PC. As the 1064 nm pump power increases from 586 mW up to 706 mW, stable fundamental mode-locking operation at 1480 nm is observed and maintained. In order to protect the graphene SA, the 1064 nm pump power is controlled below 710 mW. When the 1064 nm pump power is decreased from 706 mW down to 538 mW, stable mode-locking pulses are maintained. When the 1064 nm pump power is further decreased from 538 mW, CW lasing operation at 1480 nm reappears without optical spectrum broadening until the lasing threshold of 514 mW. In general, the 1480 nm cavity of unsynchronized mode-locking operation has the same evaluation of optical output power as that of synchronized mode-locking operation,

Similar characteristics are observed in the 1845 nm loop. CW lasing at 1845 nm starts at a threshold P_{1560} of 360 mW, and stable fundamental mode-locking operation at 1845 nm initiates at 600 mW and maintains until 1020 mW. As the 1560 nm pump power decreases from 1020 mW, mode-locking operation is maintained until the 1560 nm pump power reaches 420 mW. CW lasing re-appears as the 1560 nm pump power decreases from 420 mW to 360 mW.

To demonstrate these two cavities operating independently, we re-measure the output powers at 1480 nm and 1845 nm when the other cavity is set to operate in the mode-locking regime, respectively, as shown in the black squares of Fig. 4.6. The same evolution of output powers and lasing operating regimes are obtained whether or not the other cavity is active, indicating these two lasing cavities operate independently when the dual-band Tm^{3+}:ZBLAN fiber laser is tuned for unsynchronized mode-locking operation.

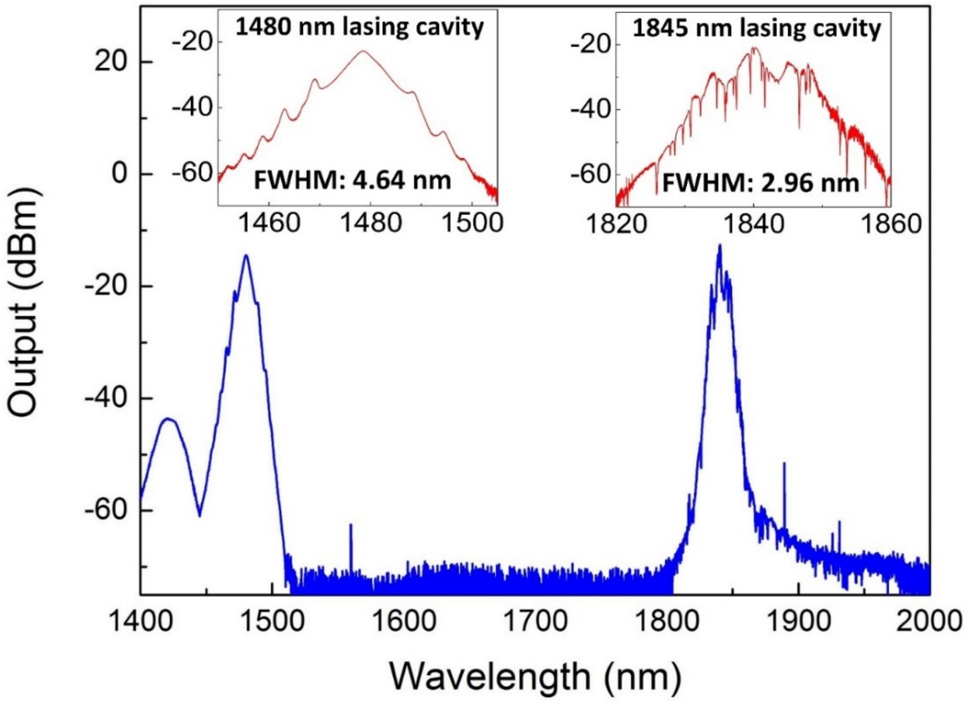

Fig. 4.7 Optical output spectra of the unsynchronized mode-locked dual-band Tm^{3+}:ZBLAN fiber laser when both cavities operate (P_{1064}= 682 mW, P_{1560}=900 mW). The insets show the optical output spectra at the two wavelength within a 50-nm span.

Fig. 4.7 shows the typical optical spectrum of unsynchronized mode-locked dual-band laser, demonstrating the ultra-broadband mode-locking operation at 1480 nm and 1845 nm simultaneously. The insets show the optical spectra within a 50 nm span centered at each lasing wavelength with a 0.05 nm resolution. The net dispersions of both cavities are anomalous, indicating the two cavities generate soliton-like pulses, which are also confirmed by the typical Kelly sidebands, a periodic disturbance of soliton pulses in the laser resonator. The Kelly sidebands in the optical spectra are asymmetric, arising from the relatively high field modulation. Note that the CW peak at 1560 nm originates from the residual pump power from the 1845 nm cavity. The FWHM of the soliton generated at 1480 nm is 4.64 nm, while the FWHM of the soliton generated at 1845 nm is 2.96 nm. The dips shown near the 1845 nm originates from the water absorption lines around 1900 nm region.

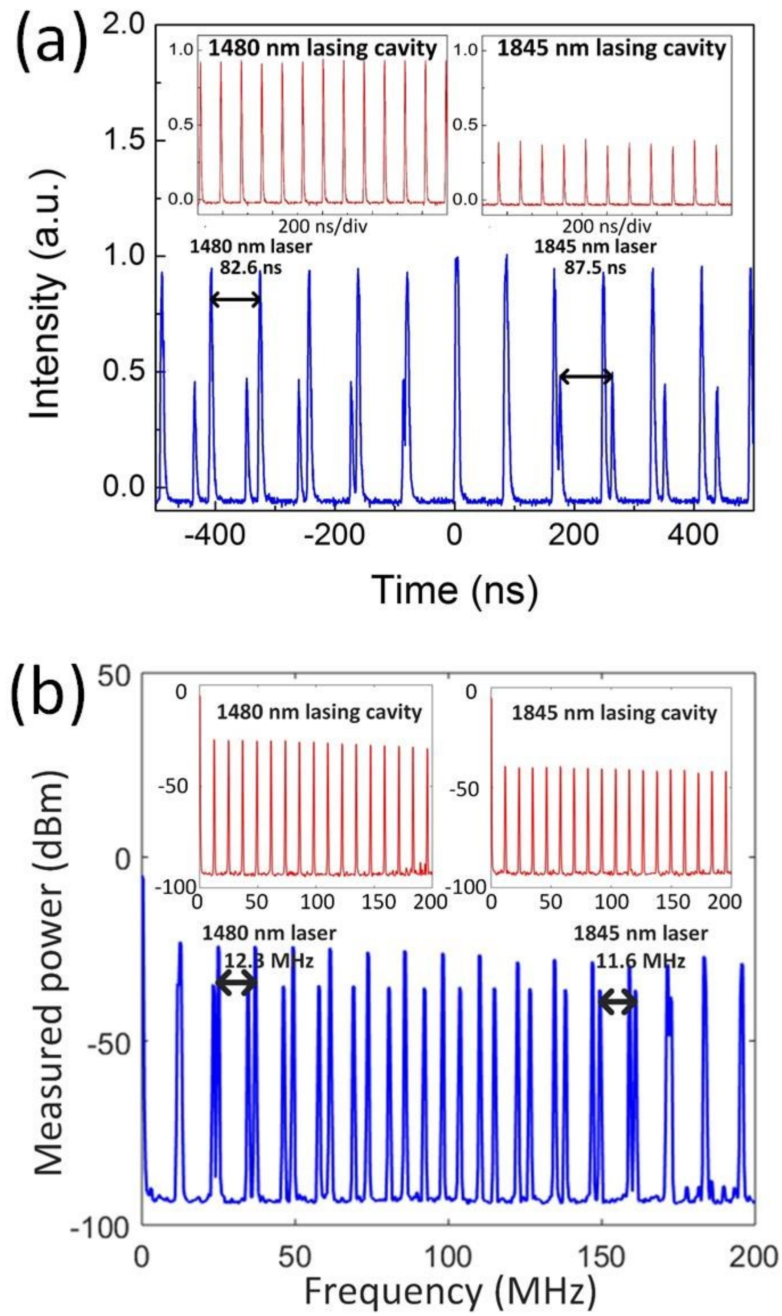

Fig. 4.8 Combined (a) temporal pulse trains and (b) RF spectra of the unsynchronized mode-locked dual-band Tm^{3+}:ZBLAN fiber laser when both cavities operate (P_{1064}= 682 mW, P_{1560}=900 mW). The insets show the pulse trains at the two wavelengths when they operate independently.

Fig. 4.8 shows the dual-band mode-locked pulse trains in the time domain along with the corresponding RF spectra when both cavities are active (P_{1064}=682 mW and P_{1560}=900 mW). When the two cavities are alive, the generated pulse trains at the two wavelengths operate independently with two different fundamental frequencies, as the fundamental frequency of mode-locking operation relies on the cavity length. The pulse trains at 1480 nm have a separation of 82.6 ns corresponding to a fundamental frequency of ~12.3 MHz, while the pulse trains at 1845 nm have a separation of 87.5 ns corresponding to a fundamental frequency of ~11.6 MHz, due to the longer cavity length at 1845 nm used for the unsynchronized dual-band mode-locking operation. The RF SNRs all exceed 50 dB, further demonstrating stable mode-locking operation at the two lasing wavelengths.

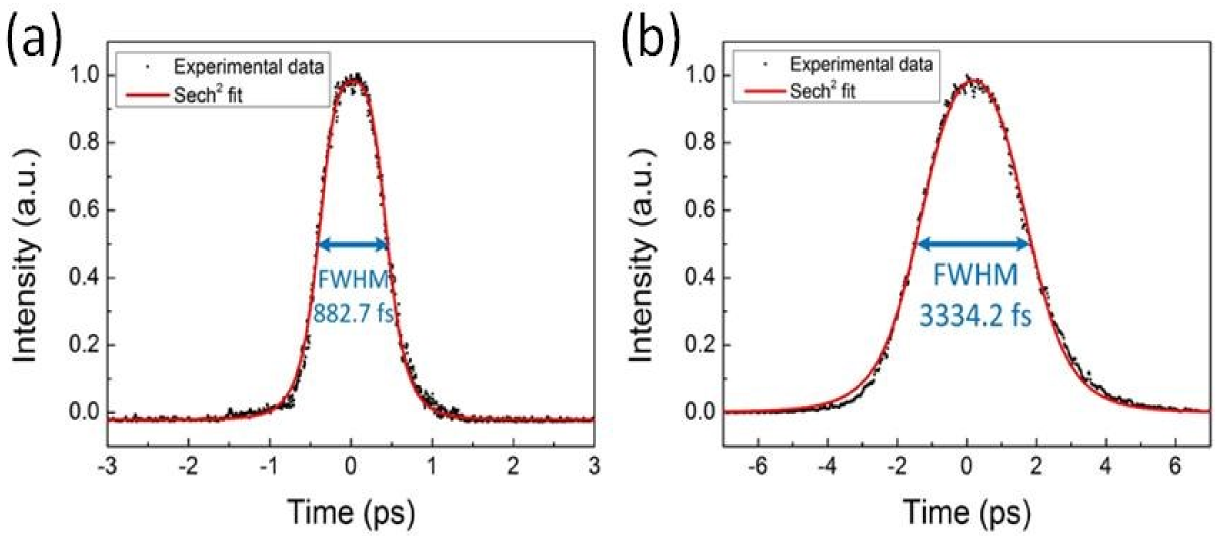

Fig. 4.9 Autocorrelation traces of the output pulses at (a) 1480 nm (P_{1064}= 682 mW, P_{1560}=0 mW) and (b) 1845 nm (P_{1064}=0 mW, P_{1560}=900 mW) from the unsynchronized mode-locked dual-band Tm^{3+}:ZBLAN fiber laser.

Fig. 4.9(a) and (b) shows the measured autocorrelation traces of the unsynchronized dual-band mode-locked pulses at 1480 nm and 1845 nm as well as sech^2 fits, respectively. For 1480 nm mode-locking operation, the pulse width after deconvolution is ~572 fs. Considering the measured FWHM bandwidth of 4.64 nm at 1480 nm, the corresponding time bandwidth product (TBWP) is 0.36, which is slightly larger than the transform-limit value of 0.315, indicating that the output pulses are slightly chirped at the output. The autocorrelator at 1845 nm requires a higher peak power to initiate the pulse width measurement. Hence, we use a Tm^{3+}:silica fiber amplifier to amplify the mode-locked pulses at 1845 nm, and pulse broadening occurs in the amplifier. For 1845 nm mode-locking operation, the pulse width after deconvolution is ~2.16 ps. Considering the measured FWHM bandwidth of 2.96 nm at 1845 nm, the corresponding TBWP is 0.56.

C. Synchronized results and discussion

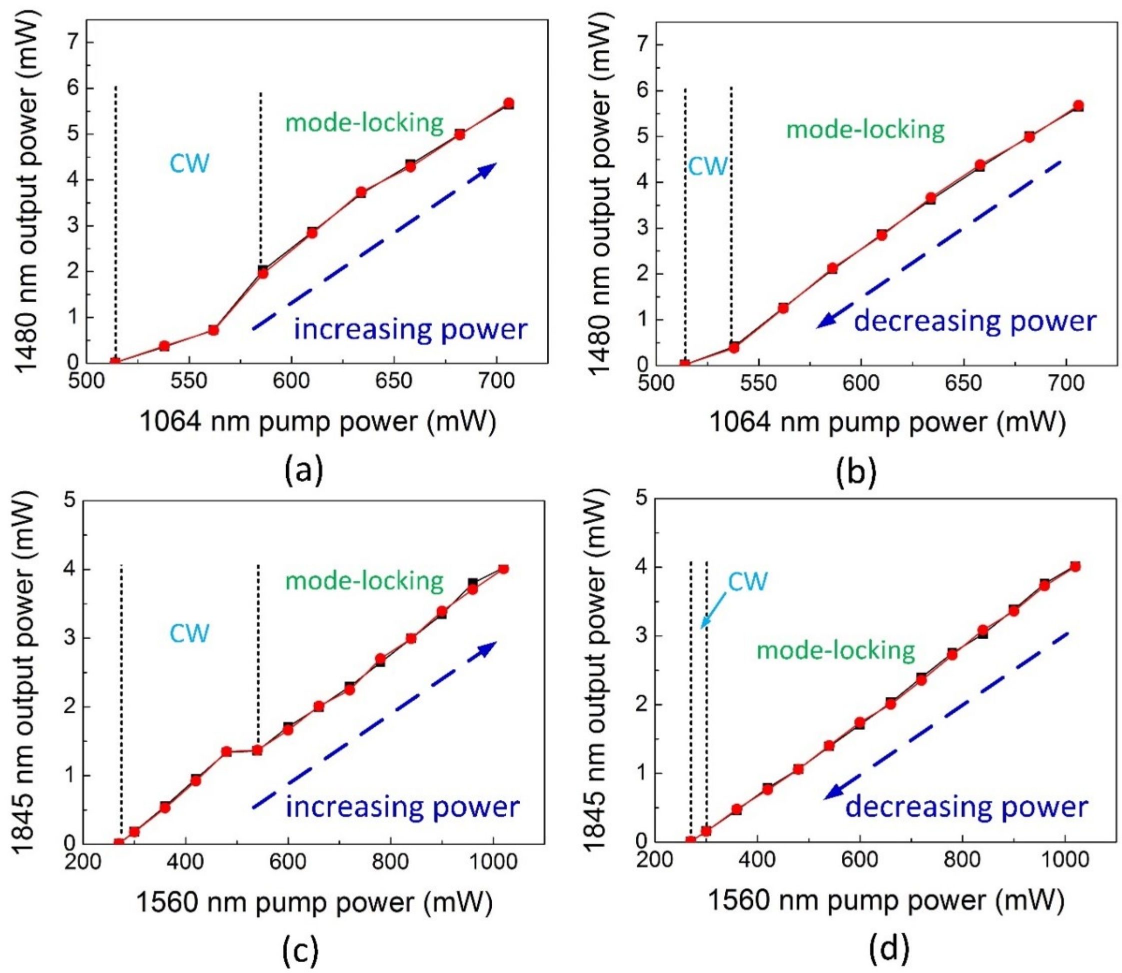

Fig. 4.10 Characteristics of the synchronized mode-locked dual-band Tm^{3+}:ZBLAN fiber laser. Measured output power at 1480 nm when the 1845 nm cavity is on (P_{1560}=900 mW, black curve) and off (P_{1560}=0 mW, red curve) as P_{1064} increases (a) and decreases (b). Measured output power at 1845 nm when the 1480 nm cavity is on (P_{1064}=682 mW, black curve) and off (P_{1064}=0 mW, red curve) as P_{1560} increases (c) and decreases (d).

By carefully adjusting the lengths of SMF-28 and ODL, synchronized dual-band mode-locking operation at 1480 nm and 1845 nm is obtained when the two cavity lengths are the same. Fig. 4.10 shows the laser output power at 1480 nm and 1845 nm along with the corresponding lasing operation regimes as a function of 1064 nm and 1560 nm pump power[(a, c) show increasing pump power, while (b, d) show decreasing pump power], respectively.

In our experiment, CW lasing at 1480 nm occurs at a threshold P_{1064} of 514 mW. When the 1064 nm pump power is increased to 586 mW, the laser's output power at 1480 nm increases obviously and its corresponding optical spectrum is broadened significantly by carefully adjusting the PC. As 1064 nm pump powers increase from 586 mW up to 706 mW, stable fundamental mode-locking operation at 1480 nm is observed and maintained. In order to protect the graphene SA, the 1064 nm pump power is controlled below 710 mW. When the 1064 nm pump power is decreased from 706 mW down to 538 mW, stable mode-locking pulses are maintained. When the 1064 nm pump power is further decreased from 538 mW, CW lasing operation at 1480 nm reappears without optical spectrum broadening until the lasing threshold of 514 mW.

Similar characteristics are observed in the 1845 nm loop. CW lasing at 1845 nm starts at a threshold P_{1560} of 270 mW, and stable fundamental mode-locking operation at 1845 nm is initiated at 540 mW and maintained until 1020 mW. As the 1560 nm pump power decreases from 1020 mW, mode-locking operation is continued until the 1560 nm pump power reaches 300 mW. CW lasing re-appears as the 1560 nm pump power decreases from 300 mW to 270 mW.

Note that slight adjustment of PCs in both branches is required in order to initiate the mode-locking operation. These two linear cavities operate independently. During simultaneous dual-band mode-locking operation, any adjustment of single PC in one cavity does not affect the mode-locking operation of the other one. To demonstrate these two cavities operating independently, we re-measure the output powers at 1480 nm and 1845 nm when the other cavity is set to operate in the mode-locking regime, respectively, as shown in the black squares of Fig. 4.10. The same evolution of output powers and lasing operating regimes are obtained whether or not the other cavity is active, indicating these two lasing cavities operate independently.

In contrast to the Q-switched operation, we ascribe the mode-locking synchronization to a combination of cross-phase modulation along with the saturable absorption effect in the graphene SA. If the graphene SA is placed between the Tm^{3+}:ZBLAN fiber and the gold tipped mirror to make the lasing signal propagate through the graphene twice in each oscillation, no mode-locking output is obtained. Instead of a ring cavity configuration, a linear cavity configuration is adopted owing to the high cavity loss, low handling power of graphene SA, along with the limited pump powers. However, we believe that a ring cavity configuration can realize the dual-band mode-locking operation if the splicing loss between the Tm^{3+}:ZBLAN fiber and SMF-28 is reduced, higher pump powers are used, and the damage threshold of graphene SA is improved by evanescent field interaction [90]. Furthermore, no wavelength selective filters are applied in the dual-band fiber laser. If any tunable wavelength selective filter is added into the cavity, tunable wavelength operation might be realized.

Fig. 4.11 shows the typical optical spectrum of synchronized mode-locked dual-band laser, demonstrating the ultra-broadband mode-locking operation at 1480 nm and 1845 nm simultaneously. The insets show the optical spectra within a 50 nm span centered at each lasing wavelength with a 0.05 nm resolution. The net dispersions of both cavities are anomalous, indicating the two cavities generate soliton-like pulses, which are also confirmed by the characteristics Kelly sidebands. Note that the CW peak at 1560 nm originates from the residual pump power from the 1845 nm cavity. The FWHM of the soliton generated at 1480 nm is 4.48 nm, while the FWHM of the soliton generated at 1845 nm is 3.54 nm. The dips shown near the 1845 nm originates from the water absorption lines around 1900 nm region.

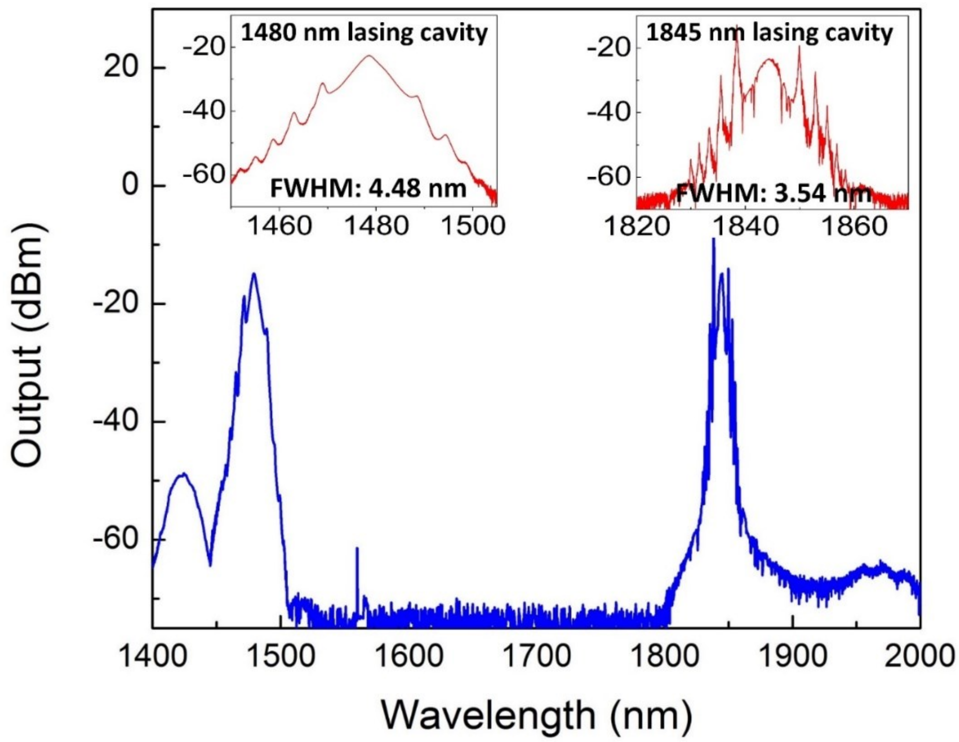

Fig. 4.11 Optical output spectra of the synchronized mode-locked dual-band Tm^{3+}:ZBLAN fiber laser when both cavities operate (P_{1064}= 682 mW, P_{1560}=900 mW). The insets show the optical output spectra at the two wavelength within a 50-nm span with typical Kelly sidebands.

Fig. 4.12 shows the dual-band mode-locked pulse trains in the time domain along with the corresponding RF spectra when both cavities are active (P_{1064}=682 mW and P_{1560}=900 mW). The combined pulse trains with a separation of 82.6 ns coincide with the individual pulse trains at 1480 nm and 1845 nm shown in the insets of Fig. 4.12(a), indicating that pulses at the two wavelengths are completed synchronized. Such a pulse separation also corresponds to the fundamental frequency of 12.3 MHz, which is further confirmed by the combined and individual RF spectra shown in Fig. 4.12(b). The RF SNRs all exceed 60 dB, demonstrating a high degree of synchronization between the mode-locked pulses at 1480 nm and 1845 nm.

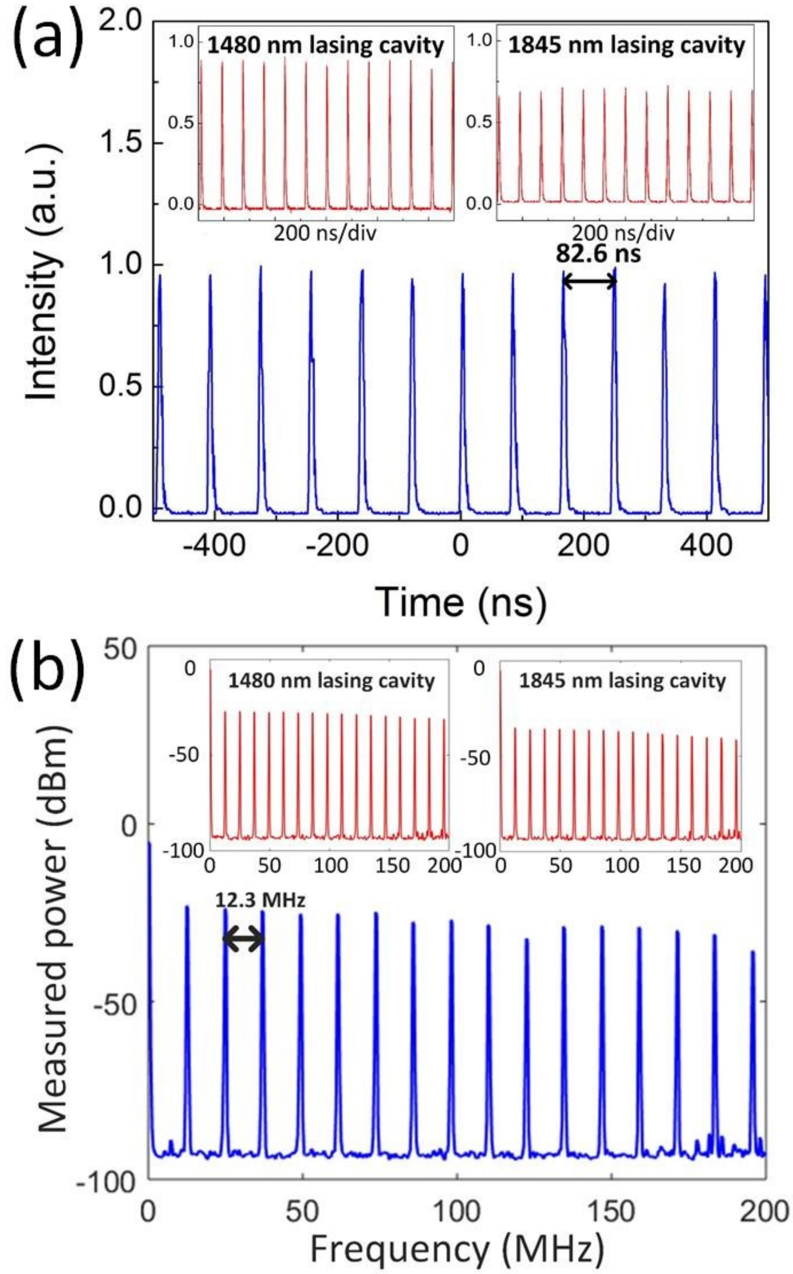

Fig. 4.12 Combined (a) temporal pulse trains and (b) RF spectra of the synchronized mode-locked dual-band Tm^{3+}:ZBLAN fiber laser when both cavities operate (P_{1064}= 682 mW, P_{1560}=900 mW). The insets show the pulse trains at the two wavelengths when they operate independently.

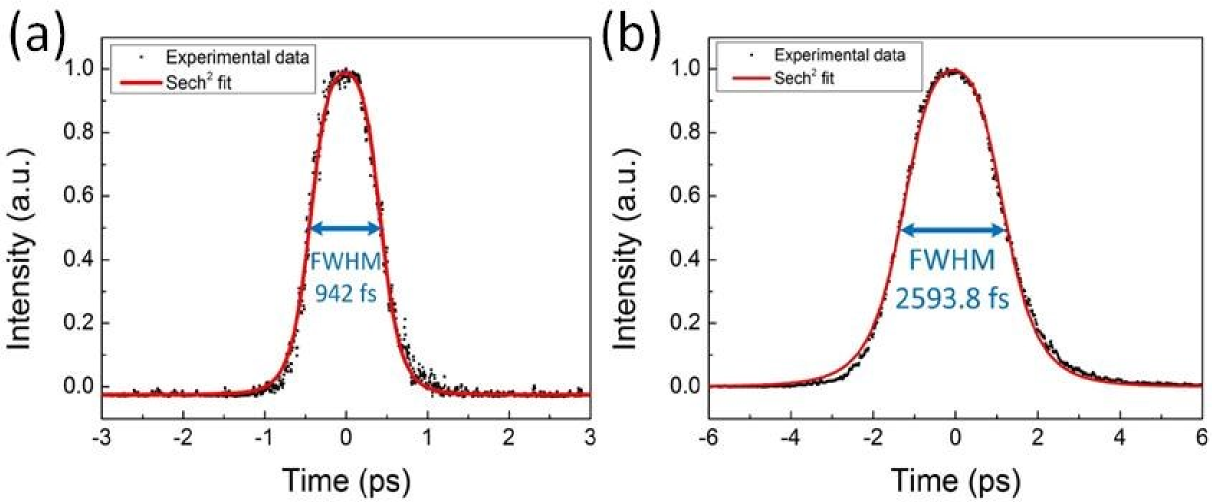

Fig. 4.13 Autocorrelation traces of the output pulses at (a) 1480 nm (P_{1064}= 682 mW, P_{1560}=0 mW) and (b) 1845 nm (P_{1064}=0 mW, P_{1560}=900 mW) from the synchronized mode-locked dual-band Tm^{3+}:ZBLAN fiber laser.

Fig. 4.13(a) and (b) show the measured autocorrelation traces of the synchronized dual-band mode-locked pulses at 1480 nm and 1845 nm as well as sech^2 fits, respectively. For 1480 nm mode-locking operation, the pulse width after deconvolution is ~610 fs. Considering the measured FWHM bandwidth of 4.48 nm at 1480 nm, the corresponding TBWP is 0.37, which is slightly larger than the transform-limit value of 0.315, indicating that the output pulses are slightly chirped at the output. The autocorrelator at 1845 nm requires a higher peak power to initiate the pulse width measurement. Hence, we use a Tm^{3+}:silica fiber amplifier to amplify the mode-locked pulses at 1845 nm, and pulse broadening occurs in the amplifier. For 1845 nm mode-locking operation, the pulse width after deconvolution is ~1.68 ps. Considering the measured FWHM bandwidth of 3.54 nm at 1845 nm, the corresponding TBWP is 0.52. Compared with the unsynchronized dual-band mode-locking operation, the pulse widths at 1480 nm are comparable, while the pulse width at 1845 nm is shorter for the synchronized operation, owing to the lack of cross-phase modulation in the graphene SA for the unsynchronized operation.

D. Summary

We have demonstrated a simultaneous mode-locked dual-band Tm^{3+}:ZBLAN fiber laser at 1480 nm and 1845 nm with synchronized or unsynchronized operation. With different cavity lengths at 1480 nm and 1845 nm, unsynchronized dual-band mode-locking operation at 1480 nm and 1845 nm is obtained with pulse durations of 572 fs and 2.16 ps, and fundamental frequency of 12.3 MHz and 11.6 MHz, respectively. With cavity length matching, synchronized dual-band mode-locking operation at 1480 nm and 1845 nm is obtained with pulse durations of 610 fs and 1.68 ps, respectively, and a synchronized repetition rate of 12.3 MHz. These dual-band mode-locked fiber lasers further confirm the use of the graphene SA to realize dual-band mode-locking operation with controllable fundamental frequencies by adjusting the cavity lengths. They can be used to develop optical transmitters in the S-band and newly exploited optical transmission window around 1900 nm. They will also be important as pump sources for supercontinuum generation at longer wavelengths [91].

4.4 Conclusion

In this chapter, we have demonstrated the use of single gain medium - Tm^{3+}:ZBLAN, as well as the graphene SA to achieve pulsed lasing operation, including (1) a passively synchronized Q-switched dual-band fiber laser at 1480 nm and 1840 nm, and (2) a simultaneous (synchronized or unsynchronized) mode-locked dual-band fiber laser at 1480 nm and 1845 nm.

We have demonstrated a passively synchronized dual-band Q-switched Tm^{3+}:ZBLAN fiber laser at 1480 nm and 1840 nm. Based on a common graphene SA, dual-band Q-switched operation with synchronized repetition rate from 20 kHz to 40.5 kHz is achieved. The dual-band Q-switched fiber laser will generate synchronized high power nano-second pulses in the S-band and around 1900 nm, which will be important in the fields of spectroscopy, communication and nonlinear frequency conversion.

We also have demonstrated a simultaneous (synchronized or unsynchronized) dual-band mode-locked Tm^{3+}:ZBLAN fiber laser at 1480 nm and 1845 nm. By adjusting the cavity lengths at the two wavelengths, synchronized and unsynchronized mode-locked fiber lasers with controllable fundamental frequencies are realized. These dual-band mode-locked fiber lasers further demonstrate the fast response time and ultra-broadband operation of graphene SA, and are expected to develop optical transmitters in the S-band and around 1900 nm.

Chapter 5

Tm^{3+}:ZBLAN fiber lasers at 1.9 μm and 2.3 μm

5.1 Introduction

Tm^{3+}:ZBLAN fiber is preferred as an excellent rare-earth doped fiber to generate mid-IR lasing operation at 2300 nm due to its unique advantages such as low phonon energy, high stability, and ultra-broadband transparency [39, 92]. For the $^3F_4 \rightarrow {}^3H_5$ transition with resulting emission around 2300 nm, multiphonon emission limits the radiative lifetime of the upper laser level at 2300 nm in the silica host; on the contrary, ZBLAN host has a reduced multiphonon emission rate resulting in a longer radiative lifetime of the upper laser level, beneficial for the lasing operation at 2300 nm [21].

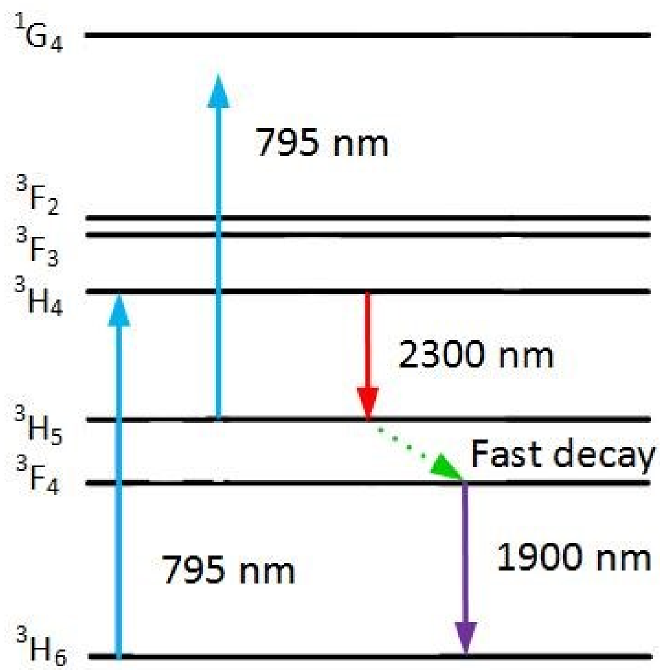

Fig. 5.1 Energy level transitions when pumped at 795 nm to produce dual-band lasing at ~1900 nm and ~2300 nm.

In addition, for the $^3H_4 \rightarrow ^3H_6$ transition with resulting emission around 1900 nm, non-radiative decay has an important influence on the metastable $^3H_4$ manifold, leading to relatively high lasing thresholds in the silica host; on the contrary, much lower thresholds might be possible in the ZBLAN host, as the $^3F_4$ manifold becomes metastable and decay is predominantly radiative. As a consequence, it might be difficult to obtain high output efficiencies in the ZBLAN host, due to the reduced branching ratio from $^3F_4$ to $^3H_4$ [22, 23]. However, through the simultaneous laser oscillation around 2300 nm, the output efficiencies of $^3H_4 \rightarrow ^3H_6$ transition at 1900 nm can be further improved by increasing the branching ratio from $^3F_4$ to $^3H_4$. Previously, there have been several reports on CW co-lasing at 1900 nm and 2300 nm in Tm^{3+}:ZBLAN fiber [21, 22, 93, 94] as well as demonstrated applications in gas sensing [21]. However, these reports were all realized in bulk optics, inducing high cost, less flexibility and less compactness.

In this chapter, we demonstrate a CW Tm^{3+}:ZBLAN all-fiber laser at 1875 nm and 2320 nm, along with a passively Q-switched Tm^{3+}:ZBLAN all-fiber laser at 1895 nm and 2315 nm using a graphene SA with synchronized repetition rate from 10.8 kHz to 25.2 kHz. Such sources can add new capabilities in the newly exploited optical transmission window around 2000 nm or for sensing and gas concentration detection [5, 21, 92].

5.2 CW Tm^{3+}:ZBLAN fiber laser at 1875 nm and 2320 nm

A. Experimental setup

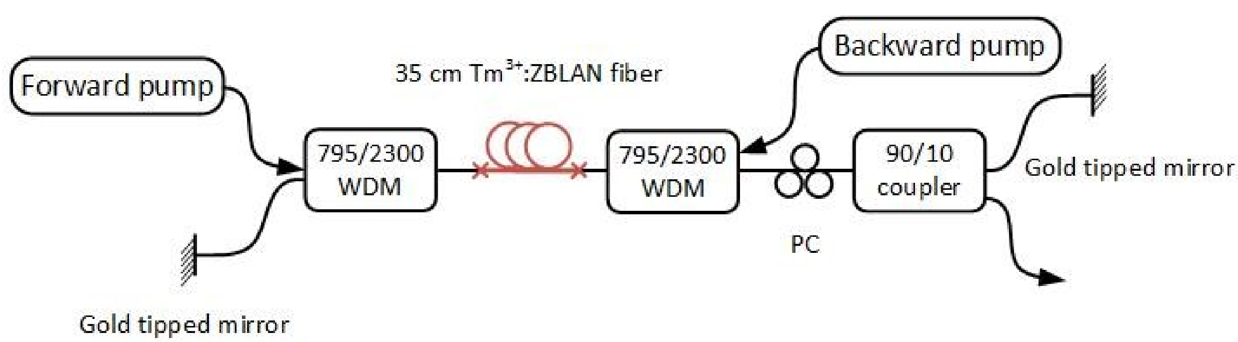

Fig. 5.2 CW Tm^{3+}:ZBLAN all-fiber laser configuration.

Fig. 5.2 shows the schematic of our CW Tm^{3+}:ZBLAN all-fiber laser at 1875 nm and 2320 nm. We adopt a linear cavity configuration along with a bidirectional pumping scheme using two 795 nm multi-mode laser diodes with maximum outputs of 5 W. The pump and lasing signals are coupled via two 795/2000 WDM couplers into the gain fiber. The gain fiber is a 35 cm length of Tm^{3+}:ZBLAN fiber, the same gain fiber as used in previous experiments. The Tm^{3+}:ZBLAN fiber is coupled with the DC silica fiber (FUD4070, Nufern) from two WDM couplers through a pair of glue splices (represented by $\times$ in Fig. 5.2), inducing 2 dB losses per pair. A PC with SM2000 fiber is used to adjust the intra-cavity polarization and to optimize the laser output. Two gold-tipped mirrors, serving as reflectors, are used to define the two ends of the linear lasing cavity. An optical coupler with a splitting ratio of 90/10 is employed to extract the laser output (10% as the output port). The total cavity length of the CW all-fiber laser is ~ 23.2 m, and the estimated cavity loss is ~ 10.5 dB.

The optical spectrum is measured by an OSA (YOKOGAWA, AQ6375) with a wavelength range from 1200 nm to 2400 nm and a resolution bandwidth of 0.05 nm. Output powers are measured by a power meter (Thorlabs, PM100D) along with a thermal power sensor (Thorlabs, S302C). Note that all the pump powers shown below are measured after the WDM couplers. In order to protect the glue splicing between the Tm^{3+}:ZBLAN and silica fiber, the maximum forward and backward pump powers are controlled below 1000 mW.

B. Results and discussion

Fig. 5.3 shows the CW lasing thresholds at 1875 nm and 2320 nm as functions of the bidirectional pump powers. Since the optical coupler and the PC are not optimized for operation out to 2300 nm, CW lasing at 2320 nm requires higher forward pump power to start under the same backward pump power than that at 1875 nm, and vice versa. In addition, the forward pump can stimulate more ASEs to initiate the CW lasing. As an example, if the forward pump power is preset as 600 mW, we need to increase the backward pump powers to 505 mW and 630 mW to start the CW lasing at 1875 nm and 2320 nm, respectively; on the contrary, if the backward pump power is preset as 600 mW, we need to increase higher forward pump powers to 520 mW and 640 mW to start the CW lasing at 1875 nm and 2320 nm, respectively

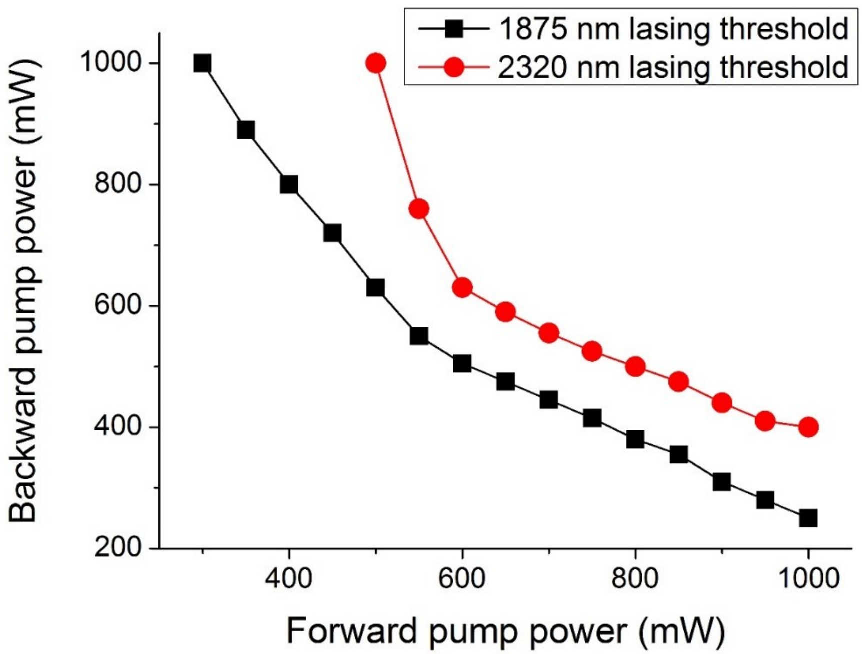

Fig. 5.3 CW lasing thresholds at 1875 nm and 2320 nm as functions of forward and backward pump powers.

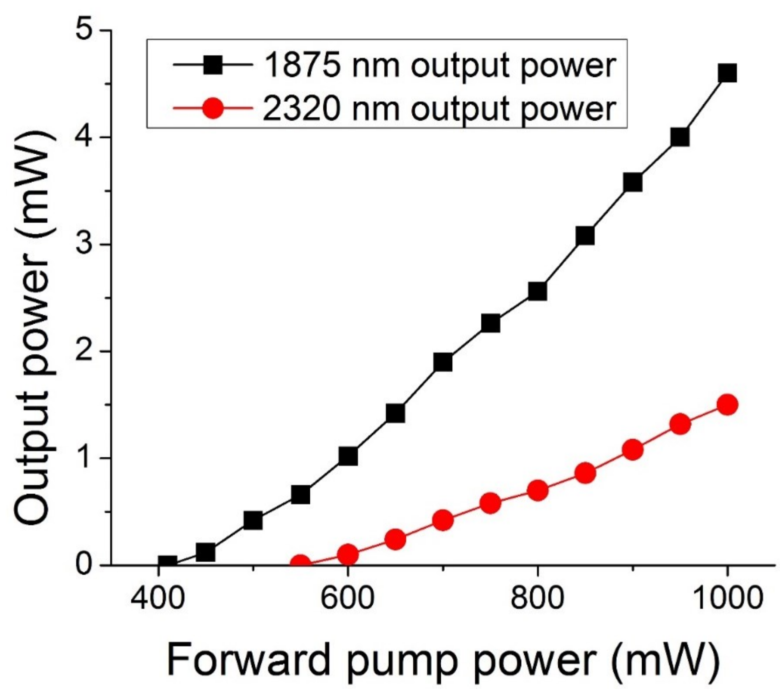

Fig. 5.4 Optical output powers at 1875 nm and 2320 nm as a function of forward pump power when the backward pump power is 800 mW

Fig. 5.4 shows the optical output powers at 1875 nm and 2320 nm as a function of the forward pump power when the backward pump is preset as 800 mW. CW lasing at 1875 nm starts at the forward pump power of 405 mW with a slope efficiency of 0.78%, while CW lasing at 2320 nm starts at the forward pump power of 550 mW with a slope efficiency of 0.33%. Such low slope efficiencies result from the relatively high cavity loss, especially for lasing operation at 2300 nm. The maximum output powers at 1875 nm and 2320 nm can reach ~4.6 mW and ~1.5 mW, respectively. We believe that if the glue splicing is replaced by other methods such as fusion splicing or laser splicing for higher handling power and lower splicing loss, higher output powers and higher output efficiencies at the two wavelengths are expected. Moreover, no pulsed operation (Q-switched or mode-locked) is observed when tuning the two pumps.

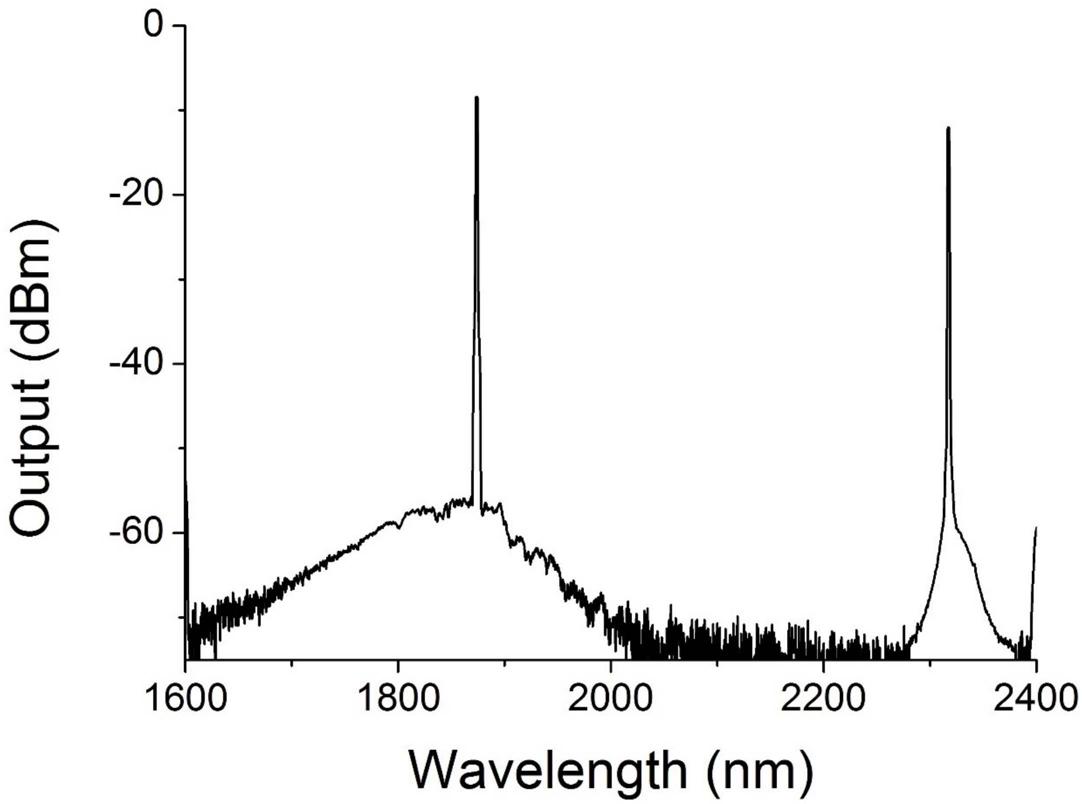

Fig. 5.5 Optical output spectrum of the CW Tm^{3+}:ZBLAN fiber laser when the forward and backward pump powers are both ~800 mW.

Fig. 5.5 shows a typical optical output spectrum of the CW Tm^{3+}:ZBLAN fiber laser with co-lasing at 1875 nm and 2320 nm when both pump powers are ~800 mW. The two lasing central wavelengths are located at 1874.03 nm and 2317.6 nm with an FWHM of ~0.07 nm and ~0.08 nm, respectively. Note that the lasing peak around 2400 nm results from the 3rd order diffraction from the 795 nm pump.

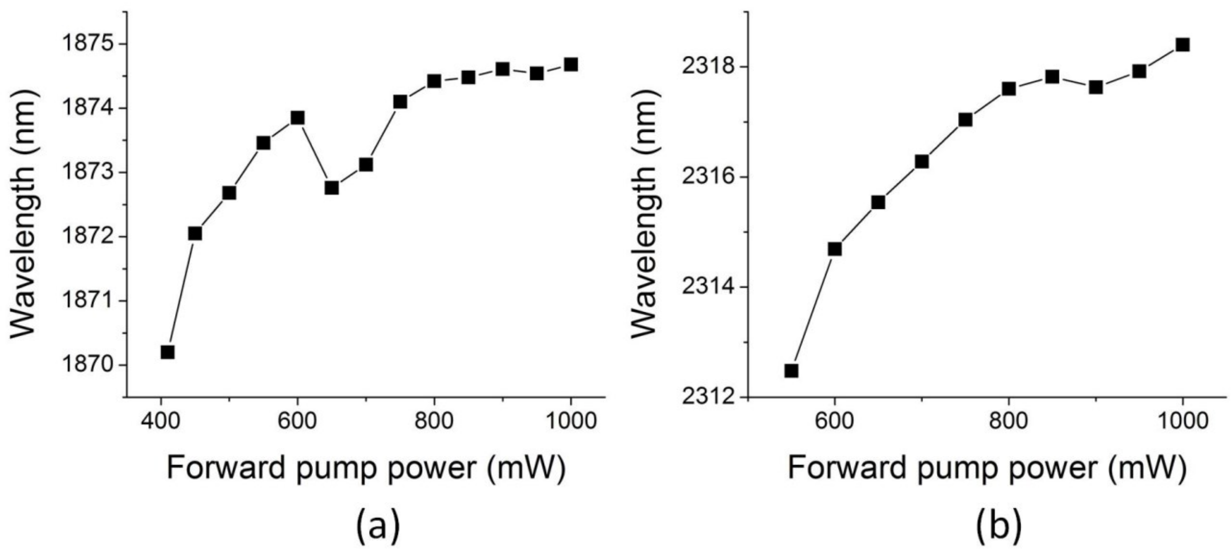

Fig. 5.6 Variations in lasing wavelength at (a) ~ 1875 nm and (b) ~ 2320 nm as a function of forward pump power when the backward pump power is ~ 800 mW.

Fig. 5.6 shows the variations of the central lasing wavelengths at 1875 nm and 2320 nm as a function of the forward pump power for a preset backward pump power of 800 mW. Since higher pump powers can stimulate emission towards longer wavelength, the central lasing wavelengths both increase as the forward pump power increases. As the forward pump power is increased from 800 mW to 1000 mW, both lasing wavelengths maintain around 1875 nm and 2318 nm, as the gain at these two wavelengths is substantially saturated. Note that for all the above measurements, the PC is fixed without any changes of polarization state.

C. Summary

We have demonstrated a CW Tm^{3+}:ZBLAN all-fiber laser at 1875 nm and 2320 nm. Using a single linear cavity configuration, CW co-lasing operation at the two wavelengths is obtained under a bidirectional pumping scheme at 795 nm. The maximum output powers at 1875 nm and 2320 nm can reach ~4.6 mW and ~1.5 mW, respectively.

5.3 Simultaneous Q-switched Tm^{3+}:ZBLAN fiber laser at 1895 nm and 2315 nm using graphene SA

A. Experimental setup

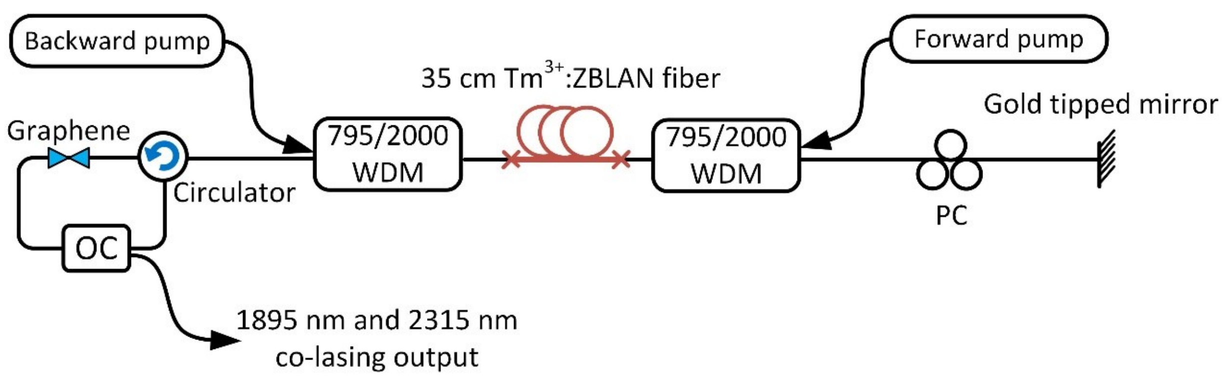

Fig. 5.7 Graphene-based Q-switched Tm^{3+}:ZBLAN all-fiber laser configuration.

Fig. 5.7 shows the schematic of our passively Q-switched Tm^{3+}:ZBLAN all-fiber laser at 1895 nm and 2315 nm using a graphene SA. We adopt a bidirectional pumping scheme with two 795 nm multi-mode laser diodes in a linear cavity configuration. The pump and lasing signals are coupled using two 795/2000 nm WDM couplers. The linear laser cavity is defined by one gold-tipped mirror on one end and a loop mirror on the other. The gain medium is a 35 cm length of DC Tm^{3+}:ZBLAN fiber, the same gain fiber as used in the previous experiment. The gain fiber is coupled with the DC silica fiber (FUD4070, Nufern) via two WDMs through a pair of glue splices (represented by × in Fig. 5.7), inducing 2 dB losses per pair. A PC with SM2000 fiber is used to adjust the intra-cavity polarization and to optimize the laser output. A circulator, a graphene SA, and an optical coupler (OC) constitute the loop mirror and are all based on SMF-28 fiber. The circulator has a transmission loss of ~ 0.5 dB around 1900 nm and ~ 1.5 dB around 2300 nm and forces the signal to propagate counter-clockwise. The graphene film is deposited and sandwiched between two FC/APC connectors to form the SA [79]. The laser output is extracted from the 10% port of the OC. The total cavity length of the Q-switched all-fiber laser is ~ 24.5 m and the estimated cavity loss is ~ 14 dB.

The optical spectrum is measured by an OSA (YOKOGAWA, AQ6375). In order to characterize the Q-switched pulses at each wavelength, two bandpass filters around 1900 nm and 2300 nm are separately applied before the laser output to isolate the desired pulses. The temporal pulse trains are measured by a combination of a 7 GHz photodetector (Newport, 818-BB-51F) and a 60 MHz digital oscilloscope (Agilent, 54621A). The RF spectrum is monitored by an electrical spectrum analyzer (ESA, Anritsu, MS2668C). Output powers are measured by a power meter (Thorlabs, PM100D) and a thermal power sensor (Thorlabs, S302C). Note that all the pump power measurements refer to those after the WDM couplers. In order to protect the glue splicing between the Tm^{3+}:ZBLAN and silica fiber, the maximum forward and backward pump powers are controlled below 1000 mW.

B. Results and discussion

Fig. 5.8(a) shows the operating regimes of the fiber laser including CW and Q-switched operation at 1895 nm and 2315 nm as functions of the bidirectional pump powers. Since the optical coupler and circulator are not optimized for operation out to 2300 nm, CW lasing at 2315 nm requires higher backward pump power to be initiated under the same forward pump power, and vice versa. Moreover, the output slope efficiency at 1895 nm is higher than that at 2315 nm. On the other hand, Q-switched lasing at 1895 nm and 2315 nm begins simultaneously as the pump powers increase further. Figs. 5.8(b) and (c) show the variations of the central lasing wavelengths at 1895 nm and 2315 nm as a function of the forward pump power for a fixed backward pump power of ~ 850 mW. As the forward pump power increases, the central wavelengths both increase, indicating that higher pump powers stimulate emission toward longer wavelengths. Finally, both lasing wavelengths approach and maintain around 1895 nm and 2315 nm as the gain at these two wavelengths is substantially saturated. Similar evaluations of lasing wavelengths at the two wavelengths as a function of the forward pump power are observed when the backward pump power is fixed at 850 mW.

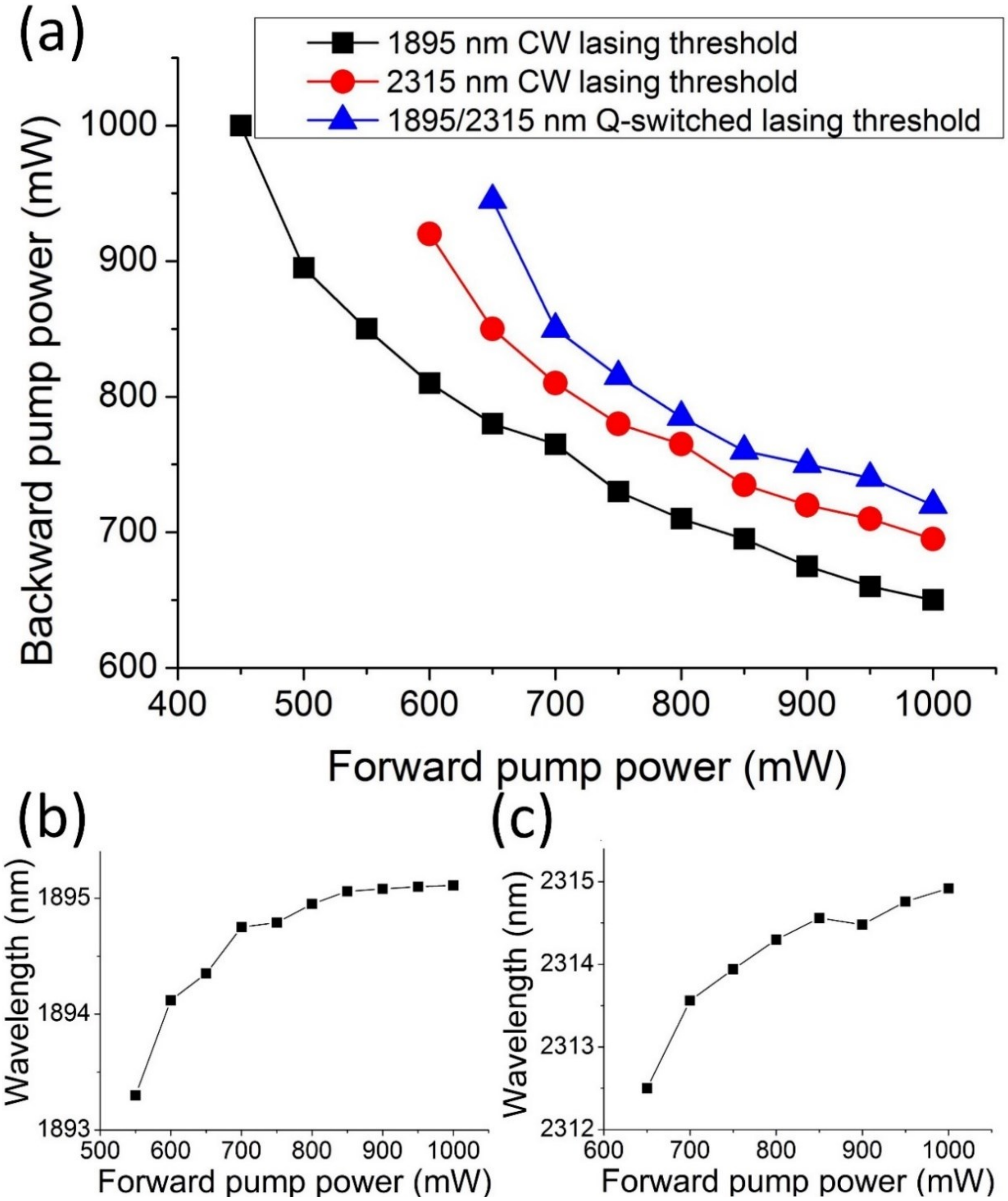

Fig. 5.8 (a) Lasing operation regimes (CW and Q-switched) as functions of forward and backward pump powers. Variations in lasing wavelength at (b) ~ 1895 nm and (c) ~ 2315 nm as a function of forward pump power when the backward pump power is fixed at ~ 850 mW.

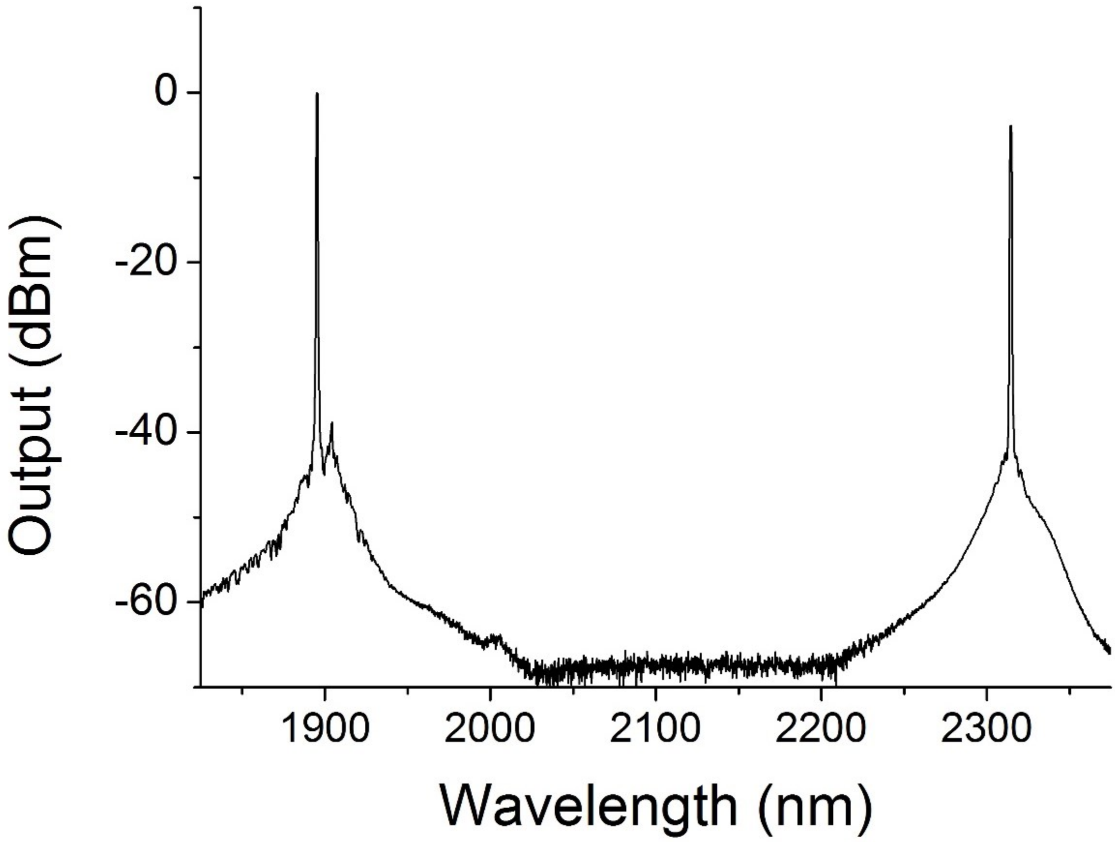

Fig. 5.9 Optical output spectrum of the graphene Q-switched Tm^{3+}:ZBLAN fiber laser when the forward and backward pump powers are both ~850 mW.

Fig. 5.9 shows a typical optical spectrum of the Q-switched Tm^{3+}:ZBLAN fiber laser output when the forward and backward pump powers are both preset as ~ 850 mW. The two lasing lines are at 1895.2 nm and 2314.6 nm with an FWHM bandwidth of ~ 0.06 nm and ~ 0.08 nm, respectively, demonstrating the ultra-broadband operation of the graphene SA with a wavelength separation of ~ 420 nm.

As the pump power increases, Q-switching operation at 1895 nm and 2315 nm continues with a synchronized rate. For example, when the forward and backward pump powers are both fixed at ~ 850 mW, the combined and individual pulse trains at 1895 nm and 2315 nm coincide with each other with the same pulse separation of 57.5 μs as shown in Fig. 5.10. No amplification modulation is observed in each pulse, demonstrating the absence of self-mode-locking effects in

Q-switching operation. The synchronized Q-switching operation is further demonstrated in the corresponding RF spectra shown in Fig. 5.11. These three RF spectra show the same repetition rate of ~ 17.4 kHz with RF SNRs all above 50 dB, highlighting the stability of synchronized Q-switching operation.

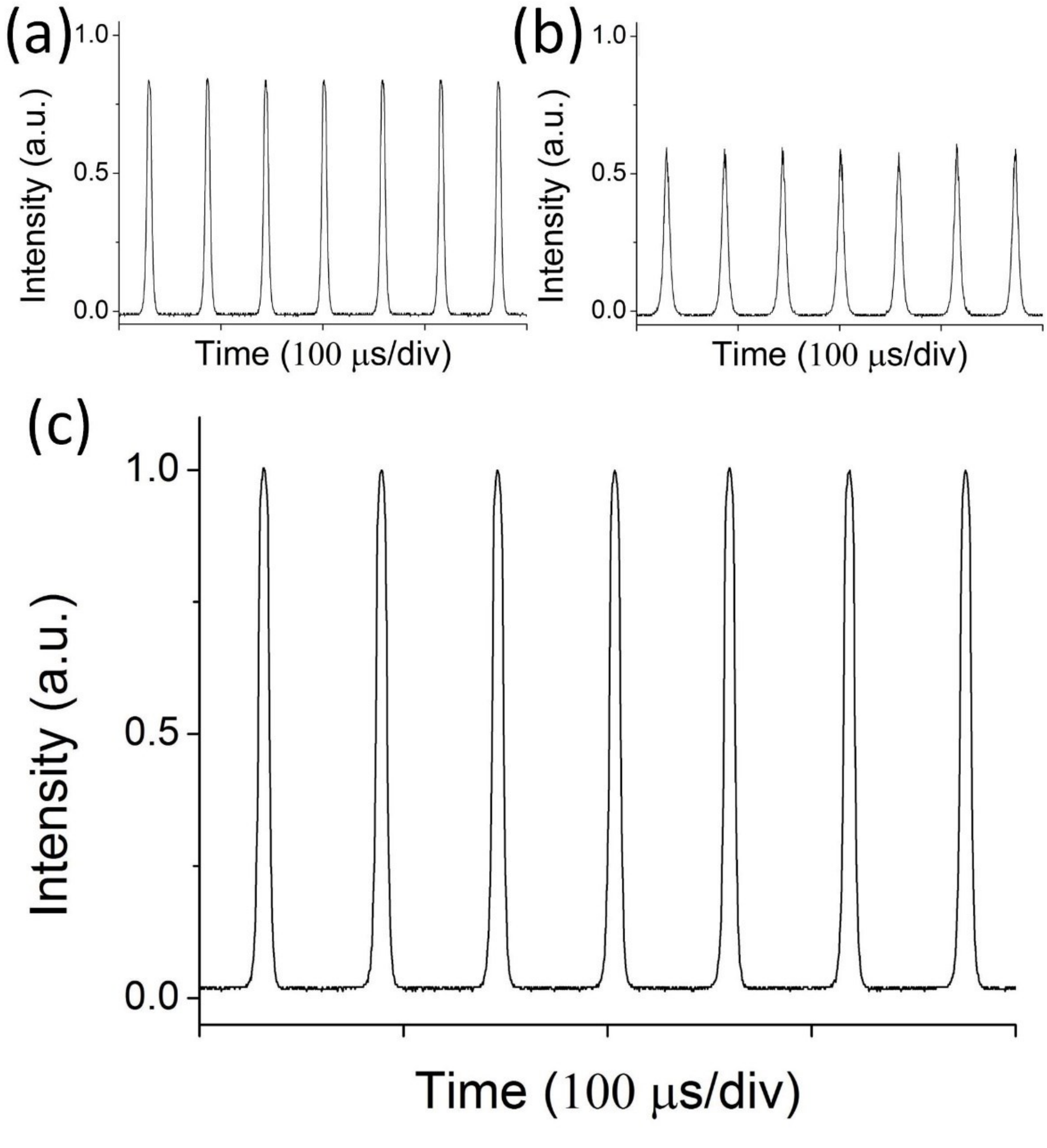

Fig. 5.10 Q-switched pulse trains at (a) 1895 nm, (b) 2315 nm, and (c) both 1895 nm and 2315 nm when the forward and backward pump powers are both ~850 mW.

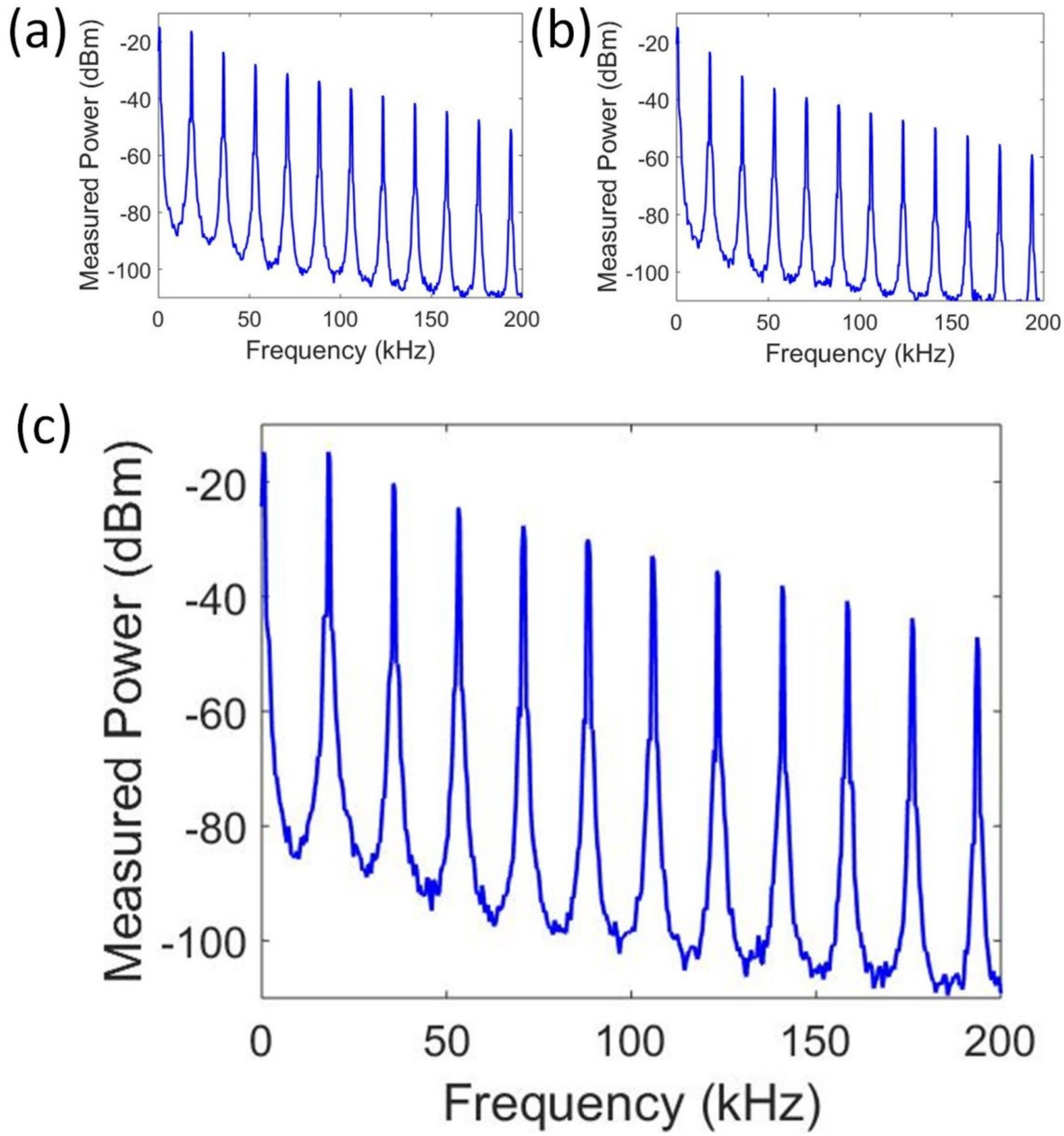

Fig. 5.11 RF spectra of the Q-switched laser operating at (a) 1895 nm, (b) 2315 nm, and (c) both 1895 nm and 2315 nm when the forward and backward pump powers are both ~ 850 mW.

Fig. 5.12 shows the pulse repetition rate and the pulse width at each wavelength measured at different forward pump powers when the backward pump power is fixed at ~ 850 mW. As the forward pump power increases from 700 mW up to 1000 mW, synchronized repetition rate (black dots) increases linearly from 10.8 kHz to 25.2 kHz at a rate of 48 Hz/mW, a typical signature of Q-switching operation. The corresponding pulse widths at 1895 nm (blue square) and 2315 nm (red square) both decrease exponentially first, then keep a level of ~ 4.5 μs due to the bleaching effect of graphene. The corresponding average output powers and the calculated pulse energies as a function of the forward pump power are shown in Fig. 5.13. CW lasing at 1895 nm starts at the forward pump power of ~ 550 mW with a slope efficiency of 0.36%, while CW lasing at 2315 nm starts at the forward pump power of ~ 650 mW with a slope efficiency of 0.22%, due to the lower cavity loss at 1895 nm. The corresponding pulse energies keep increasing linearly, not the same as saturated pulse energy in [14]. We believe that if the glue splicing can handle higher power, higher repetition rate and higher pulse energies could be observed when higher pump powers are added to the system. At a pump power of 1000 mW for each pump, the average output powers at 1895 nm and 2315 nm after filtering are 1.6 mW and 0.8 mW, respectively, while the calculated pulse energies are 63.7 nJ and 30.6 nJ, respectively. The corresponding peak powers could reach 13.3 mW and 5.92 mW, respectively.

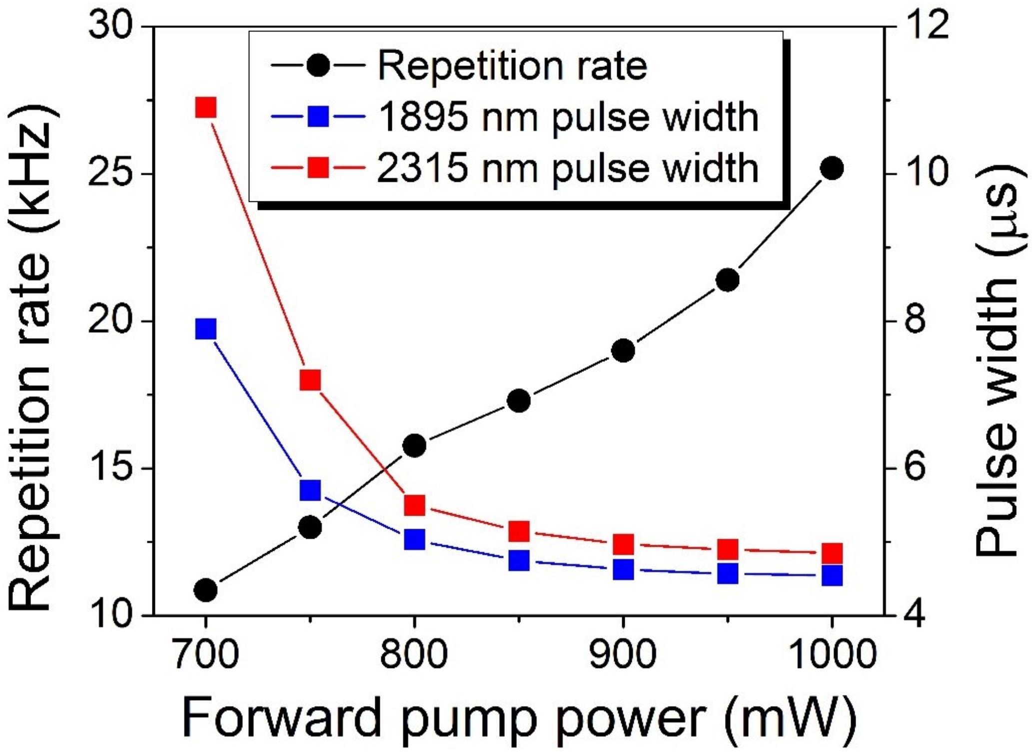

Fig. 5.12 Repetition rate and pulse width of the Q-switched pulses at 1895 nm and 2315 nm as a function of the forward pump power when the backward pump power is ~ 850 mW.

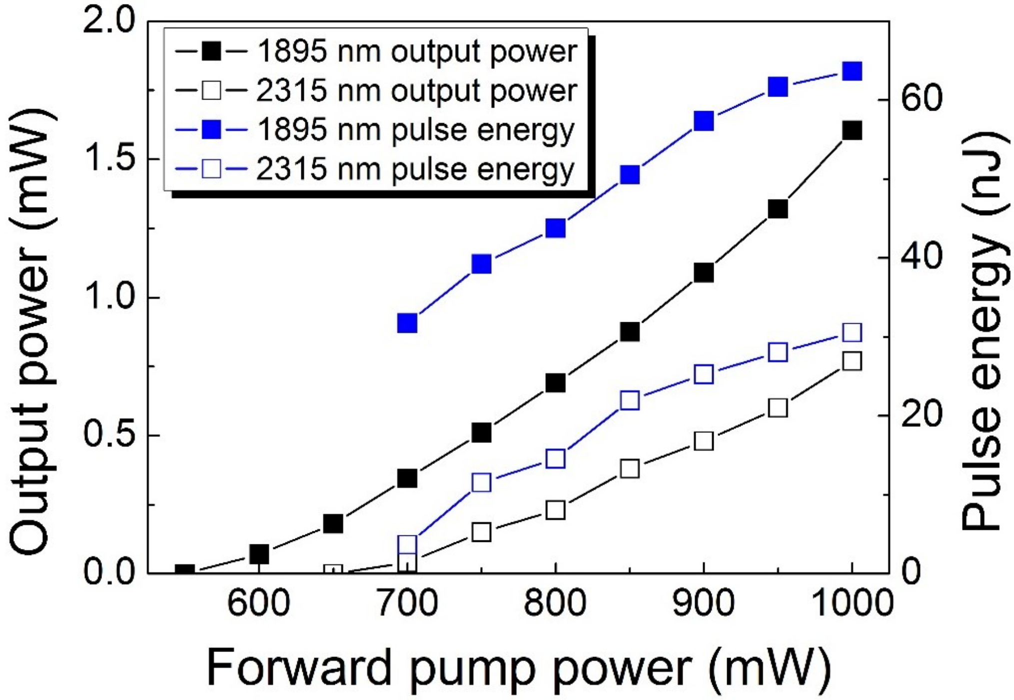

Fig. 5.13 Output power and pulse energy of the Q-switched pulses at 1895 nm and 2315 nm as a function of the forward pump power when the backward pump power is ~ 850 mW.

C. Summary

We have demonstrated a passively Q-switched Tm^{3+}:ZBLAN all-fiber laser at 1895 nm and 2315 nm using a single linear cavity along with a graphene SA. Under a bidirectional pump scheme at 795 nm, Q-switched co-lasing is obtained with a synchronized repetition rate from 10.8 kHz to 25.2 kHz with pulse widths as short as 4.5 μs at 1895 nm and 4.9 μs at 2315 nm. The maximum output powers at 1895 nm and 2315 nm are 1.625 mW and 0.77 mW, respectively, with corresponding calculated pulse energies of 63.7 nJ and 30.6 nJ, and corresponding peak powers of 13.3 mW and 5.92 mW, respectively.

5.4 Conclusion

In this chapter, we have demonstrated the use of Tm^{3+}:ZBLAN fiber to achieve (1) a CW Tm^{3+}:ZBLAN all-fiber laser with co-lasing operation at 1875 nm and 2320 nm, and (2) a passively

Q-switched Tm^{3+}:ZBLAN all-fiber laser at 1895 nm and 2315 nm using a graphene SA with a synchronized repetition rate from 10.8 kHz to 25.2 kHz. These CW and Q-switched dual-band laser sources at 1900 nm and 2300 nm could become low-cost and convenient laser sources for applications on the newly exploited optical transmission window around 2000 nm, near-IR dual-band pulse source for the chemical sensing measurements, and pump sources for mid-IR supercontinuum operation towards longer wavelengths.

Chapter 6

Conclusion and future work

This thesis studies the near-IR Tm^{3+}:ZBLAN fiber lasers. Chapter 1 provided a brief background on fiber lasers and described the needs for near-IR fiber lasers. Chapter 2 discussed the background knowledge on ZBLAN glass, rare earth doping, fiber lasers, as well as the properties of graphene. Chapter 3 demonstrated CW dual-band Tm^{3+}:ZBLAN fiber lasers and a widely tunable and switchable dual-wavelength Tm^{3+}:silica fiber laser. Chapter 4 discussed the pulsed (Q-switched and mode-locked) dual-band Tm^{3+}:ZBLAN fiber lasers. Chapter 5 described CW and Q-switched Tm^{3+}:ZBLAN fiber lasers with co-lasing at 1900 nm and 2300 nm. The main achievements of Tm^{3+}:ZBLAN fiber lasers are listed in the following figure. And the main contributions are summarized as follows:

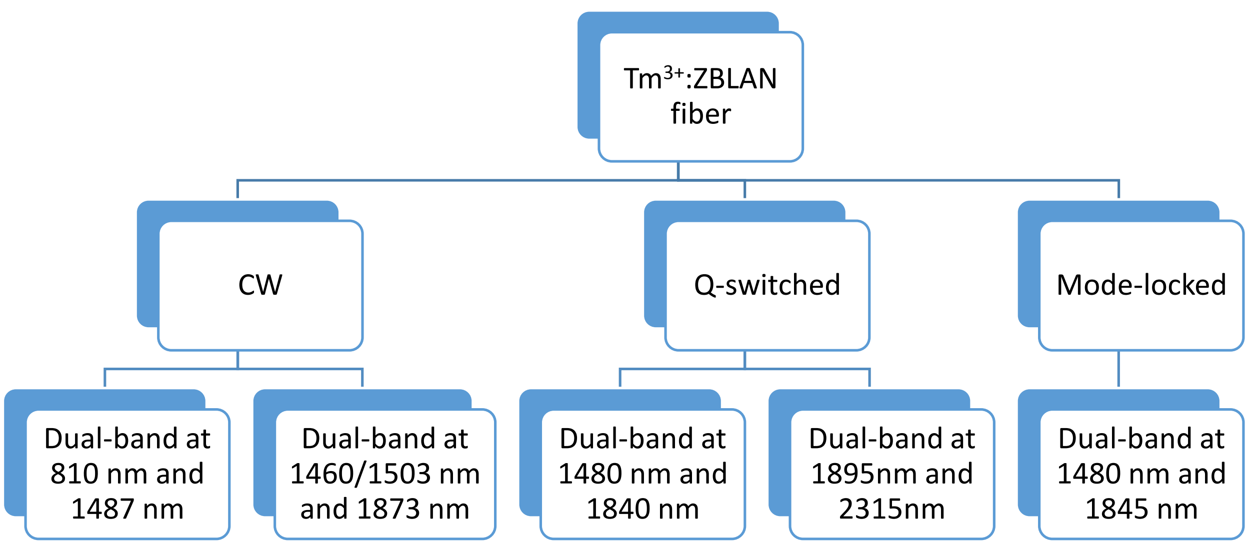

Fig. 6.1 Achievements on Tm^{3+}:ZBLAN fiber laser.

(1) We demonstrated a dual-band Tm^{3+}:ZBLAN fiber laser at 810 nm and 1487 nm using a linear cavity configuration without the use of WDM coupler. By controlling the 1064 nm pump power, single-wavelength operation at 810 nm or 1487 nm, and dual-wavelength operation at both wavelengths are observed. Each wavelength can emit an output power more than 25 mW. Such a dual-band laser located in the first and third tele-communication window may find important applications in bio-sensing, communication and instrumentation.

(2) We demonstrated a dual-band three-wavelength Tm^{3+}:ZBLAN fiber laser emitting simultaneously at 1460 nm, 1503 nm and 1873 nm. Its power fluctuations at three wavelengths are less than 1.5 dB over 30 minutes. Also switchable dual-wavelength operation at 1460 nm and 1503 nm is obtained. Such a three-wavelength fiber laser could be important in the fields of communication, spectroscopy and chemical sensing.

(3) We demonstrated a widely tunable and switchable dual-wavelength Tm^{3+}:silica fiber laser based on the Sagnac loop mirror and Tm^{3+}:silica DC silica fiber, with a tuning range over 70 nm from 1857 nm to 1927 nm. Only by simply controlling the PC in the ring cavity, alternate/sequential switching operation is realized with ~5.4 nm wavelength spacing. This is the largest tuning range reported for a dual-wavelength TDFL. We believe that such a laser can offer capabilities in the fields of fiber optic sensing in the 1900 nm wavelength range, such as LIDAR, multi-wavelength absorption spectroscopy and fiber cavity ring-down spectroscopy.

(4) We demonstrated a passively synchronized dual-band Q-switched Tm^{3+}:ZBLAN fiber laser at 1480 nm and 1840 nm. Based on a common graphene SA, dual-band Q-switched operation synchronized repetition rate from 20 kHz to 40.5 kHz is achieved. Such ultra-broadband synchronized Q-switched pulses will provide high power nanosecond pulses for applications in the fields of nonlinear frequency conversion, spectroscopy and chemical sensing.

(5) We demonstrated a synchronized mode-locked dual-band Tm^{3+}:ZBLAN fiber laser at 1480 nm and 1845 nm. With length adjustment of SMF-28 and ODL, synchronized dual-band mode-locking operation at 1480 nm and 1845 nm is obtained with pulse durations of 610 fs and 1.68 ps, respectively, along with a synchronized repetition rate of 12.3 MHz. The simultaneous mode-locked dual-band fiber laser can be used to develop optical transmitters in the S-band and newly exploited optical transmission window around 1900 nm.

(6) We demonstrated a passively Q-switched Tm^{3+}:ZBLAN all-fiber laser at 1895 nm and 2315 nm using a single linear cavity along with a graphene SA. Using a bidirectional pump scheme at 795 nm, Q-switched co-lasing is obtained with a synchronized repetition rate from 10.8 kHz to 25.2 kHz with pulse widths as short as 4.5 μs at 1895 nm and 4.9 μs at 2315 nm. Such dual band Q-switched lasers around 1900 nm and 2300 nm could become low-cost and convenient laser sources for applications on the newly exploited optical transmission window around 2000 nm, near-IR dual-band pulse source for the chemical sensing measurements, and pump sources for mid-IR supercontinuum operation towards longer wavelengths.

Based on the above achievements, we propose the following future work to further the research on ZBLAN fiber:

(1) Lasing at 2.8 μm based on Er^{3+}:ZBLAN fiber

Mid-IR wavelengths lasers, especially fiber lasers at around 3 μm, have many potential applications in a wide range of fields including military countermeasure applications, medical diagnostics, and light detection for atmospheric and chemical sensing and monitoring. For Er^{3+} ions, transition from $^4I_{11/2}$ to $^4I_{13/2}$ will produce emission at 2.8 μm which is closely linked to the above applications and therefore attracts intense interests [95-97]. Therefore, amplification at 2.8 μm will be investigated. CW and pulsed lasing operation at 2.8 μm needs to be investigated further.

(2) Single-longitudinal-mode Tm^{3+}:ZBLAN fiber laser

Single-longitudinal-mode Er^{3+} doped fiber lasers has been successfully realized under different schemes: the DBR fiber lasers, DFB fiber lasers, ring cavity fiber lasers with embedded narrow-bandwidth filters, injection locked fiber lasers and Brillouin fiber lasers. Here we may use similar ways, such as compound fiber loops to generate a ultra-narrow filter, or use unpumped Tm^{3+}:ZBLAN fiber as saturable absorber, to achieve single-longitudinal-mode operation for microwave generation at 2 μm. The expected eye-safe single-longitudinal-mode ZBLAN fiber laser at 1.9 will have a narrow output linewidth, long laser coherence length, and controlled mode competition, which will be useful for Raman spectroscopy, holography, biomedical and fluorescence.

(3) Stimulated Brillouin scattering in Tm^{3+}:ZBLAN fiber

Stimulated Brillouin scattering (SBS) refers to the interaction of material waves and light within a medium. An incident photon can be converted into a scattered photon with slightly lower energy in the opposite direction, and a phonon. Recent research showed that the power threshold of SBS is much higher in the ZBLAN fiber than in SMF-28, beneficial for telecommunication applications [98]. Also the lower phonon energy in ZBLAN fiber make it a better choice for future telecommunication systems since it is much more difficult to generate SBS in ZBLAN fiber. However, there is limited research on the acousto-optic properties in ZBLAN fiber by using SBS. Therefore, SBS on ZBLAN fiber needs to be investigated further.

References

[1] N. Taylor, *LASER: The inventor, the Nobel laureate, and the thirty-year patent war*: Simon and Schuster, 2002.

[2] T. H. Maiman, "Stimulated optical radiation in Ruby," *Nature,* vol. 187, pp. 493-494, 1960.

[3] E. Snitzer, "Optical maser action of Nd^{+3} in a barium crown glass," *Physical Review Letters,* vol. 7, pp. 444-446, 1961.

[4] R. Mears, L. Reekie, I. Jauncey, and D. Payne, "Low-noise Erbium-doped fibre amplifier operating at 1.54μm," *Electronics Letters,* vol. 19, pp. 1026-1028, 1987.

[5] Z. Li, A. M. Heidt, J. M. O. Daniel, Y. Jung, S. U. Alam, and D. J. Richardson, "Thulium-doped fiber amplifier for optical communications at 2 μm," *Optics Express,* vol. 21, pp. 9289-9297, 2013.

[6] A. Garnache, A. Ouvrard, L. Cerutti, D. Barat, A. Vicet, F. Genty*, et al.*, "2-2.7 μm single frequency tunable Sb-based lasers operating in CW at RT: microcavity and external cavity VCSELs, DFB," in *Photonics Europe*, 2006, pp. 61840N-61840N-15.

[7] B. M. Walsh and N. P. Barnes, "Comparison of Tm : ZBLAN and Tm : silica fiber lasers; Spectroscopy and tunable pulsed laser operation around 1.9 μm," *Applied Physics B,* vol. 78, pp. 325-333, 2004.

[8] T. S. McComb, R. A. Sims, C. C. C. Willis, P. Kadwani, L. Shah, and M. Richardson, "Atmospheric Transmission Testing Using a Portable, Tunable, High Power Thulium Fiber Laser System," *2010 Conference on Lasers and Electro-Optics (Cleo) and Quantum Electronics and Laser Science Conference (Qels),* 2010.

[9] W. J. Peng, F. P. Yan, Q. Li, S. Liu, T. Feng, S. Y. Tan*, et al.*, "1.94 μm switchable dual-wavelength Tm^{3+} fiber laser employing high-birefringence fiber Bragg grating," *Applied Optics,* vol. 52, pp. 4601-4607, 2013.

[10] X. Wang, Y. Zhu, P. Zhou, X. Wang, H. Xiao, and L. Si, "Tunable, multiwavelength Tm-doped fiber laser based on polarization rotation and four-wave-mixing effect," *Optics Express,* vol. 21, pp. 25977-25984, 2013.

[11] W. B. Cho, A. Schmidt, J. H. Yim, S. Y. Choi, S. Lee, F. Rotermund*, et al.*, "Passive mode-locking of a Tm-doped bulk laser near 2 μm using a carbon nanotube saturable absorber," *Optics Express,* vol. 17, pp. 11007-11012, 2009.

[12] G. S. Qin, S. H. Huang, Y. Feng, A. Shirakawa, and K. Ueda, "784-nm amplified spontaneous emission from Tm^{3+}-doped fluoride glass fiber pumped by an 1120-nm fiber laser," *Optics Letters,* vol. 30, pp. 269-271, 2005.

[13] G. S. Qin, S. H. Huang, Y. Feng, A. Shirakawa, and K. I. Ueda, "Multiple-wavelength up-conversion laser in Tm^{3+}-doped ZBLAN glass fiber," *IEEE Photonics Technology Letters,* vol. 17, pp. 1818-1820, 2005.

[14] G. Androz, D. Faucher, D. Gingras, and R. Valle, "Self-pulsing dynamics of a dual-wavelength Tm^{3+}: ZBLAN upconversion fiber laser emitting around 800 nm," *Journal of the Optical Society of America B-Optical Physics,* vol. 24, pp. 2907-2913, 2007.

[15] B. Frison, A. R. Sarmani, L. R. Chen, X. Gu, S. Thomas, P. Long*, et al.*, "Dual-wavelength lasing around 800 nm in a Tm:ZBLAN fibre laser," in *IEEE Photonics Conference*, 2012, pp. 668-669.

[16] B. Frison, A. R. Sarmani, L. R. Chen, X. Gu, and M. Saad, "Dual-wavelength S-band Tm^{3+}: ZBLAN fibre laser with 0.6 nm wavelength spacing," *Electronics Letters,* vol. 49, pp. 60-61, 2013.

[17] K. Ramaswamy, C. Jia, M. Dastmalchi, L. R. Chen, and M. Saad, "Dual-band 810/1480 nm Tm^{3+}: ZBLAN fiber laser," in *IEEE Photonics Conference*, 2013, pp. 273-274.

[18] O. Svelto and D. C. Hanna, *Principles of lasers*. New York: Springer, 2010.

[19] A. Martinez and Z. Sun, "Nanotube and graphene saturable absorbers for fibre lasers," *Nature Photonics,* vol. 7, pp. 842-845, 2013.
[20] F. Bonaccorso, Z. Sun, T. Hasan, and A. Ferrari, "Graphene photonics and optoelectronics," *Nature photonics,* vol. 4, pp. 611-622, 2010.
[21] F. J. McAleavey, J. O'Gorman, J. F. Donegan, B. D. MacCraith, J. Hegarty, and G. Mazé, "Narrow linewidth, tunable Tm^{3+}-doped fluoride fiber laser for optical-based hydrocarbon gas sensing," *IEEE Journal of Selected Topics in Quantum Electronics,* vol. 3, pp. 1103-1111, 1997.
[22] J. N. Carter, R. G. Smart, A. C. Tropper, and D. C. Hanna, "Thulium-doped fluorozirconate fibre lasers," *Journal of Non-Crystalline Solids,* vol. 140, pp. 10-15, 1992.
[23] V. Sudesh and J. A. Piper, "Spectroscopy, modeling, and laser operation of Thulium-doped crystals at 2.3 µm," *IEEE Journal of Quantum Electronics,* vol. 36, pp. 879-884, 2000.
[24] N. L. P. Andrews, A. G. MacLean, J. E. Saunders, J. A. Barnes, H.-P. Loock, M. Saad*, et al.*, "Quantification of different water species in acetone using a NIR-triple-wavelength fiber laser," *Optics Express,* vol. 22, pp. 19337-19347, 2014.
[25] V. Ter-Mikirtychev, *Fundamentals of fiber lasers and fiber amplifiers*: Springer, 2014.
[26] J. Zarzycki, *Glasses and the vitreous state*: Cambridge University Press, 1991.
[27] J. Sanghera and I. D. Aggarwal, *Infrared fiber optics*: CRC Press, 1998.
[28] M. P. M. L. J. Poulain, "Verres fluores au tetrafluorure de zirconium proprietes optiques d'un verre dope au Nd^{3+}," *Materials Research Bulletin Materials Research Bulletin,* vol. 10, pp. 243-246, 1975.
[29] R. M. Percival and J. R. Williams, "Highly efficient 1.064 µm upconversion pumped 1.47 µm Thulium doped fluoride fibre amplifier," *Electronics Letters,* vol. 30, pp. 1684-1685, 1994.
[30] T. Komukai, Y. Fukasaku, T. Sugawa, and Y. Miyajima, "Highly efficient and tunable Nd^{3+} doped fluoride fibre laser operating in 1-3 µm band," *Electronics Letters,* vol. 29, pp. 755-757, 1993.
[31] R. M. El-Agmy, "Upconversion CW laser at 284 nm in a Nd:YAG-pumped double-cladding Thulium-doped ZBLAN fiber laser," *Laser Physics,* vol. 18, pp. 803-806, 2008.
[32] T. Sun, Z. Y. Zhang, K. T. V. Grattan, A. W. Palmer, and S. F. Collins, "Temperature dependence of the fluorescence lifetime in Pr^{3+}:ZBLAN glass for fiber optic thermometry," *Review of Scientific Instruments,* vol. 68, pp. 3447-3451, 1997.
[33] FiberLabs. *Technology*. Available: https://www.fiberlabs-inc.com/technology/
[34] Wikipedia. (2016). *ZBLAN*. Available: https://en.wikipedia.org/wiki/ZBLAN
[35] G. J. Leigh, *Nomenclature of inorganic chemistry*: Blackwell Scientific, 1990.
[36] P. M. Becker, A. A. Olsson, and J. R. Simpson, *Erbium-doped fiber amplifiers: fundamentals and technology*: Academic press, 1999.
[37] B. Frison, "Single and dual-wavelength lasing in the 800-820 nm and 1460-1520 nm bands in a Tm:ZBLAN fibre laser," McGill University, 2013.
[38] M. Pollnau and S. Jackson, "Advances in mid-infrared fiber lasers," in *Mid-infrared coherent sources and applications*, ed, 2008, pp. 315-346.
[39] X. Zhu and N. Peyghambarian, "High-power ZBLAN glass fiber lasers: review and prospect," *Advances in OptoElectronics,* vol. 2010, p. 501956, 2010.
[40] R. M. Percival, S. F. Carter, D. Szebesta, S. T. Davey, and W. A. Stallard, "Thulium-doped monomode fluoride fiber laser broadly tunable from 2.25 to 2.5 µm," *Electronics Letters,* vol. 27, pp. 1912-1913, 1991.
[41] R. M. El-Agmy and N. M. Al-Hosiny, "2.31 µm laser under up-conversion pumping at 1.064 µm in Tm^{3+}:ZBLAN fibre lasers," *Electronics Letters,* vol. 46, pp. 936-U94, 2010.
[42] T. Hasan, Z. Sun, F. Wang, F. Bonaccorso, P. H. Tan, A. G. Rozhin*, et al.*, "Nanotube–polymer composites for ultrafast photonics," *Advanced Materials,* vol. 21, pp. 3874-3899, 2009.
[43] Q. Bao, H. Zhang, Y. Wang, Z. Ni, Y. Yan, Z. X. Shen*, et al.*, "Atomic-layer graphene as a saturable absorber for ultrafast pulsed lasers," *Advanced Functional Materials,* vol. 19, pp. 3077-3083, 2009.

[44] S. Davide Di Dio Cafiso, E. Ugolotti, A. Schmidt, V. Petrov, U. Griebner, A. Agnesi, *et al.*, "Sub-100-fs Cr:YAG laser mode-locked by monolayer graphene saturable absorber," *Optics Letters,* vol. 38, pp. 1745-1747, 2013.

[45] J. Li, H. Luo, L. Wang, Y. Liu, Z. Yan, K. Zhou, *et al.*, "Mid-infrared passively switched pulsed dual wavelength Ho^{3+}-doped fluoride fiber laser at 3 μm and 2 μm," *Scientific Reports,* vol. 5, p. 10770, 2015.

[46] F. Zhu, H. Hundertmark, A. A. Kolomenskii, J. Strohaber, R. Holzwarth, and H. A. Schuessler, "High-power mid-infrared frequenc comb source based on femtosecond Er:fiber oscillator," *Optics Letters,* vol. 38, pp. 2360-2362, 2013.

[47] C. Manzoni, D. Polli, and G. Cerullo, "Two-color pump-probe system broadly tunable over the visible and the near infrared with sub-30 fs temporal resolution," *Review of Scientific Instruments,* vol. 77, 2006.

[48] F. Ganikhanov, C. L. Evans, B. G. Saar, and X. S. Xie, "High-sensitivity vibrational imaging with frequency modulation coherent anti-Stokes Raman scattering (FM CARS) microscopy," *Optics Letters,* vol. 31, pp. 1872-1874, 2006.

[49] R. Zhu, J. Xu, C. Zhang, A. C. Chan, Q. Li, P. C. Chui, *et al.*, "Dual-band time-multiplexing swept-source optical coherence tomography based on optical parametric amplification," *IEEE Journal of Selected Topics in Quantum Electronics,* vol. 18, pp. 1287-1292, 2012.

[50] Y. Mao, S. Chang, E. Murdock, and C. Flueraru, "Simultaneous dual-wavelength-band common-path swept-source optical coherence tomography with single polygon mirror scanner," *Optics Letters,* vol. 36, pp. 1990-1992, 2011.

[51] X. Liu, W. Zhao, H. Liu, K. Zou, T. Zhang, K. Lu, *et al.*, "A C- and L-band dual-wavelength Erbium-doped fibre laser for assisting four-wave mixing self-stability," *Journal of Optics A: Pure and Applied Optics,* vol. 8, pp. 601-605, 2006.

[52] H. D. Lee, Z. Chen, M. Y. Jeong, and C. S. Kim, "Simultaneous dual-band wavelength-swept fiber laser based on active mode locking," *IEEE Photonics Technology Letters,* vol. 26, pp. 190-193, 2014.

[53] J. Boullet, L. Lavoute, A. D. Berthelemot, V. Kermène, P. Roy, V. Couderc, *et al.*, "Tunable red-light source by frequency mixing from dual band Er/Yb co-doped fiber laser," *Optics Express,* vol. 14, pp. 3936-3941, 2006.

[54] J. H. Chong, M. K. Rao, Y. Zhu, and P. Shum, "An effective splicing method on photonic crystal fiber using CO^2 laser," *IEEE Photonics Technology Letters,* vol. 15, pp. 942-944, 2003.

[55] S. Pan, C. Lou, and Y. Gao, "Multiwavelength Erbium-doped fiber laser based on inhomogeneous loss mechanism by use of a highly nonlinear fiber and a Fabry-Perot filter," *Optics Express,* vol. 14, pp. 1113-1118, 2006.

[56] W. Clarkson, N. Barnes, P. Turner, J. Nilsson, and D. Hanna, "High-power cladding-pumped Tm-doped silica fiber laser with wavelength tuning from 1860 to 2090 nm," *Optics Letters,* vol. 27, pp. 1989-1991, 2002.

[57] X. Ma, D. Chen, Q. Shi, G. Feng, and J. Yang, "Widely tunable Thulium-doped fiber laser based on multimode interference with a large no-core fiber," *Journal of Lightwave Technology,* vol. 32, pp. 3234-3238, 2014.

[58] J. Li, Z. Sun, H. Luo, Z. Yan, K. Zhou, Y. Liu, *et al.*, "Wide wavelength selectable all-fiber Thulium doped fiber laser between 1925 nm and 2200 nm," *Optics Express,* vol. 22, pp. 5387-5399, 2014.

[59] Z. Li, S. U. Alam, Y. Jung, A. M. Heidt, and D. J. Richardson, "All-fiber, ultra-wideband tunable laser at 2 μm," *Optics Letters,* vol. 38, pp. 4739-4742, 2013.

[60] S. Liu, F. Yan, T. Feng, B. Wu, Z. Dong, and G.-K. Chang, "Switchable and spacing-tunable dual-wavelength Thulium-doped silica fiber laser based on a nonlinear amplifier loop mirror," *Applied Optics,* vol. 53, pp. 5522-5526, 2014.

[61] L. Shuo, Y. Fengping, P. Wanjing, F. Ting, D. Ze, and C. Geekung, "Tunable dual-wavelength Thulium-doped fiber laser by employing a HB-FBG," *IEEE Photonics Technology Letters,* vol. 26, pp. 1809-1812, 2014.
[62] F. Wang, D. Shen, D. Fan, and Q. Lu, "Widely tunable dual-wavelength operation of a high-power Tm:fiber laser using volume Bragg gratings," *Optics Letters,* vol. 35, pp. 2388-2390, 2010.
[63] X. Ma, S. Luo, and D. Chen, "Switchable and tunable Thulium-doped fiber laser incorporating a Sagnac loop mirror," *Applied Optics,* vol. 53, pp. 4382-4385, 2014.
[64] G. Aihui, M. Wanzhuo, W. Tianshu, J. Qingsong, Z. Peng, and W. Chunming, "Multiwavelength tunable ring fiber laser operating at 1.9 μm," *Microwave and Optical Technology Letters,* vol. 57, pp. 401-403, 2015.
[65] Z. Zhang, J. Wu, K. Xu, X. Hong, and J. Lin, "Tunable multiwavelength SOA fiber laser with ultra-narrow wavelength spacing based on nonlinear polarization rotation," *Optics Express,* vol. 17, pp. 17200-17205, 2009.
[66] A.-P. Luo, Z.-C. Luo, and W.-C. Xu, "Multi-wavelength Erbium-doped fiber ring laser based on wavelength-dependent polarization rotation with a phase modulator and an in-line comb filter," *Laser Physics,* vol. 19, pp. 1034-1037, 2009.
[67] T. Yamamoto, Y. Miyajima, and T. Komukai, "1.9 μm Tm-doped silica fibre laser pumped at 1.57 μm," *Electronics Letters,* vol. 30, pp. 220-221, 1994.
[68] Y. Liu, B. Liu, X. Feng, W. Zhang, G. Zhou, S. Yuan*, et al.*, "High-birefringence fiber loop mirrors and their applications as sensors," *Applied Optics,* vol. 44, pp. 2382-2390, 2005.
[69] Z. Jianluo, Y. Chao-Yu, G. G. Schinn, W. R. L. Clements, and J. W. Y. Lit, "Stable single-mode compound-ring Erbium-doped fiber laser," *Journal of Lightwave Technology,* vol. 14, pp. 104-109, 1996.
[70] J. Liu, J. P. Yao, J. Yao, and T. H. Yeap, "Single-longitudinal-mode multiwavelength fiber ring laser," *IEEE Photonics Technology Letters,* vol. 16, pp. 1020-1022, 2004.
[71] J. Zhou, A. Luo, Z. Luo, X. Wang, X. Feng, and B.-O. Guan, "Dual-wavelength single-longitudinal-mode fiber laser with switchable wavelength spacing based on a graphene saturable absorber," *Photonics Research,* vol. 3, pp. A21-A24, 2015.
[72] X. Chen, J. Yao, F. Zeng, and Z. Deng, "Single-longitudinal-mode fiber ring laser employing an equivalent phase-shifted fiber Bragg grating," *IEEE Photonics Technology Letters,* vol. 17, pp. 1390-1392, 2005.
[73] S. Pan, X. Zhao, and C. Lou, "Switchable single-longitudinal-mode dual-wavelength Erbium-doped fiber ring laser incorporating a semiconductor optical amplifier," *Optics Letters,* vol. 33, pp. 764-766, 2008.
[74] K. Scholle, E. Heumann, and G. Huber, "Single mode Tm and Tm,Ho:LuAG lasers for LIDAR applications," *Laser Physics Letters,* vol. 1, pp. 285-290, 2004.
[75] H. Waechter, D. Munzke, A. Jang, and H.-P. Loock, "Simultaneous and continuous multiple wavelength absorption spectroscopy on nanoliter volumes based on frequency-division multiplexing fiber-loop cavity ring-down spectroscopy," *Analytical chemistry,* vol. 83, pp. 2719-2725, 2011.
[76] R. Paschotta, R. Häring, E. Gini, H. Melchior, U. Keller, H. L. Offerhaus*, et al.*, "Passively Q-switched 0.1-mJ fiber laser system at 1.53 μm," *Optics Letters,* vol. 24, pp. 388-390, 1999.
[77] M. L. Siniaeva, M. N. Siniavsky, V. P. Pashinin, A. A. Mamedov, V. I. Konov, and V. V. Kononenko, "Laser ablation of dental materials using a microsecond Nd:YAG laser," *Laser Physics,* vol. 19, pp. 1056-1060, 2009.
[78] M. Laroche, A. M. Chardon, J. Nilsson, D. P. Shepherd, W. A. Clarkson, S. Girard*, et al.*, "Compact diode-pumped passively Q-switched tunable Er–Yb double-clad fiber laser," *Optics Letters,* vol. 27, pp. 1980-1982, 2002.
[79] B. J. Shastri, M. A. Nahmias, A. N. Tait, A. W. Rodriguez, B. Wu, and P. R. Prucnal, "Spike processing with a graphene excitable laser," *Scientific reports,* vol. 6, p. 19126, 2016.

[80] S. Liu, X. Zhu, G. Zhu, K. Balakrishnan, J. Zong, K. Wiersma, *et al.*, "Graphene Q-switched Ho^{3+}-doped ZBLAN fiber laser at 1190 nm," *Optics Letters,* vol. 40, pp. 147-150, 2015.

[81] G. Zhu, X. Zhu, K. Balakrishnan, R. A. Norwood, and N. Peyghambarian, "Fe^{2+}: ZnSe and graphene Q-switched singly Ho^{3+}-doped ZBLAN fiber lasers at 3 μm," *Optical Materials Express,* vol. 3, pp. 1365-1377, 2013.

[82] C. Wei, X. Zhu, F. Wang, Y. Xu, K. Balakrishnan, F. Song, *et al.*, "Graphene Q-switched 2.78 μm Er^{3+}-doped fluoride fiber laser," *Optics Letters,* vol. 38, pp. 3233-3236, 2013.

[83] G. Zhu, X. Zhu, F. Wang, S. Xu, Y. Li, X. Guo, *et al.*, "Graphene mode-locked fiber laser at 2.8 μm," *IEEE Photonics Technology Letters,* vol. 28, pp. 7-10, 2016.

[84] S. I. Islam, A. Islam, and S. Islam, "Integrated duo wavelength VCSEL using an electrically pumped GaInAs/AlGaAs 980 nm cavity at the bottom and an optically pumped GaInAs/AlGaInAs 1550 nm cavity on the top," *International Scholarly Research Notices,* vol. 2014, p. 10, 2014.

[85] D. Wu, Z. Luo, F. Xiong, C. Zhang, Y. Huang, S. Chen, *et al.*, "Passive synchronization of 1.06- and 1.53-μm fiber lasers Q-switched by a common graphene SA," *IEEE Photonics Technology Letters,* vol. 26, pp. 1474-1477, 2014.

[86] M. Zhang, E. J. R. Kelleher, A. S. Pozharov, E. D. Obraztsova, S. V. Popov, and J. R. Taylor, "Passive synchronization of all-fiber lasers through a common saturable absorber," *Optics Letters,* vol. 36, pp. 3984-3986, 2011.

[87] J. Sotor, G. Sobon, I. Pasternak, A. Krajewska, W. Strupinski, and K. M. Abramski, "Simultaneous mode-locking at 1565 nm and 1944 nm in fiber laser based on common graphene saturable absorber," *Optics Express,* vol. 21, pp. 18994-19002, 2013.

[88] J. Sotor, G. Sobon, J. Tarka, I. Pasternak, A. Krajewska, W. Strupinski, *et al.*, "Passive synchronization of Erbium and Thulium doped fiber mode-locked lasers enhanced by common graphene saturable absorber," *Optics Express,* vol. 22, pp. 5536-5543, 2014.

[89] Z. Luo, M. Zhou, J. Weng, G. Huang, H. Xu, C. Ye, *et al.*, "Graphene-based passively Q-switched dual-wavelength erbium-doped fiber laser," *Optics letters,* vol. 35, pp. 3709-3711, 2010.

[90] Y.-W. Song, S.-Y. Jang, W.-S. Han, and M.-K. Bae, "Graphene mode-lockers for fiber lasers functioned with evanescent field interaction," *Applied Physics Letters,* vol. 96, p. 051122, 2010.

[91] J. Liu, J. Xu, K. Liu, F. Tan, and P. Wang, "High average power picosecond pulse and supercontinuum generation from a Thulium-doped, all-fiber amplifier," *Optics Letters,* vol. 38, pp. 4150-4153, 2013.

[92] S. D. Jackson, "Towards high-power mid-infrared emission from a fibre laser," *Nature Photonics,* vol. 6, pp. 423-431, 2012.

[93] R. G. Smart, J. N. Carter, A. C. Tropper, and D. C. Hanna, "Continuous-wave oscillation of Tm^{3+}-doped fluorozirconate fibre lasers at around 1.47 μm, 1.9 μm and 2.3 μm when pumped at 790 nm," *Optics Communications,* vol. 82, pp. 563-570, 1991.

[94] R. M. Percival, D. Szebesta, and S. T. Davey, "Highly efficient and tunable operation of two colour Tm-doped fluoride fibre laser," *Electronics Letters,* vol. 28, pp. 671-673, 1992.

[95] P. Tang, Z. Qin, J. Liu, C. Zhao, G. Xie, S. Wen, *et al.*, "Watt-level passively mode-locked Er^{3+}-doped ZBLAN fiber laser at 2.8 μm," *Optics Letters,* vol. 40, pp. 4855-4858, 2015.

[96] C. Wei, X. Zhu, R. A. Norwood, and N. Peyghambarian, "Passively continuous-wave mode-locked Er^{3+}-doped ZBLAN fiber laser at 2.8 μm," *Optics Letters,* vol. 37, pp. 3849-3851, 2012.

[97] C. Wei, X. Zhu, R. A. Norwood, and N. Peyghambarian, "Passively Q-switched 2.8-μm nanosecond fiber laser," *IEEE Photonics Technology Letters,* vol. 24, pp. 1741-1744, 2012.

[98] V. Lambin-Iezzi, S. Loranger, M. Saad, and R. Kashyap, "Stimulated Brillouin scattering in SM ZBLAN fiber," *Journal of Non-Crystalline Solids,* vol. 359, pp. 65-68, 2013.